EXPERIMENTAL STUDY OF ANTIPROTON-PROTON ANNIHILATION INTO A PAIR OF CHARGED PI-MESONS OR K-MESONS FOR INCIDENT ANTIPROTON MOMENTA IN THE RANGE FROM 0.72 GeV/c TO 2.62 GeV/c

Thesis by

Douglas G. Fong

In Partial Fulfillment of the Requirements

For the Degree of

Doctor of Philosophy

California Institute of Technology

Pasadena, California

1968

(Submitted March 13, 1968)

ACKNOWLEDGMENTS

This experiment was carried out at Brookhaven National Laboratory's AGS as a combined effort of members from the Caltech's Users Group, Al Maschke, and Ted Zipf. Special gratitude is due Jerome Pine who, as my thesis advisor, provided me with many invaluable suggestions, and Alvin Tollestrup, the leader of the Caltech Users Group. Barry Barish, Ricardo Gomez, Don Hartill, Al Maschke, Jerry Pine, Alvin Tollestrup, and Ted Zipf all shared equally in carrying out the running of the experiment. John Madey, Peter Mazur, and Jerry Mar of Caltech also contributed to the effort.

Thanks are also due Tom Blair, Bob Gibbs, Jim Sanford and the AGS crew for their help and cooperation.

About 10,000 of the 40,000 pictures taken in this part of the experiment were measured with a Vanguard machine at Stanford Linear Accelerator Center with a technique worked out by Ted Zipf. Thanks are also due Miss Diane Maue for her supervision of the operation. The rest of the pictures were analyzed at Caltech with the help of Marshall Armistead, Mitch Persons, and Bill Peterson. Special thanks are due Bill Friedler, Don Hartill and Mrs. Phyllis Nilsson, all of whom assisted the analysis effort. Thanks are also due Barry Barish for stimulating discussions.

For financial support, the author is indebted to the Xerox EOS Corporation, the Atomic Energy Commission, and to the California Institute of Technology.

ABSTRACT

The cross sections for the two antiproton-proton annihilation-in-flight modes,

$$\bar{p} + p \rightarrow \pi^+ + \pi^-$$

$$\bar{p} + p \rightarrow k^+ + k^-$$

were measured for fifteen laboratory antiproton beam momenta ranging from 0.72 to 2.62 GeV/c. No magnets were used to determine the charges in the final state. As a result, the angular distributions were obtained in the form $[\frac{d\sigma}{d\Omega}(\Theta_{C.M.}) + \frac{d\sigma}{d\Omega}(\pi - \Theta_{C.M.})]$ for $45 \lesssim \Theta_{C.M.} \lesssim 135^o$.

A hodoscope-counter system was used to discriminate against events with final states having more than two particles and antiproton-proton elastic scattering events. One spark chamber was used to record the track of each of the two charged final particles. A total of about 40,000 pictures were taken. The events were analyzed by measuring the laboratory angle of the track in each chamber. The value of the square of the mass of the final particles was calculated for each event assuming the reaction

$$\bar{p} + p \rightarrow \text{a pair of particles with equal masses.}$$

About 20,000 events were found to be either annihilation into $\pi^{\pm}$-pair or $k^{\pm}$-pair events. The two different charged meson pair modes were also distinctly separated.

The average differential cross section of $\bar{p} + p \rightarrow \pi^+ + \pi^-$ varied from ~ 25 μb/sr at antiproton beam momentum 0.72 GeV/c (total energy in center-of-mass system, $\sqrt{s} = 2.0$ GeV) to ~ 2 μb/sr at beam momentum 2.62 GeV/c ($\sqrt{s} = 2.64$ GeV). The most striking feature in the angular distribution was a peak at $\Theta_{C.M.} = 90^o$ ($\cos \Theta_{C.M.} = 0$) which increased with $\sqrt{s}$ and reached a maximum at $\sqrt{s} \sim 2.1$ GeV (beam momentum ~ 1.1 GeV/c). Then it diminished and seemed to disappear completely at $\sqrt{s} \sim 2.5$ GeV (beam momentum ~ 2.13 GeV/c). A valley in the angular distribution occurred at $\cos \Theta_{C.M.} \cong 0.4$. The differential cross section then increased as $\cos \Theta_{C.M.}$ approached 1.

The average differential cross section for $\bar{p} + p \rightarrow k^+ + k^-$ was about one third of that of the $\pi^{\pm}$-pair mode throughout the energy range of this experiment. At the lower energies, the angular distribution, unlike that of the $\pi^{\pm}$-pair mode, was quite isotropic. However, a peak at $\Theta_{C.M.} = 90^o$ seemed to develop at $\sqrt{s} \sim 2.37$ GeV (antiproton beam momentum ~ 1.82 GeV/c). No observable change was seen at that energy in the $\pi^{\pm}$-pair cross section.

The possible connection of these features with the observed meson resonances at 2.2 GeV and 2.38 GeV, and its implications, were discussed.

TABLE OF CONTENTS

TABLE OF CONTENTS (cont.)

TABLE OF CONTENTS (cont.)

APPENDICES

LIST OF FIGURES

LIST OF FIGURES (cont.)

LIST OF FIGURES (cont.)

LIST OF FIGURES (cont.)

LIST OF FIGURES (cont.)

LIST OF FIGURES (cont.)

LIST OF FIGURES (cont.)

LIST OF FIGURES (cont.)

LIST OF TABLES

LIST OF TABLES (cont.)

I. INTRODUCTION

The purpose of this thesis is to describe and report the results of an experiment which measured the cross sections of two antiproton-proton annihilation modes:

$$\bar{p} + p \rightarrow \pi^+ + \pi^- \tag{1}$$

$$\bar{p} + p \rightarrow k^+ + k^- \tag{2}$$

The cross channels of these reactions, the elastic scattering of $\pi^\pm$ or $k^\pm$-mesons by protons,

$$\pi^\pm + p \rightarrow \pi^\pm + p$$

$$k^\pm + p \rightarrow k^\pm + p$$

have been frequently used for the understanding of strong interactions. For example, the scattering cross sections at various total energies have provided information about the existence and quantum numbers of various fermion resonances.

The cross sections of the antiproton-proton annihilations into charged π or k meson pairs are interesting because they can provide further tests of the theories that have been used to understand $\pi^\pm$ or $k^\pm$ elastic scattering, and information about certain boson resonances. However, experimental data for these annihilation modes have been very scarce. The reason is that their cross sections are two orders of magnitude smaller than the corresponding elastic cross sections at the same total energy.

A further reason for the difficulty in measuring these annihilation cross sections is that they contribute only a very small part to the total annihilation cross section. For 1.5 GeV/c antiprotons and stationary protons, the total cross section for antiproton-proton interaction is 100 mb, [1] while the $\pi^{\pm}$-pair and $k^{\pm}$-pair annihilation cross sections are only of the order of 100 μb.

Previous to this experiment, the investigation of annihilations into $\pi^{\pm}$- and $k^{\pm}$-pairs had only been done with bubble chambers. The experiment which observed the largest number of events was done at 1.61 GeV/c antiproton beam momentum by Lynch et al. [2), 3)] From 20,200 antiproton interactions, only 21 $\pi^{\pm}$-pair and 11 $k^{\pm}$-pair annihilations were identified. The number of bubble chamber pictures and the amount of analysis required to obtain angular distributions at many energies with good statistics would be impossibly large.

The annihilation modes (1) and (2) have, however, the distinction of having only two final particles, both of which are charged, while essentially all other annihilations result in three or more particles. Consequently, the simple criterion that an event must have two charged particles coplanar with the incident antiproton direction eliminates a very large majority of annihilations which are not interesting here.

The coplanarity condition does not eliminate antiproton-proton elastic scattering events, whose cross section is about two orders of magnitude greater than the combined cross section of the $\pi^{\pm}$-pair and $k^{\pm}$-pair annihilation modes. However, in the laboratory system, the kinematics for $\bar{p}$ - p elastic scattering are quite different from those for $\bar{p}$ - p annihilation into a $\pi^{\pm}$-pair

or a $k^{\pm}$-pair. The combined use of counters and spark chambers can therefore be advantageously applied to measure the small cross sections of the $\pi^{\pm}$-pair and $k^{\pm}$-pair annihilation modes. Before the spark chambers are triggered, hodoscopes can be used to discriminate against those events which have more than two charged particles in the final states, or which have a pair of charged particles not coplanar with the direction of the incident antiproton, or which are kinematically similar to $\bar{p}$ - p elastic events.

The equipment of this experiment was primarily designed to measure the cross section of the annihilation of antiproton and proton into electron and positron.[4] The cross section of this mode was expected to be of the order of one nanobarn. For this reason, a high intensity antiproton beam was constructed. The liquid hydrogen target used was 80" long, and large hodoscopes and spark chambers were positioned around the target to cover a large solid angle. An elaborate trigger system was designed to discriminate against uninteresting antiproton-proton interactions. To obtain a rich sample of spark chamber pictures for $\pi^{\pm}$-pair and $k^{\pm}$-pair annihilations, all that was necessary was a slight modification of the trigger conditions.

A total of approximately 40,000 spark chamber pictures were taken for the two charged meson pair annihilation modes at 15 different antiproton beam momenta ranging from 0.72 to 2.62 GeV/c. After analysis, about 20,000 events were identified as either $\pi^{\pm}$-pair or $k^{\pm}$-pair events. Since no magnets were used in the equipment to determine the charges of the final particles, the angular distributions obtained were in the form

II. EXPERIMENTAL APPARATUS

A. Introduction

In this experiment, events of the annihilation modes

$$\bar{p} + p \rightarrow \pi^+ + \pi^-$$

$$\bar{p} + p \rightarrow k^+ + k^-$$

were identified by measuring the angles of the final state particles.

Firstly, with initially stationary proton and moving antiproton, an event of either of the above types has final particles coplanar with the path of the incident antiproton. Secondly, for a definite antiproton momentum, the angles between the directions of the final particles and that of the antiproton depend on the masses of the two final particles. Fig. 2.1 shows the kinematic curves for the above two annihilations and antiproton-proton elastic scattering for 1.75 GeV/c incident antiprotons. Thus, by measuring the angles between the final particles and the incident antiproton, the mass of the final particles can be determined.

As can be seen from Fig. 2.1, antiproton-proton elastic scattering events are kinematically very different from those of $\pi^{\pm}$-pair or $k^{\pm}$-pair annihilation modes. In this experiment, a hodoscope system was designed to separate the elastic events from the two-meson annihilation events. The separation of the two meson-pair annihilation modes from each other was achieved by accurate measurements of the final particle tracks as recorded by spark chambers. For this experiment, the laboratory angles between

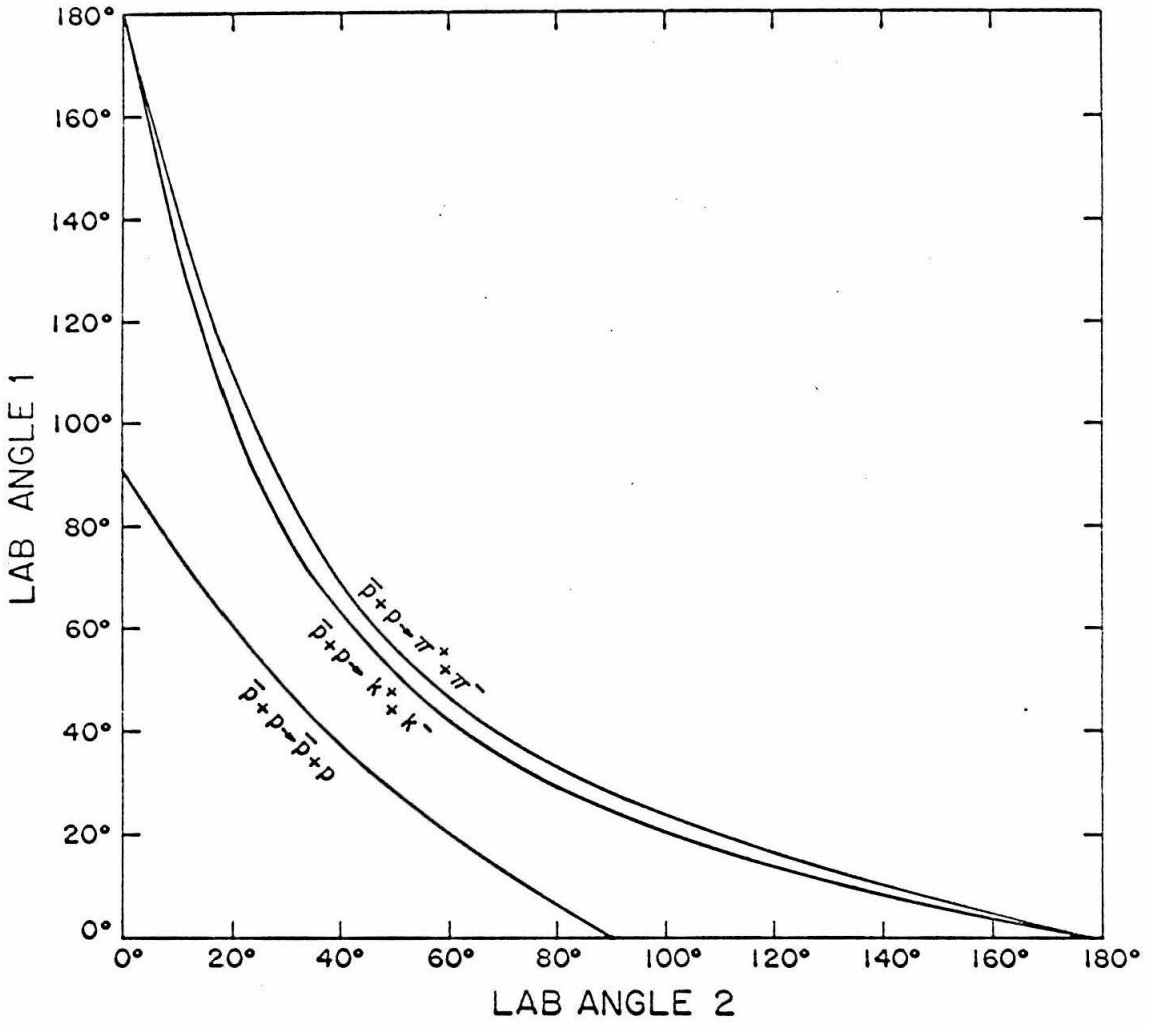

Fig. 2.1 Kinematic curves for 1.75 GeV/c incident antiprotons

the final particles and the incident antiproton ranged from about 25^{o} to 110^{o}. From the curves in Fig. 2.1, it can be seen that a minimum accuracy of about $\pm 1^{o}$ was necessary for this separation.

A schematic drawing of the apparatus is shown in Fig. 2.2. A plan view and an end view are also shown in Figs. 2.3 and 2.4. Two spark chambers were placed symmetrically on the left and right sides of the target to record the paths of the final charged particles. Before spark chamber pictures were taken, the directions of the final charged particles were determined roughly with six scintillation hodoscopes. The channels in the outermost hodoscopes were horizontal and parallel to the target. They provided a measurement of coplanarity. The other four hodoscopes had vertical channels and provided measurements of the angles between the final particles and the antiproton beam. The width of the channels in these hodoscopes was chosen so that they were able to distinguish between $\bar{p}$- p elastic events and $\pi^{\pm}$-pair or $k^{\pm}$-pair annihilations. The spark chambers were triggered to record the tracks of charged particles only after the hodoscopes determined roughly that the two charged particles in the final states were coplanar, and that they were kinematically consistent with $\pi^{\pm}$-pair or $k^{\pm}$-pair annihilations but not with $\bar{p}$- p elastic events.

For a definite determination of the angles of the final charged particles, it was required electronically that one and only one channel in each hodoscope detected the passage of a charged particle in an event. This also discriminated against multi-particle annihilations.

The hodoscopes and the spark chambers subtended about 90^{o} of the azimuth on each side of the target. In almost all of the other directions, the target was enclosed with veto counters behind

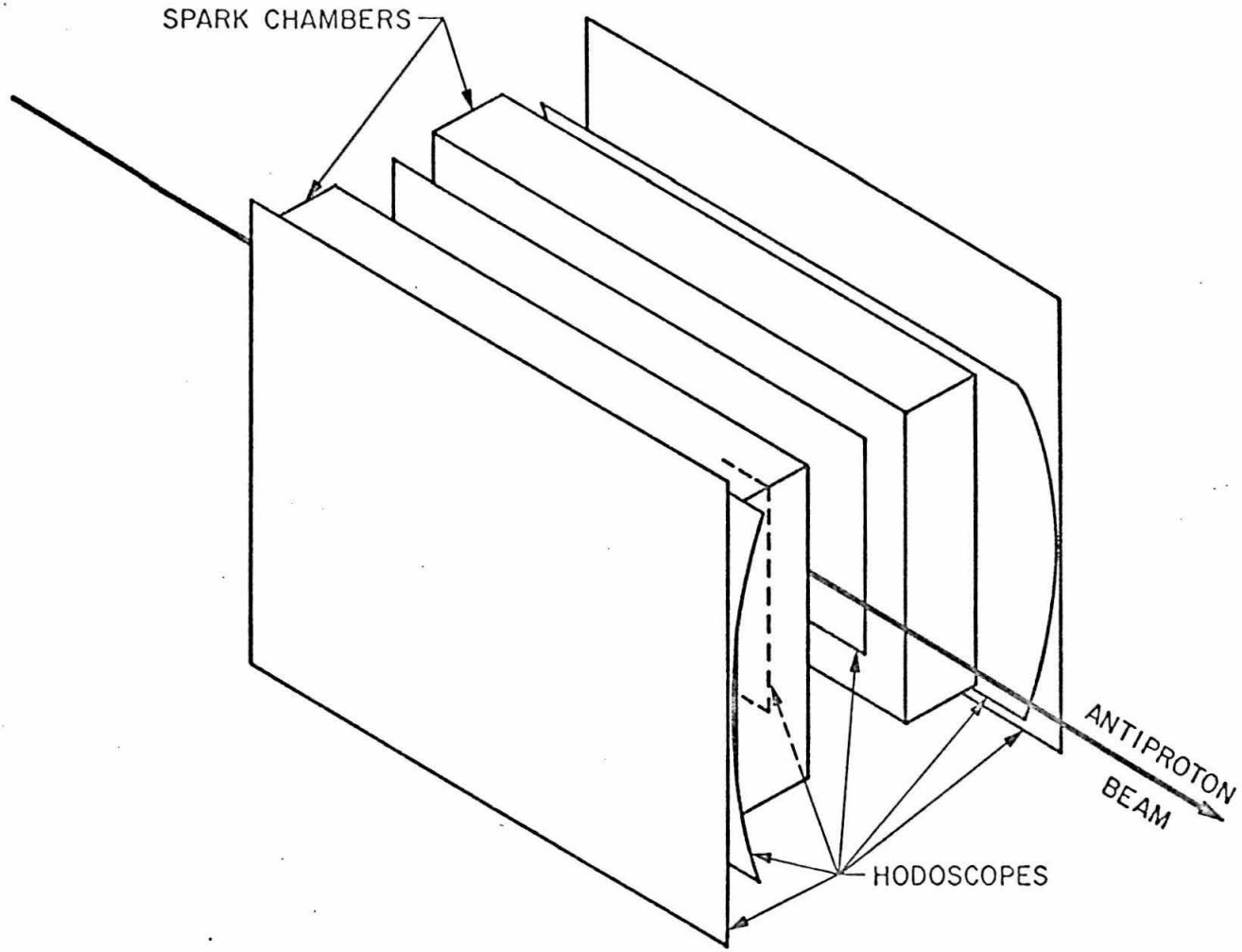

Fig. 2.2 Schematic diagram of the detection apparatus

lead sheets. These were also used to discriminate against events which resulted in more than two particles.

The remainder of this chapter gives a more detailed description of the various components of this experiment, and how they were utilized. The spark chamber data reduction is discussed in the following two chapters.

B. The Antiproton Beam

The antiproton beam used in this experiment was the long branch of a partially separated beam designed and built at Brookhaven National Laboratory's AGS. A detailed description of the construction of the beam is given in Ref. 5.

The antiproton yield was

$70,000/10^{12}$ protons in AGS at 2.5 GeV/c

and $30,000/10^{12}$ protons at 1.5 GeV/c.

At 2.5 GeV/c, the π^- and μ^- to $\bar{p}$ ratio was about 1.5 to 1, and the beam divergence was about $\pm 0.6^{o}$ at the hydrogen target. The momentum spread was about $\pm 3.5\%$ of the mean beam momentum. The cross section at the target was oval shaped, and was about 1" x 2", depending somewhat on the beam momentum.

Antiprotons in the beam were identified by time of flight. The main contaminations were π^-'s and μ^-'s. This was studied at beam momentum 2.5 GeV/c:

a) When the electrostatic separators of the beam[5] were tuned to select π^- or μ^--mesons, it was found that the time-of-flight method to select antiprotons was able to discriminate against π^- or μ^--mesons with better than 99% efficiency.

b) When the separators were tuned to select antiprotons, it was found that the antiproton to π^- or μ^--meson ratio at the target was about 1.5 to 1.

The conclusion was that with the combined use of the separators and the time-of-flight method, the contamination of the antiproton count was less than 0.7%. At the highest nominal beam momentum of this experiment (2.75 GeV/c), the contamination was not expected to be much worse, while at the lower beam momenta, it was expected to be even better because of the even more effective time-of-flight selection.

After each antiproton was identified, a dead time of about 4 μ sec was imposed on the beam electronics. This was to prevent the spark chamber from recording simultaneously the final products of more than one $\bar{p}$ - p interaction. (The sensitive time of the spark chambers was $\simeq$ 2.5 μ sec.)

C. The Target

Liquid hydrogen was used as the material for the target. It was contained in a cylindrical mylar flask 4" in diameter and 82.5" long. The mylar wall was 0.014" thick. The target was wrapped in thirty layers of super-insulation (crinkled 0.00025" thick mylar). It was suspended by thin stainless steel wire hangers inside an evacuated aluminum chamber with 0.014" thick mylar side walls. The liquid hydrogen was fed in and the gaseous hydrogen vented through a 2" wide brass collar at the upstream end of the flask. The total usable length of the target was 80". The total material, besides the liquid hydrogen, through which a particle coming from the target had to pass to enter the detection hodoscopes was only 0.036" of mylar. From the boil-off rate of the liquid hydrogen during the experiment, a calculation was made to set a limit on the correction to the liquid hydrogen density due to gas bubbles. The hydrogen density in the target was found to be 0.069 gm/c.c..[4)]

D. The Veto Counters

The top and bottom of the target frame were lined with 1/4" thick lead sheets. Behind them were two 1 1/2" thick, 12" wide, and 80" long scintillation counters. Their function was to detect either charged or neutral particles leaving the target in the upward or downward directions not subtended by the hodoscopes. The lead-scintillator combination was tested at the 1.5 GeV electron synchrotron at Caltech, and was found to be 65 ± 15% efficient in detecting high energy photons. If the top or bottom counters detected particles after the beam electronics identified an anti-proton, the "event" was vetoed and not examined by the electronics in the spark chamber trigger system. These veto counters were used to discriminate against some of the multi-particle final state annihilations.

At the upstream end of the target, there was a 12" x 12" x 1/2" scintillation counter perpendicular to the beam direction, with a 3" diameter circular hole at the center. The center of the hole was positioned on the axis of the antiproton beam. This counter served both as a beam collimator, and a veto counter against interactions which produced a very backward charged particle.

At the downstream end of the target was a solid 12" x 12" x 1/2" scintillation counter also used in veto. This counter registered the antiprotons that did not interact with any proton in the target, or events that produced at least one very forward charged particle (e.g., diffraction elastic scattering of the antiproton). Earlier in the experiment, a 1/4" lead sheet was placed in front of this counter to convert π^o's or γ's. Later, the lead sheet was removed. The net results after analysis showed no observable difference.

E. The Hodoscope System

Six trays of scintillation counters were used in this experiment. Their positions relative to the hydrogen target are shown in Figs. 2.3 and 2.4. The setup was left-right symmetric. Mainly in order to minimize the required number of phototubes, the scintillators in each tray were overlapped as shown in Figs. 2.3 and 2.4. The "channels" were defined by coincidence or anticoincidence between adjacent counters. All the scintillators in the hodoscopes were 1/4" thick, and all the phototubes used were RCA 6655A's.

The scintillators of the eleven counters in the outermost tray on each side were all 80" long. They were placed vertically with their lengths parallel to the target. The top and bottom ones were 4.4" wide, and the rest 6.6" wide. Each counter had a phototube on each end to increase the light collection efficiency. They were overlapped to form 21 "channels", each of width 2.2".

The counters of the hodoscope on the left were numbered 1 to 11 from top to bottom, and those on the right were numbered 1 to 11 in the opposite direction. (Left and right were defined with the viewer standing upright, facing along the beam direction.) The "channels" were numbered 6 to 26 from top to bottom for both trays. These two hodoscopes were placed equidistant (24") from the axis of the target. They were used to impose a rough coplanarity condition on the particles coming from the target. A pair of tracks from the target axis, perfectly coplanar with the axis of the antiproton beam, would always strike the hodoscopes at two "channels" whose sum was 32, independent of the inclination of the plane defined by these

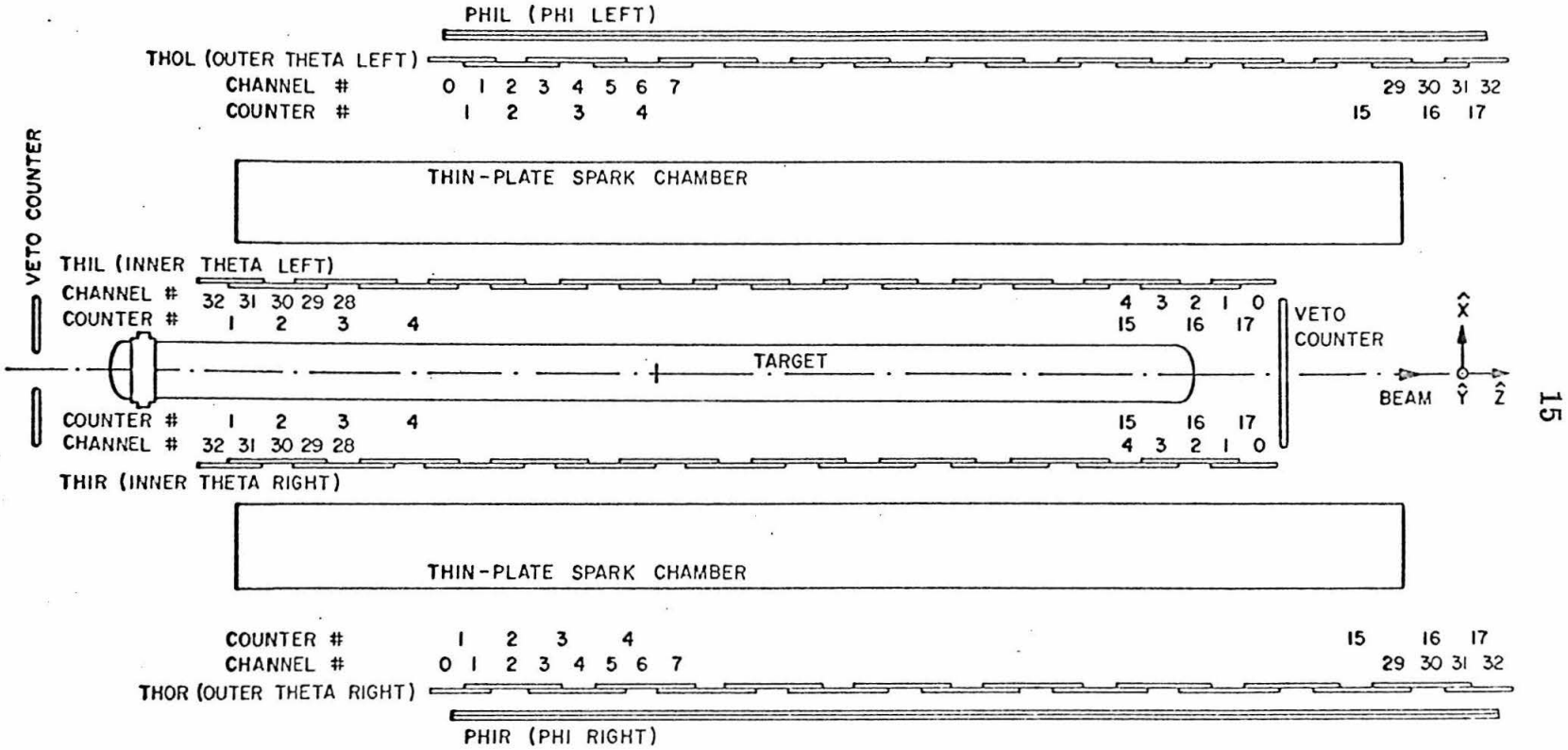

Fig. 2.3 Top view of the detection apparatus

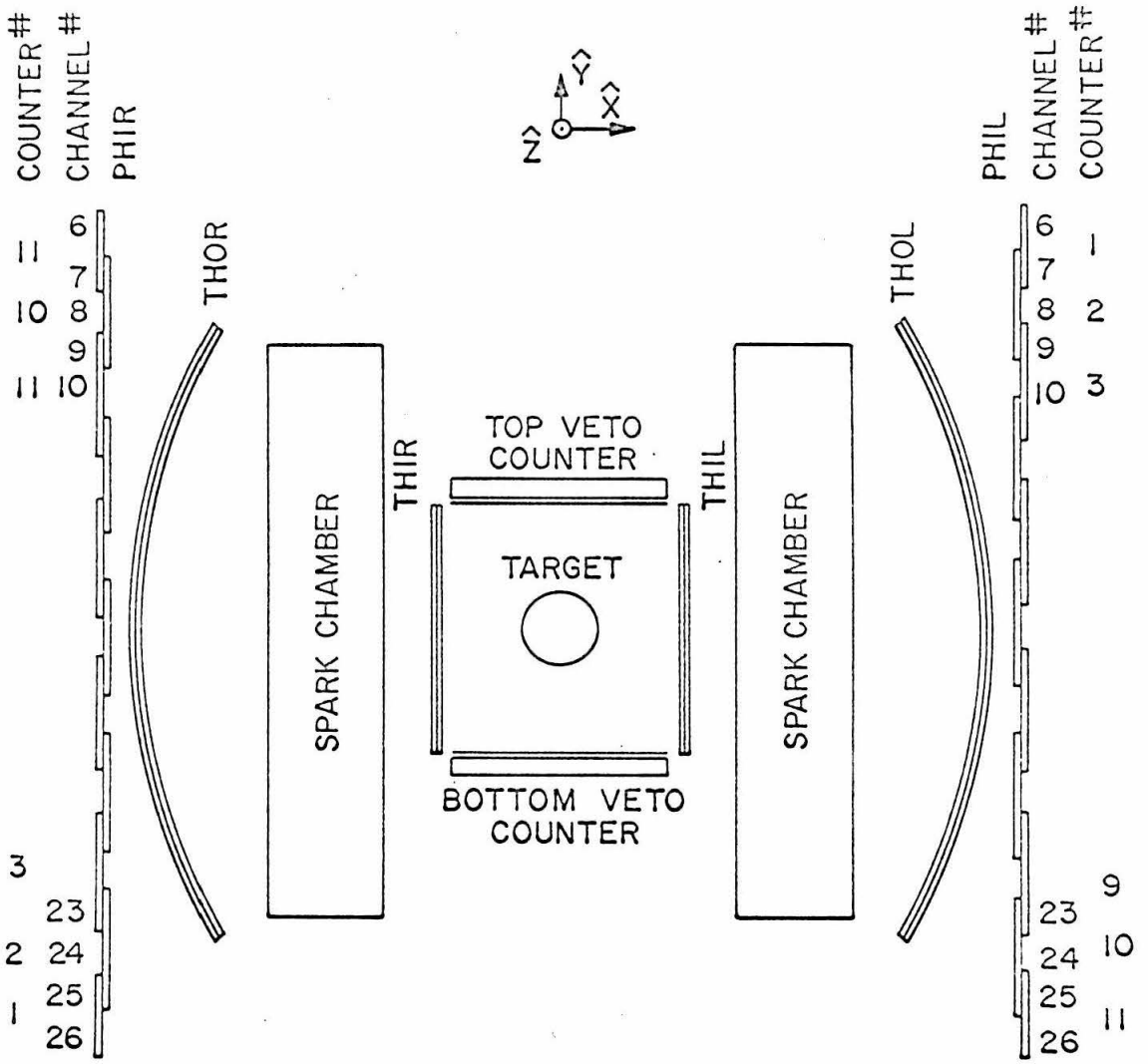

Fig. 2.4 End view of the detection apparatus

tracks. These two hodoscopes were called the left and the right phi trays.[†]

In each of the other hodoscopes there were seventeen counters, forming 33 channels of width 2.5". The most upstream and the most downstream counters were 5" wide; all the rest were 7.5" wide. The counters were placed vertically with their lengths perpendicular to the target. Each had one phototube at the bottom end.

The scintillators of the innermost trays were straight, 13.5" tall, and 6.5" from the axis of the target. They were called the inner theta hodoscope trays. The middle trays, called the outer theta trays, were curved, having a radius of curvature of 34", and were 22.2" from the axis of the target. They were 33.2" tall. The counters in each tray were numbered 1 to 17 from upstream to downstream. The channels were numbered 0 to 32 from upstream to downstream for the outer theta trays and from downstream to upstream in the case of the inner theta trays. All the channels numbered 32 were not used.

If a particle, coming from the target, passed through two theta trays, the sum of the channel numbers for the track indicated, within a small range ($\sim 8^{o}$), the value of the angle θ between the track and the direction of the beam, independent of where the particle came from along the target. The purpose of having the

---

[†]The angle between the plane defined by a two body final state and the horizontal plane was called the ϕ angle. For a complete definition of the chosen coordinate system in the laboratory, see Chapter 3, Section B.

outer θ counters curved was to eliminate also the dependence of this sum on the azimuthal angle ϕ of the particle track.

In this manner, the six hodoscopes provided crude measurements of coplanarity (ϕ channel sum), azimuthal angles (left and right ϕ channel numbers), the location of the interaction inside the target (inner θ channel numbers), and the two laboratory polar angles of the final particles (left and right θ channel sums).

F. Information from a Hodoscope

The signals from the phototubes of the hodoscopes were fed into an electronic system built at Caltech (CC1 -- Caltech Computer 1), and the following pieces of information were extracted from each hodoscope:

1) Whether there was at least one pair of adjacent counters which detected the passage of a charged particle, (this was called "coincidence > 0"),

2) Whether there were more than one pair of adjacent counters which were fired (coincidence > 1),

3) Whether at least one "hodoscope channel" detected a charged particle (channel > 0),

4) Whether more than one "channel" were fired (channel > 1),

5) The number of the channel which detected the passage of a charged particle.

It is evident that both coincidence > 1 and channel > 1 signals from a hodoscope indicated the passage of at least two charged particles through the same hodoscope, and hence the presence of more than two final particles in the event.

Appendix 1 gives a detailed description of how these pieces of information were extracted from the signals of a hodoscope.

G. Theta Channel Sum Matrix

The sum of the channel numbers from the two theta-hodoscopes on the same side of the target corresponded to a certain value of the polar angle θ within a small range. If the value of "channel sum" was made into a continuous rational number, this relationship could be expressed as

$$\text{channel sum} = 5.9 \times \cot\theta + 25.3$$

Fig. 2.5 shows the theta channel sum matrix in the cot θ_{right} vs. cot θ_{left} plane. For a definite antiproton beam momentum, the values of θ-left and θ-right for the process $\bar{p} + p \rightarrow$ (equal mass pair) have a definite relation as shown in Fig. 2.1. Thus, processes like $\bar{p} + p \rightarrow \pi^+ + \pi^-$, $\bar{p} + p \rightarrow k^+ + k^-$, and $\bar{p} + p \rightarrow \bar{p} + p$ can be represented by single lines in the cot θ_{right} vs. cot θ_{left} plane, as shown in Fig. 2.5. The curves are for an incident antiproton momentum of 1.75 GeV/c.

In the CC1 (Caltech Computer 1), two five bit binary encoders (see Appendix 1), registered the values of the channel numbers for inner-theta and outer-theta hodoscopes on each side. These encoders were connected to the inputs of a 6 bit fast adder. The answers corresponding to theta channel sums 23 to 38 were used to drive each of the two sides of a 16 x 16 coincidence matrix corresponding to a left-channel-sum vs. right-channel sum matrix. An output signal, called "K" (for "desired kinematics"), could be obtained from the CC1 if any one of a selected group of coincidence matrix elements was activated. For example, in Fig. 2.6, the squares inside the boundary marked by the heavy line represent the

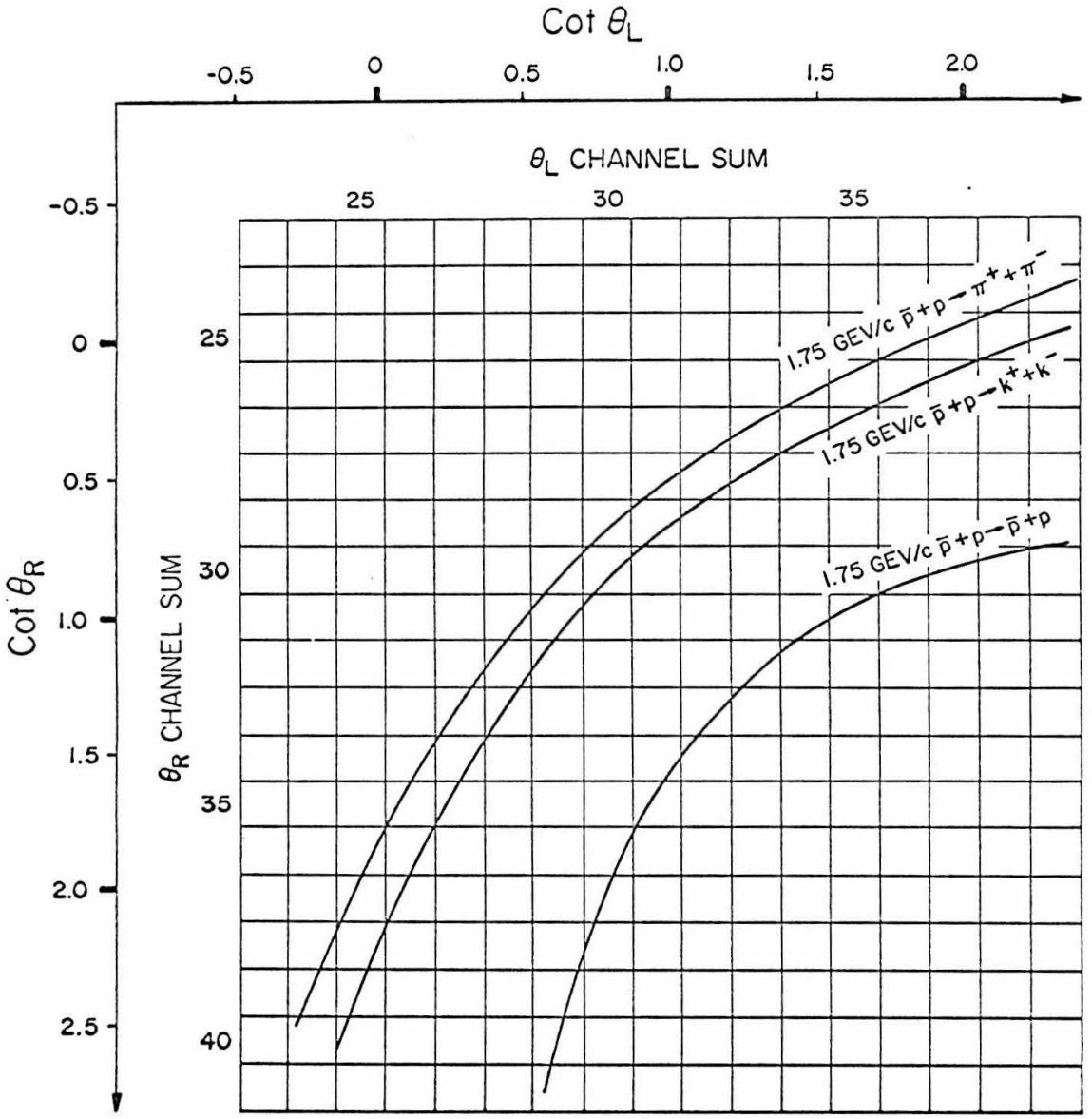

Fig. 2.5 θ_L-channel sum vs. θ_R-channel sum matrix in cot θ_L vs. cot θ_R space for $\phi = 0$

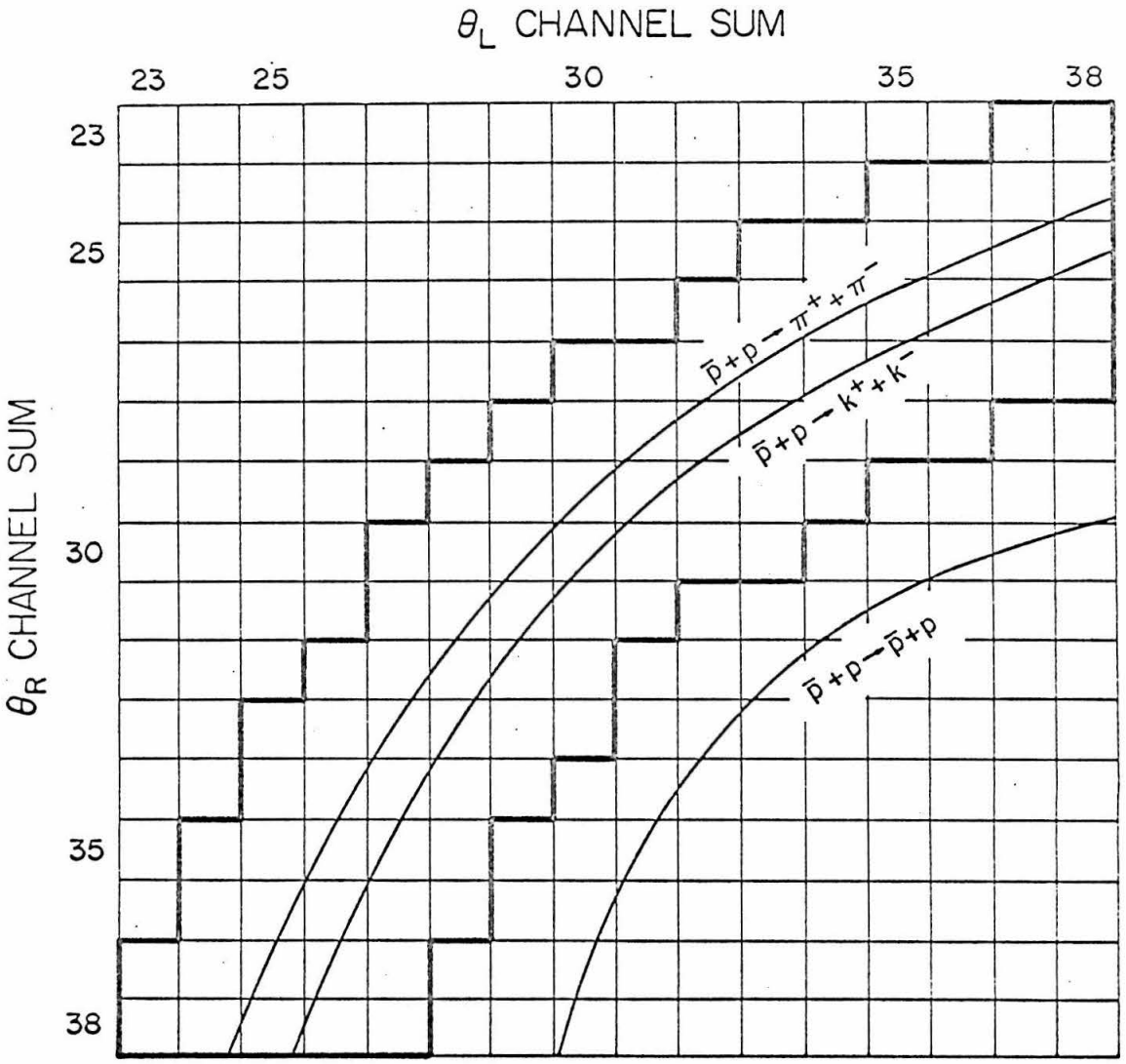

Fig. 2.6 The "kinematic matrix" in CC1. The heavy line marks the boundary of the activated matrix elements for runs with nominal beam momentum 1.75 GeV/c

coincidence matrix elements ("K matrix") for selecting $\pi^{\pm}$-pair and $k^{\pm}$-pair events at an antiproton momentum of 1.75 GeV/c. With this K matrix, the $\bar{p}$- p elastic scattering events could thus be completely eliminated, while maintaining high efficiency for the desired events.

H. Trigger Conditions

a) "Compute". If the time-of-flight (TOF) counters in the beam electronics identified an antiproton, and if the veto counters around the target detected no passage of charged particles, a signal called "Compute" was generated for the CC1 to investigate the signals, if any, from the hodoscopes. This can be symbolized as:

$$\text{Compute} = \text{TOF (antiproton)} \cdot \overline{V_{top}} \cdot \overline{V_{bottom}} \cdot \overline{V_{front}} \cdot \overline{V_{rear}}$$

(Bars over symbols denote "not".)

b) "Necessary" (denoted as "N"). Upon receiving the signal "Compute", the CC1 decided for each tray whether

i) channel > 0 (see Section F),

ii) channel > 1,

iii) coincidence > 0,

iv) coincidence > 1.

For a final states with only two charged particles, it was necessary that each hodoscope satisfied (channel > 0) $\cdot$ $\overline{(\text{channel} > 1)}$ $\cdot$ $\overline{(\text{coincidence} > 1)}$, and the "Necessary" condition was defined as

$$N = \text{Compute} \cdot \prod_{\substack{\text{six} \\ \text{hodoscopes}}} (\text{channel} > 0) \cdot \overline{(\text{channel} > 1)} \cdot \overline{(\text{coincidence} > 1)}.$$

c) Coplanarity ("ϕ"). CC1 also simultaneously calculated the channel numbers for the two ϕ hodoscopes, and the ϕ channel

sum (= [(ϕ_{left} channel number) + (ϕ_{right} channel number)]).

As pointed out in Section E, for an ideal coplanar event, originating from the axis of the target, the ϕ channel sum should be 32. During the experiment, this condition was relaxed to allow for the finite size of the beam, possible inaccuracy in the positioning of the hodoscopes, and other factors:

$$\text{"}\phi\text{"} = (\phi \text{ channel sum} = 31, 32, 33)$$

Even with this relaxation, it was found that some good events were lost due to the "ϕ" requirement. This is discussed in detail in Chapter 5, Section D.

d) Desired kinematics ("K"). CC1 also computed the channel numbers from each of the four theta-hodoscopes, the θ_{left} channel sum, and the θ_{right} channel sum, and then decided whether the event was desired kinematically (see last section).

To include all $\pi^{\pm}$-pair and $k^{\pm}$-pair annihilation events, the matrix elements in CC1 were chosen quite liberally to allow for θ-tray misalignment and the slight ϕ dependence of the $\pi^{\pm}$, $k^{\pm}$ curves in the θ channel sum matrix. The criterion used was that every point on the boundary of the matrix elements included must not be less than 1 1/4 channels away from the ideal $\pi^{\pm}$, $k^{\pm}$ curves for $\phi = 0$. An example is shown in Fig. 2.6.

The conditions "N", "ϕ", "K" were available separately from the CC1. For most of the fifteen beam momenta in this experiment, the spark chambers were triggered for events which satisfied all three conditions, "N", "ϕ", and "K". During the experiment, the CC1 was able to make all the computations and

decisions in about 150 nsec. For every picture, all the hodoscope counter numbers were recorded, as will be discussed in Section J.

For the lowest two momenta, the antiproton beam flux was low enough that only "N" and "ϕ" conditions were imposed. With just these conditions, the trigger rate was much less than one per AGS beam pulse. During the analysis of the pictures obtained at these beam momenta, the condition "K" was imposed to economize measurement.

I. Spark Chambers and Camera System

Two thin-plate spark chambers were used for observing the paths of the charged particles in the final states. They were placed symmetrically, one on each side of the target as shown in Figs. 2.2, 2.3, and 2.4.

In each chamber, there were nine plates, each consisting of 0.001" thick tempered aluminum foil stretched and bonded over a 3" thick aluminum frame with dimensions 3/8" x 38" x 96". The plates were separated by 0.34" thick mylar spacers, forming eight spark gaps. The side walls of the chamber were 0.014" thick mylar sheets. The gas used was 10% He and 90% Ne, very slightly above atmospheric pressure. The chambers were operated at 15 kV with a 30 V sweep field. The rise-time of the high voltage pulse was $\approx$ 40 nsec and its width was about 400 nsec. The sensitive time was about 2.5 μ sec.

The chambers were viewed by three cameras, one 16' above each chamber, and one 32' away downstream viewing both chambers. For each chamber, four sides were covered by fiducial plates as described in Appendix 2. On the top of each chamber was a field lens consisting of eight prisms machined on a lucite plate, simulating a lens with a focal length of 16'. On the downstream end was a field lens consisting of a section of a spherical lens of focal length 32'.

This camera system provided stereo views of each chamber for the reconstruction of the events, as discussed in Appendix 2. The top views were called the θ-views and the end view was called the ϕ-view.

The film advancing mechanism and the spark chamber pulsing system allowed the photographing of only one event per AGS beam pulse. In view of the trigger system, which provided a sample rich in desired events, this limitation was not serious.

J. Monitoring

1) Scalers. Thirty-one scalers were used to keep track of various counting rates. The most important ones were TOF $\bar{p}$, TOF $\bar{p} \cdot V_{rear}$, Compute, N, $N \cdot \phi$, $N \cdot \phi \cdot K$, and (coincidence > 1) or (channel > 1) for each hodoscope. After a run, the rates were graphed in the form of a histogram on two-cycle semilog tracing paper. If there was a previous run at the same beam momentum, the histograms from the two runs were matched together, normalized by the TOF $\bar{p}$ rates (antiproton counts). If there was a change in the various rates greater than statistics would allow, the reason was investigated.

2) PDP5 - BS2. A PDP5 computer was connected on-line in this experiment as a part of the monitoring system. The electronic interface between the CC1 and the PDP5 was called BS2 (buffer-storage 2). It was necessary because the CC1 could process events in a much shorter time ($\sim$ 150 nsec.) than the PDP5 ($\sim$ 13 msec.). The BS2 was capable of storing eight 12 bit words. For this experiment, the numbers it handled were the six hodoscope channel numbers and the two θ-channel sums. It was possible to load data into the buffer for any combination of the conditions "Compute," "N," "ϕ," and "K."

The PDP5 was programmed to count the pairs of θ channel sums in four 16 x 16 matrices (called A, B, C, and D). The PDP5 also accumulated histograms of the counts of ϕ-channel sums, the counts of all the counters in each of the hodoscopes, and the counts of all the channels in each of the hodoscopes. An oscilloscope was connected to the PDP5, and was capable of displaying on-line any of

the histograms, or of displaying any of the matrices with a 16 x 16 dot grid, showing which matrix elements had more than a preset number of counts.

In normal operation, matrix A was used to store the counts of θ_{left}-channel sum 23 to 38 vs. θ_{right}-channel sum 23 to 38, and the oscilloscope was used to display the same matrix. To check the working condition of the CC1 kinematic matrix, the BS2 was gated on $N \cdot \phi \cdot K$, and the oscilloscope was watched to see whether, after a period of time, every desired element in the matrix registered at least one count, indicating that all the transistors in the CC1 matrix were functioning properly.

For most of the runs, the BS2 was triggered by $N \cdot \phi$. Fig. 2.7 shows a PDP5 printout of the matrix A. The line indicates the region of the "K" requirement in the CC1 matrix.

At any point of a run, the PDP5 could be interrupted, and called upon to print out on a teletype any part of the stored information. For every run, the individual counter rates were graphed to check whether all of the counters were functioning normally. This was found to be a very powerful monitoring method to keep the ninety counters in the hodoscopes in good working condition.

3) BS1 - system. For every spark chamber picture, the counter numbers of the counters that detected the passage of charged particles, the θ-channel sums, and the ϕ-channel sum were fed from the CC1 into a buffer storage called BS1. The information was stored while used in the following ways:

i) The information was punched on a data processing card by an IBM card punch. The punched cards, called "BS1 cards," were later used to calculate hodoscope inefficiency (Chapter 5, Section C). For the

0	3	2	3	5	13	9	2	2	5	7	7	4	4	4	4
2	5	2	6	11	16	5	13	7	9	9	7	13	13	14	21
2	10	14	12	11	18	14	8	18	12	14	13	25	39	39	21
7	8	13	11	16	17	19	15	24	15	36	50	48	36	6	9
12	11	10	21	34	22	34	37	41	71	76	50	42	34	32	30
10	10	9	21	22	23	40	59	133	84	59	31	24	29	17	22
8	6	11	12	26	36	77	169	119	60	23	25	26	22	149	341
5	8	13	17	27	55	183	142	60	40	30	42	274	885	917	441
5	8	8	11	45	117	123	64	64	59	115	790	1460	727	125	16
4	5	16	24	78	116	55	34	48	137	1104	1185	225	37	24	17
7	4	11	43	80	46	27	28	89	1056	1038	114	22	20	26	10
4	7	18	51	51	37	26	35	750	1197	122	28	19	19	18	10
5	6	34	46	48	33	18	215	1402	291	16	21	18	17	16	13
6	11	49	30	28	32	33	727	777	41	15	9	19	10	10	13
3	16	46	12	21	28	116	900	140	17	12	7	13	10	12	4
6	33	19	14	27	29	270	511	22	17	15	26	8	7	7	7

Fig. 2.7 PDP5 matrix "A" printout for nominal beam momentum 1.75 GeV/c. PDP5 was gated by the condition "N·ϕ"

two lowest beam momenta, they were also used to impose the kinematic condition on the events to be measured (Chapter 2, Section H).

ii) The information about the counter numbers was used to flash corresponding lights on a panel inside the experimental control trailer such that the counters for each event could be seen at a glance. This was a very useful check that the CC1 was functioning properly.

iii) The same information was used to flash appropriate counter numbers attached to the spark chambers, which were photographed with the tracks (Fig. 3. 1). These lights were called BS1 lights. Their use in the analysis process is described in Chapter 3, Section C.

4) Visual monitoring. At the beginning of each run, the spark chambers were inspected visually for malfunctioning. The rolls of film of the spark chamber pictures were developed day by day and scanned for camera or fiducial system failure.

III. SCANNING AND MEASURING

A. Introduction and Summary

The two thin-plate kinematic spark chambers were viewed by three cameras: one for the two ϕ-views and one each for the two θ-views. Fig. 3.1 shows a typical event. The lines running across the spark plates are fiducial lines. A detailed description of the fiducial system is given in Appendix 2. All the measurements were made with respect to these fiducials, and each track was completely reconstructed in three-dimensional space from the measurements.

The angles made by the two tracks with the beam direction determined the calculated mass of the particles in the final state, as will be described in the next chapter. The distance of nearest approach and the coplanarity of the two reconstructed tracks were used for putting necessary conditions on the acceptance of the event as a single interaction with a two-body final state.

Certain standard distances on the spark chamber pictures were also measured as checks on the measurer and the measurement equipment. A measurement was rejected and the event remeasured unless these distances fell within acceptable limits.

Several hundred spark chamber pictures were taken in the course of the experiment with the chambers triggered by the passage of cosmic ray particles. For these pictures, the tracks in the two chambers were collinear with each other. They were analyzed to provide a determination of the measurement accuracy. It was found that the accuracy in the measurements of angles was $\pm 1/2^{o}$. This accuracy was sufficient for the separation of the $\pi^{\pm}$-pair and $k^{\pm}$-pair annihilation events.

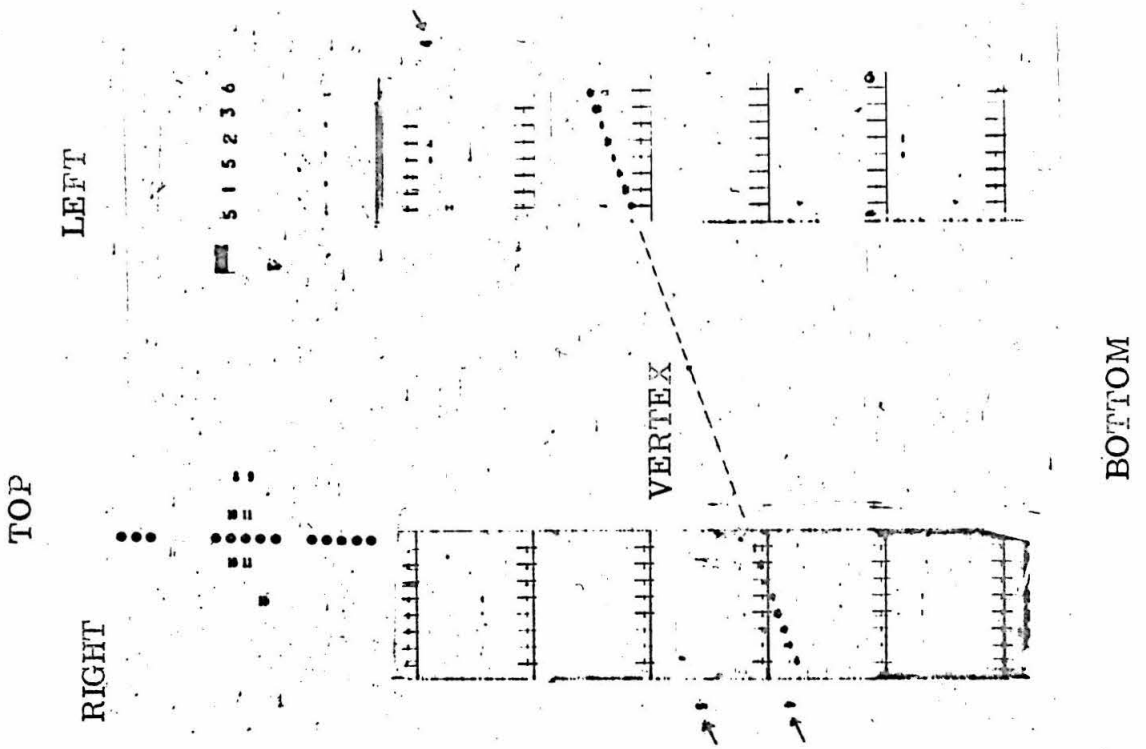

(a) ϕ-view

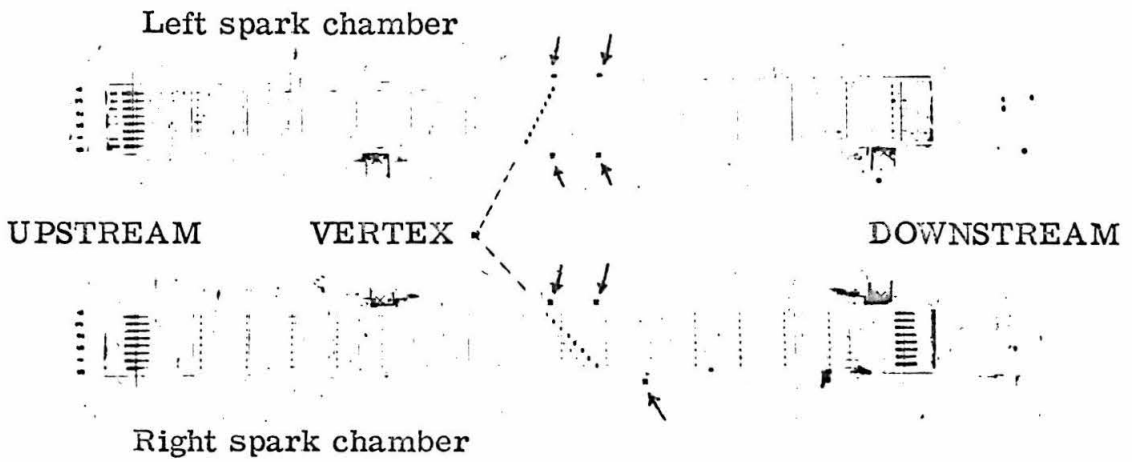

(b) θ-views

Fig. 3.1 Spark chamber pictures
(BS1 lights are indicated by arrows)

Several hundred annihilation events were remeasured and the results were compared with those of the previous measurements. It was found that the scanning inefficiency was $1.5 \pm 0.5\%$.

B. Reconstruction of Events

a) Measurement procedure

The measurement table was equipped with a device similar to a drafting machine. It was capable of measuring both angles and positions on the measurement table. Appendix 3 contains a schematic drawing of this device and also gives a description of its function and calibration.

For each event, the pictures of the spark chambers were projected onto the measurement table one at a time. For each view, the information from four measurements was digitized and punched out on an IBM 526 card punch. Figure 3.2 shows the position of the measurement arm for each of these measurements. They are:

1) The position of any point on the left-hand-most fiducial.

2) The orientation of the first fiducial to the left of the second spark in the track (the sparks of each track were ordered in the direction away from the target). That is, the lengthwise line of the cross-hair on the measurement arm was aligned with that fiducial. The position of the cross was not important.

3) The orientation of the track and the position of the center of the second spark in the track.

4) The position of the end closer to the target of the first fiducial to the right of the one used in 2).

Only fiducials on the planes closer to the cameras were used, since their images were more visible.

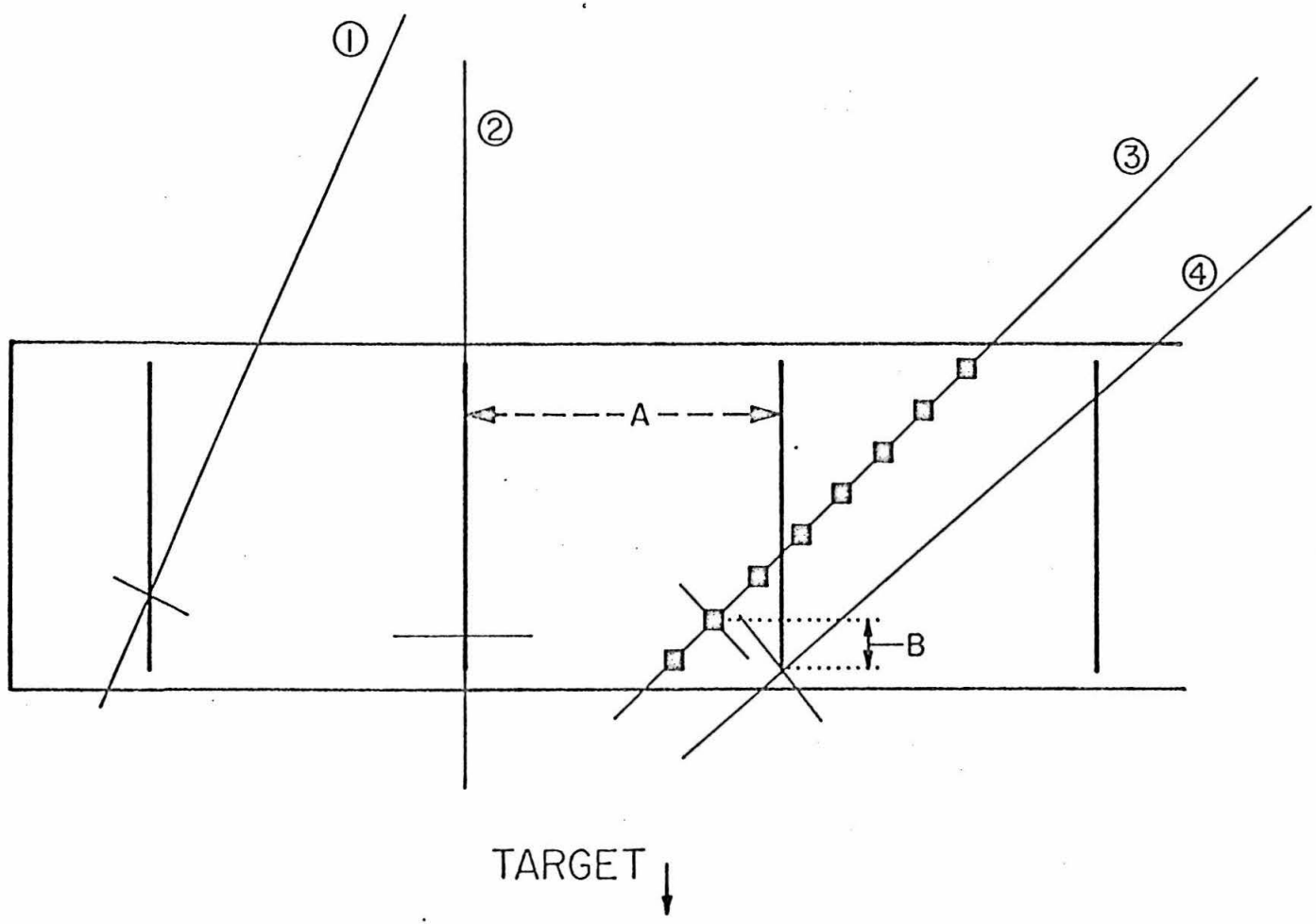

Fig. 3.2 The four steps in the measurement procedure

Measurements 2) and 4) defined one fiducial unit on the measuring table (distance "A" in Fig. 3.2). Then 1) and 2) indicated which fiducial was the first one to the left of the second spark, by giving the distance in fiducial units between this fiducial and the left-hand-most fiducial. Measurements 2) and 3) supplied the apparent angle between the track and the fiducials. This angle and measurements 3) and 4) gave the apparent transverse distance between the center of the second gap and the end of the first fiducial line to the right of the second spark (distance "B" in Fig. 3.2). For a given view, the value of this distance and that of one fiducial unit as measured on the measuring table were fixed within certain limits. These values were printed out for each view in the preliminary computer output and were used as a check on both the measurer and the measurement equipment.

In measuring the apparent angle and one fiducial unit, only the fiducials closest to the track were used, thus minimizing the effect of optical distortion.

The information for each view of the chambers was punched out on one IBM data processing card, with the event number.

b) Geometric reconstruction

From the measurements described in the previous section, the apparent position of a track relative to the fiducial system was completely determined. Putting together the information from both the ϕ and the θ views of a track (end and top views), the track could be completely reconstructed in real space (for detail, see Appendix 2). A right-handed coordinate system was chosen such that the beam direction was $\vec{z}$, the $\vec{y}$ direction pointed vertically up, and the $\vec{x}$ direction pointed at the left chamber away from the target -- left and

right were defined with the observer standing upright and looking downstream along the beam line. The surveyed center of the target was chosen to be the origin.

A track was described by four parameters Q, R, S, T such that the track coordinates obeyed the equations

$$y = Qx + R$$

$$z = Sx + T.$$

The geometry of a two-body final state was thus completely defined by eight numbers:

Left	Right
QL, RL, SL, TL	QR, RR, SR, TR

The track angles are given in terms of these numbers, as follows:

$$\theta_L = \cos^{-1}\left(SL/\sqrt{1+QL^2+SL^2}\right) = \theta \text{ - left}$$

$$\theta_R = \cos^{-1}\left(SR/\sqrt{1+QR^2+SR^2}\right) = \theta \text{ - right}$$

$$\phi_L = \sin^{-1}\left(QL/\sqrt{1+QL^2}\right) = \phi \text{ - left}$$

$$\phi_R = \sin^{-1}\left(QR/\sqrt{1+QR^2}\right) = \phi \text{ - right}$$

$$\phi \equiv 1/2\,(\phi_L + \phi_R)$$

The center of the shortest line perpendicular to both tracks was taken to be the "vertex" of the event and was denoted by three co-ordinates (X, Y, Z). The length of this line was the "distance of nearest approach" (DONA) for the event.

C. The Measurement Routine

a) Selection of tracks

With the help of the hodoscopes, the spark chamber pictures had a very high percentage of events of interest (about 60% at 1.5 GeV/c). Thus, on most of the film, no visual selection for candidates was made. However, because the kinematic spark chambers had a sensitive time of about 2.5 microseconds, there were often extra tracks from general background radiation in the pictures. The measurers were given a procedure for making proper selections from these tracks.

In Fig. 3.1, small numbers can be seen on the sides of the chambers. These numbers, called BS1 lights, were flashed during an event to indicate which counters in the hodoscopes registered the passage of a charged particle. The positions of the BS1 lights and their corresponding counters were roughly the same.

The ϕ-views were measured first, since both ϕ_R and ϕ_L were on the same film. In the case of more than one track in one of the chambers, the measurer was instructed to choose and measure the track most nearly collinear with a track in the other chamber. However, if there were two sets of collinear tracks, the pair that agreed with the position of the illuminated numbers (BS1 lights) was chosen for measurement. Usually, this choice could be easily made. In rare cases, the two pairs of nearly collinear tracks were very close to each other. Then, the pair that fired the hodoscope was selected by using a template which was made to the scale of the picture image on the measuring table and which had the properly scaled cross section of the hodoscope drawn in. Whenever more

than one track was present in one of the ϕ-views, the measurer was instructed to write down on a scan-sheet the spark characteristics of the track that was used. For example, a typical track might have been described by: w, s, m, vs, s, w, w, m, where w stood for "weak," s for "strong," m for "missing" and v for "very." When the θ-view of this event was projected, the track agreeing with this description was chosen. If there was ambiguity, a θ-view template was used. With this technique, unresolvable pictures were reduced to less than one in two thousand.

b) Preliminary output routine

The bulk of the pictures was measured in blocks of 100 events. The cards with the same event number were then grouped together and sent with the analysis program to the Caltech computer. The computation was divided into two parts:

1) Each event was reconstructed geometrically to obtain the eight parameters, from which ϕ, $\Delta\phi(\equiv \phi_L - \phi_R)$, DONA, X, Y, Z, θ_R and θ_L were calculated.

2) The "characteristic distances" in each view were calculated. These are the distances A and B shown in Fig. 3.2, measured in inches.

This preliminary analysis was run every day to monitor the reliability of the measurement equipment. Two forms of output were obtained. One was a BCD card for each event, called the "QRST card." This card contained the event number, the eight geometric parameters and the nominal beam momentum. The other was a printed preliminary output containing a listing of all the quantities calculated.

c) Measurement cycle

A cycling flow diagram is shown in Fig. 3.3. The dotted squares denote measurements made by measurers. Solid squares are outputs. Dotted ellipses denote scanning done by a scan-aide and rhombuses designate logical decisions.

A scan-aide looked through the preliminary printed output and picked out all the event numbers within a block that were absent in the sequence. This category was called "missing."

Good "reasons" for an event being "missing" were:

1) film destroyed

2) no complete usable fiducials

3) left or right track had less than four sparks

4) one track could not possibly be consistent with BS1 lights

5) $\Delta\phi > 10^{o}$

6) multiple exposure (film advance failure).

The measurers wrote down the reason for not measuring an event on a scan-sheet.

The scan-aide also did the checking for "scan errors" and "good geometry." A "scan error" was defined as a case when the characteristic distances (A and B in Fig. 3.2) fell out of the following ranges:

θ_L-view		θ_R-view	
A	B	A	B
1.7" - 1.8"	0.25" - 0.40"	1.7" - 1.8"	0.25" - 0.40"

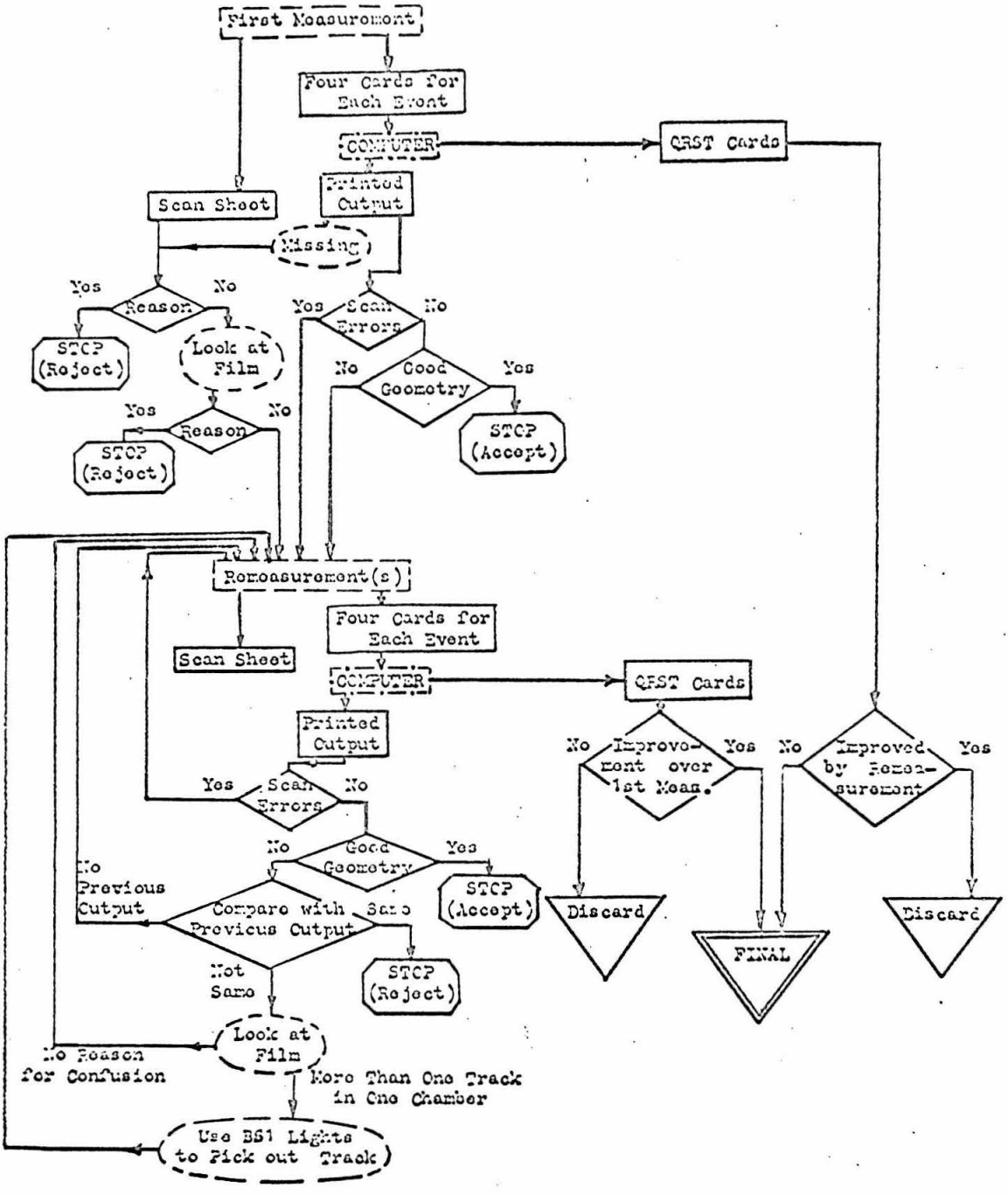

Fig. 3.3 Analysis routine flow diagram

ϕ_L-view		ϕ_R-view	
A	B	A	B
3.7" - 3.8"	0.70" - 1.20"	3.7" - 3.8"	1.00" - 1.30"

A measured event had "good geometry" if the reconstructed tracks led to the results:

$$\text{DONA} \leq 0.5"$$

$$-2" \leq X \leq +2"$$

$$-2" \leq Y \leq +2"$$

$$-40" \leq Z \leq +40" .$$

When comparing a remeasurement with a previous measurement, if the differences were less than 1^{o} in angles and 0.5" in distances, the two measurements were called the "same." Normally, if the angles were the same, the distances also agreed.

If an event was missing without good reason, displayed a scan error, or failed to meet the "good geometry" conditions, it was remeasured. Remeasurement continued until two successive sets of measurements were in agreement.

The remeasurements detected many of the measurers' errors, and the routine converged quite rapidly. In general, the measurements had to be cycled at most three times. Table 3.1 gives an idea of the convergence at three antiproton beam momenta. After the second remeasurement, $\lesssim$ 0.5% of the events remained unacceptable.

TABLE 3.1 The Convergence of the Measurement Cycle

Nominal Beam Momentum (GeV/c)	Total # Pictures	Preliminary Measurement			First Measurement		Second Measurement	
		Accept	Reject	Missed	Accept	Reject	Accept	Reject
1.000	2856	2447	321	88	287	34	26	8
1.750	3503	2845	375	283	306	69	50	19
2.500	2385	1860	339	186	293	46	38	8

D. Measurement Accuracy

The accuracy of the measurements was checked in two ways. Firstly, several hundred pictures were taken with the spark chambers triggered by the passage of cosmic ray particles. They were measured and the results are summarized in Figs. 3.4a and 3.4b. The accuracy in measuring angles was thus about $\pm 1/2^{o}$. The angular accuracy needed for the experiment has been discussed previously and this measurement accuracy was quite adequate. As will be seen in the next chapter, the actual experimental angular resolution was mainly determined by uncertainties considerably larger than the measurement error.

The displacement of the peak of the $\Delta\phi$ distribution was not fully understood, and indicated some systematic error in the fiducial system survey. There was a similar, but smaller, systematic shift evident in the cosmic ray data for $\theta_L + \theta_R$. These shifts did not affect the experiment.

A second check was to remeasure, with the same routine described above, 10% of several blocks of 2000 pictures. A one-to-one comparison was made, and the measurement inaccuracy found was consistent with the cosmic ray data. This method also showed that the loss of events due to measurement errors was $1.5\% \pm 0.5\%$.

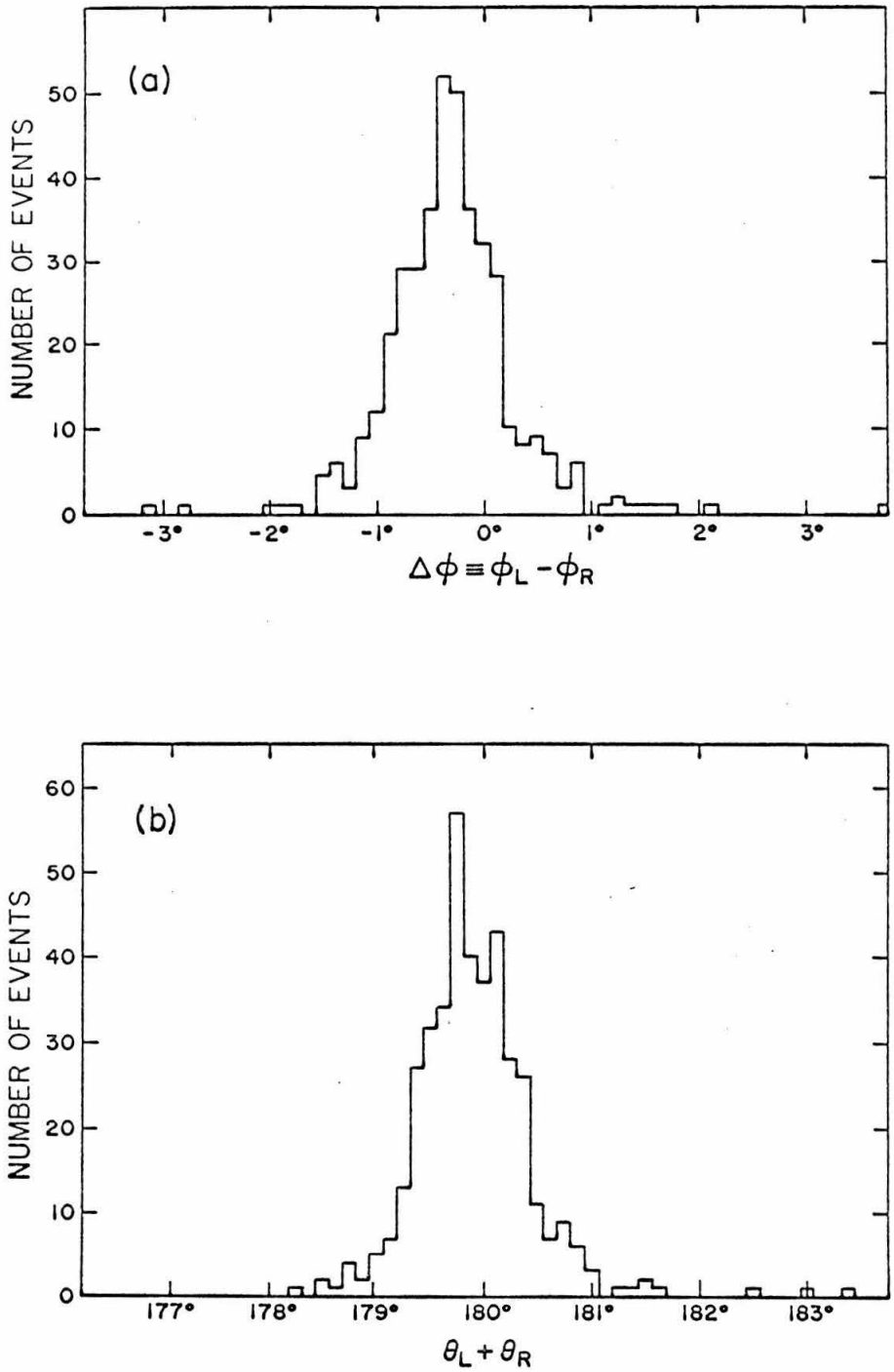

Fig. 3.4 Measurement accuracy check
- Results of cosmic ray picture measurements

IV. DATA REDUCTION

A. Introduction and Summary

Assuming the reaction,

$$\bar{p} + p \rightarrow \text{two particles of equal mass, } m,$$

the value of m^2 was calculated for each event from the incident antiproton momentum and the laboratory angles of the final state particles. An m^2-histogram was graphed for all the events at each of the fifteen antiproton beam momenta. In each histogram, two distinct peaks were present, corresponding to the two charged-meson-pair annihilation modes. The widths of the peaks were mainly due to the $\pm$ 3.5% beam momentum spread.

The values of m^2 at which the peaks appeared were somewhat lower than m_π^2 and m_k^2, and this was found to be most likely due to an error of about 3.5% in the calibration of the beam momentum. For each run, the antiproton momentum was assumed to be that for which the $\pi^\pm$-pairs in the m^2-distribution occurred at the value of m_π^2, 0.0195 GeV^2. The $k^\pm$-pair peak then also occurred at the value of m_k^2, 0.244 GeV^2.

A $\Delta\phi$-histogram was also graphed for the data at each momentum. The full-width at half maximum was found to be about 2^o, and was mainly due to the angular divergence of the incident beam.

From the above-mentioned histograms, conditions on $\Delta\phi$ and m^2 were determined for the acceptance of events:

$\bar{p} + p \rightarrow \pi^+ + \pi^-$	$\bar{p} + p \rightarrow k^+ + k^-$
$-0.12 \leq m^2 \leq 0.14$ GeV^2	$0.14 < m^2 \leq 0.35$ GeV^2
$-2.5^o \leq \Delta\phi \leq 2.0^o$	$-2.5^o \leq \Delta\phi \leq 2.0^o$

The following conditions were also set, corresponding to requiring that the event had a well defined origin inside the hydrogen target:

$$-2'' \leq X \leq 2'',$$

$$-2'' \leq Y \leq 2'',$$

$$-40'' \leq Z \leq 40'', \text{ and}$$

$0.5'' \geq$ DONA (distance of nearest approach of the reconstructed tracks). The loss of events due to all these conditions was studied, and was found to be negligible (i.e., < 1%).

The events at each antiproton momentum were distributed, according to their values of m^2 and $\Theta_{LC.M.}$ (the left-side center-of-mass angle), in the form of a two-variable histogram. Such a histogram was called a $\Theta_{LC.M.}$-m^2 matrix. For each antiproton momentum, two such matrices were made, one for the events which satisfied all the acceptance conditions on X, Y, Z, DONA, and $\Delta\phi$, and one for those which did not. The latter matrix was used to evaluate the background in the former and, after a background subtraction, the $\pi^{\pm}$-pair and $k^{\pm}$-pair angular distributions were obtained.

Because no magnets were used in this experiment to determine the charges of the final particles, $\Theta_{C.M.}$, defined as the angle

between the direction of the original antiproton and that of the final negatively charged meson, could be either $\Theta_{LC.M.}$ or $\Theta_{RC.M.}$ (the right-side center-of-mass angle). The $\Theta_{LC.M.}$ - m^2 matrices were therefore folded and summed symmetrically with respect to $\Theta_{LC.M.} = 90^o$. The cross sections obtained from the counts were expressed as $[\frac{d\sigma}{d\Omega}(\Theta_{C.M.}) + \frac{d\sigma}{d\Omega}(\pi - \Theta_{C.M.})]$.

To obtain the final cross sections, it was necessary to consider:

(1) the total number of antiprotons which produced the final counts of desired events,

(2) the different lengths of the target available for different values of $\Theta_{C.M.}$,

(3) the attenuation of the flux of the antiproton beam along the target due to antiproton-proton interactions, and

(4) other various systematic errors due to the design of this experiment.

The first three factors are discussed in this chapter, and preliminary cross sections are presented in 5^o steps of $\Theta_{C.M.}$. Other systematic corrections are discussed in the next chapter.

B. Kinematics

As described in the last chapter, the following geometric values were calculated for each event: θ_L, θ_R, ϕ_L, ϕ_R, $\Delta\phi$, X, Y, Z, and DONA. For kinematic fitting, each event was assumed to be an annihilation into two particles of equal masses. With the additional information about the incident momentum of the antiproton, the center-of-mass angle Θ and the mass of the particles in the final state could be calculated.

For annihilation into particles of identical masses m,

$$m^2 = \frac{1}{E^2}\left\{\frac{1}{4}(E^4-Q^4) - \frac{Q^2}{\sin^2(\theta_L+\theta_R)}\left[ME(\sin^2\theta_2+\sin^2\theta_R) + Q^2\sin^2\theta_L\sin^2\theta_R\right]\right\}, \qquad 4.1$$

where θ_L, θ_R are the two polar angles of the final particles in the laboratory, c(velocity of light)=1, and

Q = momentum of antiproton at interaction,

M = mass of proton = mass of antiproton, and

E = total interaction energy.

The center-of-mass angle Θ of an interaction is given by

$$\sin\Theta = \frac{Q \sin\theta_L \sin\theta_R}{\sin(\theta_L + \theta_R)} \Big/ \sqrt{\frac{1}{2} ME - m^2}\,. \qquad 4.2$$

Because no magnets were used to determine the charges of the particles in the final state, Θ and its supplement are indistinguishable, as implied in Eqn. 4.2.

Since the hydrogen target was 80" long, the energy loss of the antiprotons in the beam was not negligible. Thus, the value of Q in Eqns. 4.1 and 4.2 was a function of Z -- the location of the vertex in the target. To get the functional dependence, the range-momentum curve for protons in hydrogen[6] was used. The curve was differentiated graphically to obtain d(momentum)/d(distance) as a function of the proton momentum, and an empirical fit was made. The density of liquid hydrogen was taken to be 0.069 gm/cm^3. Then,

$$Q = S + \frac{dQ}{dZ}\,(Z + 40), \qquad 4.3$$

where S was the momentum of the antiproton upon entering the target, and Z was in inches.

For $2.75 \geq S \geq 1.20$ GeV/c,

$$\frac{dQ}{dZ} = -(2.48 - 1.34\,S + 0.264\,S^2) \times 10^{-3}\ \text{GeV/c/inch}, \qquad 4.4a$$

and for $S < 1.20$ GeV/c,

$$\frac{dQ}{dZ} = -(6.81 - 8.63\,S + 3.33\,S^2) \times 10^{-3}\ \text{GeV/c/inch}\,. \qquad 4.4b$$

Fig. 4.1 shows the fit for dQ/dZ.

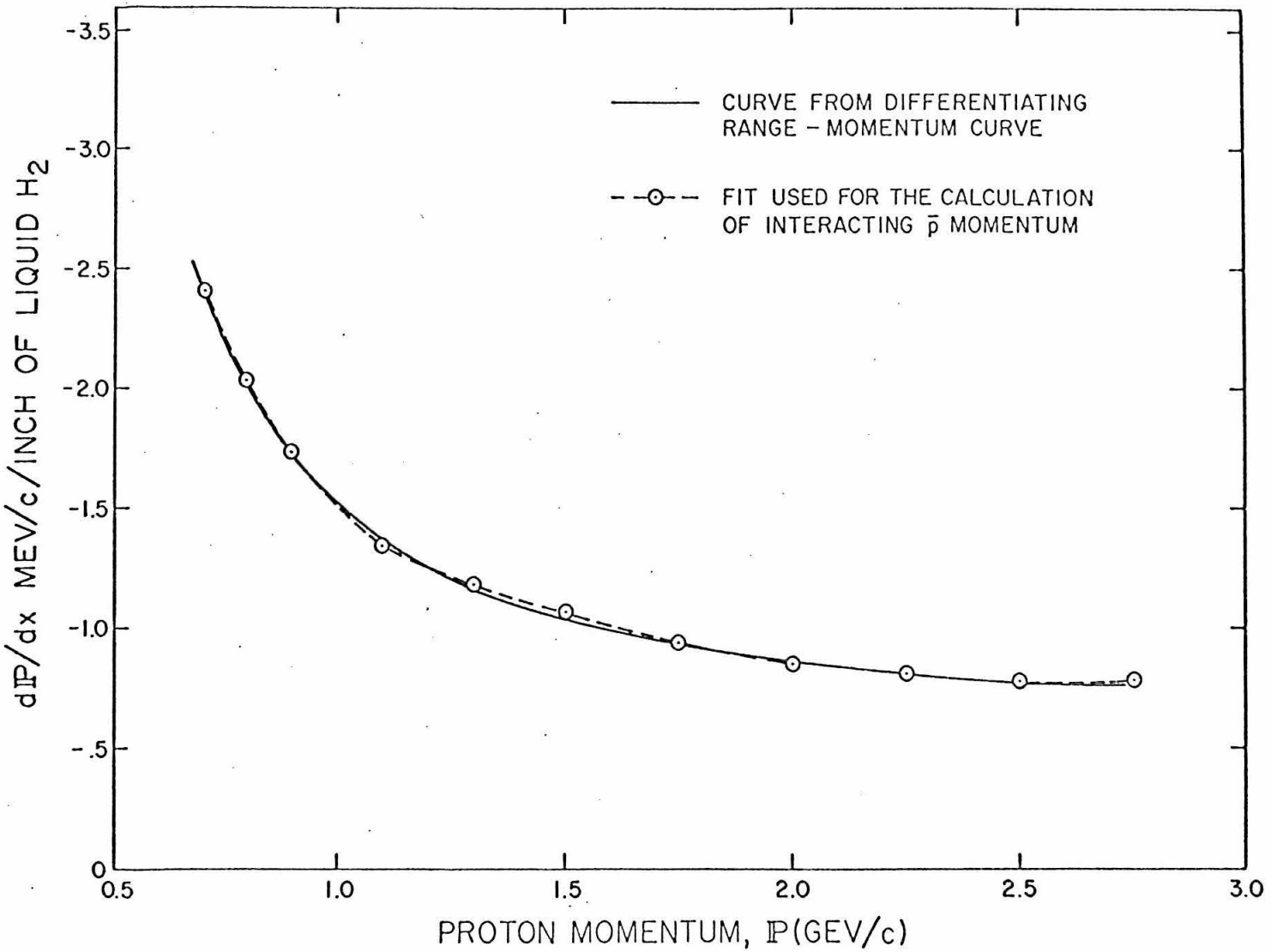

Fig. 4.1 Momentum loss of proton in liquid hydrogen, H_2 density = 0.069 gm/c.c.

It should be emphasized that the kinematical analysis proceeded on the assumption that all beam particles had a given momentum and direction. The actual spread in momentum and in direction of the incident antiprotons contributed to uncertainties in m^2, $\Delta\phi$, and the polar angles of the final particles. This will be discussed later.

C. One Variable Histograms

Since the hodoscopes had fairly generous conditions for the acceptance of events, there was background mainly due to events with more than two final particles. To separate out the $\pi^+\pi^-$ and k^+k^- events, stricter requirements were put on $\Delta\phi$, X, Y, Z, DONA(distance of nearest approach), and the calculated mass. These requirements were mainly determined by studies of $\Delta\phi$ and m^2 distributions.

The 1.75 GeV/c data will be used as an example here; the data at the other momenta were quite similar.

a) $\Delta\phi$-distribution

The angle $\Delta\phi$ measured the departure from collinearity of the tracks as seen in the ϕ-view. For collinear tracks, $\Delta\phi = 0$.

Figure 4.2 is a $\Delta\phi$-histogram of all the analyzed events for 1.75 GeV/c beam momentum that had $\Delta\phi$ within the range $\pm 4.3^{\circ}$. Above the background, there is a peak, centered at $-1/4^{\circ}$, with full-width at half maximum (FWHM) of about 2°.

The 1/4 degree shift in the peak position was attributed to a systematic surveying error, while the spread of this $\Delta\phi$ distribution could be understood in terms of the following reasons:

1) Beam divergence. For antiprotons not travelling precisely in the z-direction, the tracks of the particles from a two-body annihilation would not be collinear as seen from the ϕ-view. Thus, beam divergence gave rise to a spread in $\Delta\phi$. The beam divergence could be calculated from the beam optics and from the multiple scattering in the target.

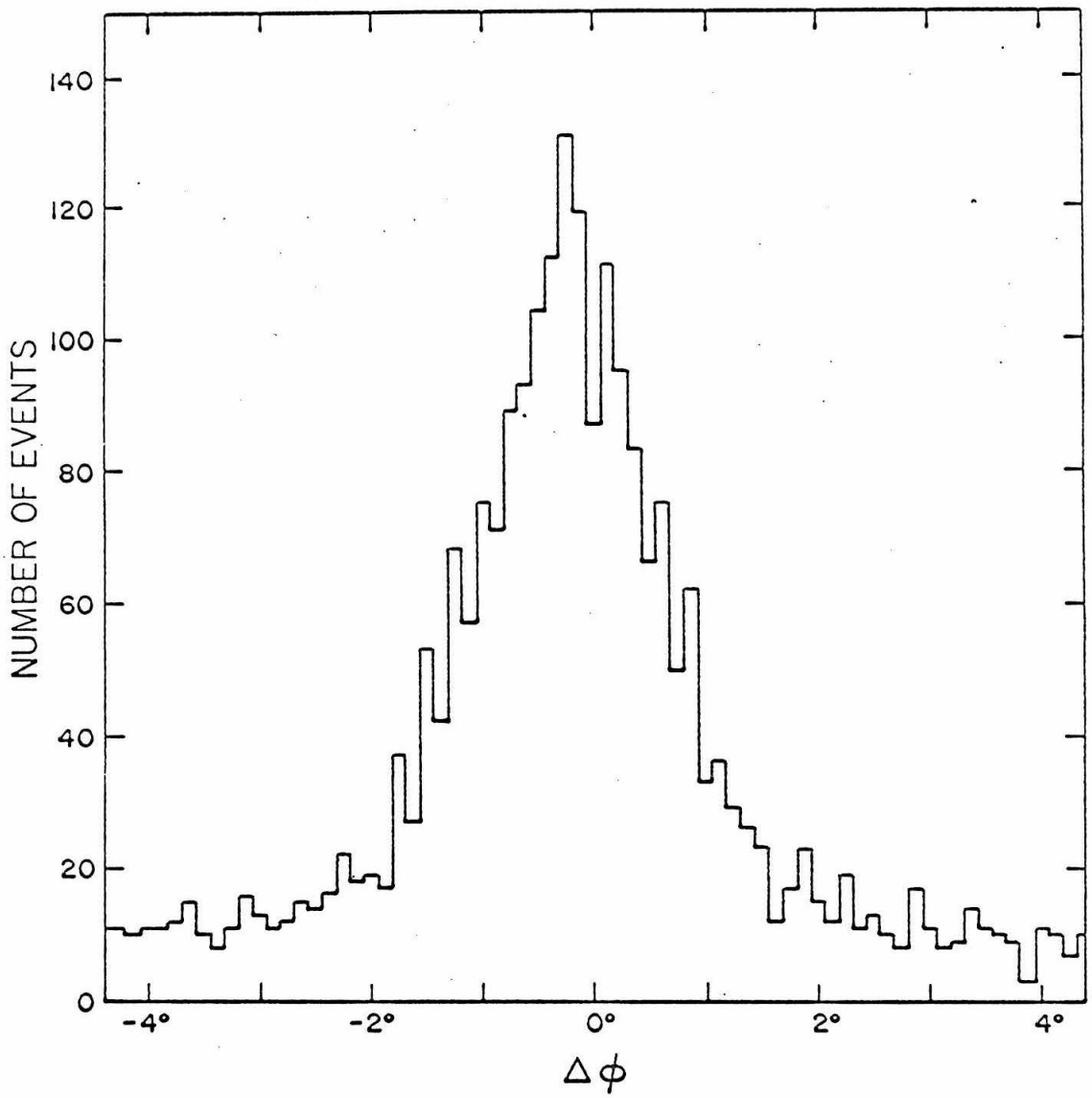

Fig. 4.2 $\Delta\phi$ histogram for the events for 1.75 GeV/c nominal beam momentum

2) Measurement inaccuracy.

3) The multiple Coulomb scattering of the final particles in going through the target, counters, and the spark chambers.

From each of these sources of error listed above, a full-width at half maximum for the $\Delta\phi$ distribution was estimated, as shown in the table below. They were then combined quadratically to estimate the net width of the $\Delta\phi$ distribution. The agreement between the estimated and observed widths was reasonable.

Cause of uncertainty in $\Delta\phi$		FWHM
Beam divergence: 1) Angular spread in the design of the beam		1.5^{o}
2) Multiple scattering in the target		0.7^{o}
Angular measurement inaccuracy:	Left track	1^{o}
	Right track	1^{o}
Multiple scattering of final particles:		$\cong 0.3^{o}$ (Negligible)
	Quadratic sum	2.2^{o}
	Observed	2^{o}

b) m^2-distribution

Figure 4.3 is an m^2-distribution of all the 1.75 GeV/c events that had m^2, as calculated with Eqn. 4.1, from -0.19 to

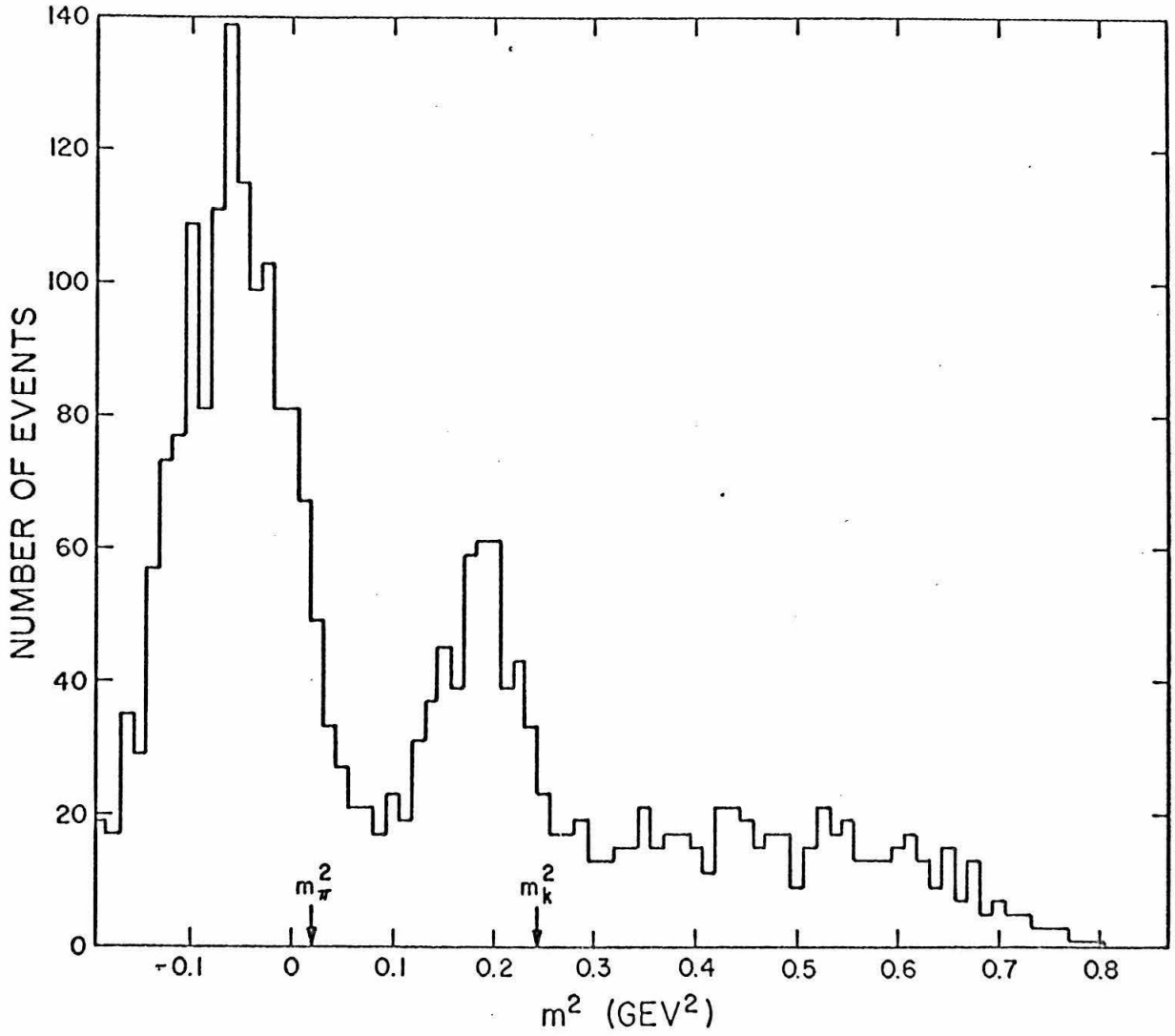

Fig. 4.3 m^2-histogram for the 1.75 GeV/c data without beam momentum adjustment. No limits on $\Delta\phi$, X, Y, Z, DONA were imposed

+0.8 GeV^2. The peaks for $\pi^{\pm}$-pair and $k^{\pm}$-pair events are clearly present, but displaced. This displacement was seen in all the data for all the different incident beam momenta. For 1.75 GeV/c, the beam magnets in the experiment were tuned so that the average interaction momentum was supposedly the nominal momentum, with energy loss in the target taken into consideration. This displacement could therefore be attributed to only two possibilities:

1) A systematic error in the determination of the polar angles of the final particles which could be caused by a bias in the angular measurements and/or an error in the positioning of the spark chambers.

2) An error in the calibration of the beam magnets.

To determine which possibility was most likely, elastic scattering pictures were compared with annihilation pictures. About 350 pictures, which were taken with the spark chambers triggered by conditions "N" and "ϕ" only at nominal beam momentum 2.5 GeV/c, were analyzed. With these trigger conditions (which omitted the kinematic requirement "K"), the pictures were a rich sample of antiproton-proton elastic scattering. Fig. 4.4 is an m^2-distribution for these events. Fig. 4.5 is an m^2-spectrum of the pictures taken at the same beam momentum with the chambers triggered for $\pi^{\pm}$-pair and $k^{\pm}$-pair events. Thus, the $\bar{p}$ p peak was displaced by 0.03 GeV^2 and the $\pi^+\pi^-$ peak by 0.1 GeV^2. From Eqn. 4.1, the following derivatives could be calculated:

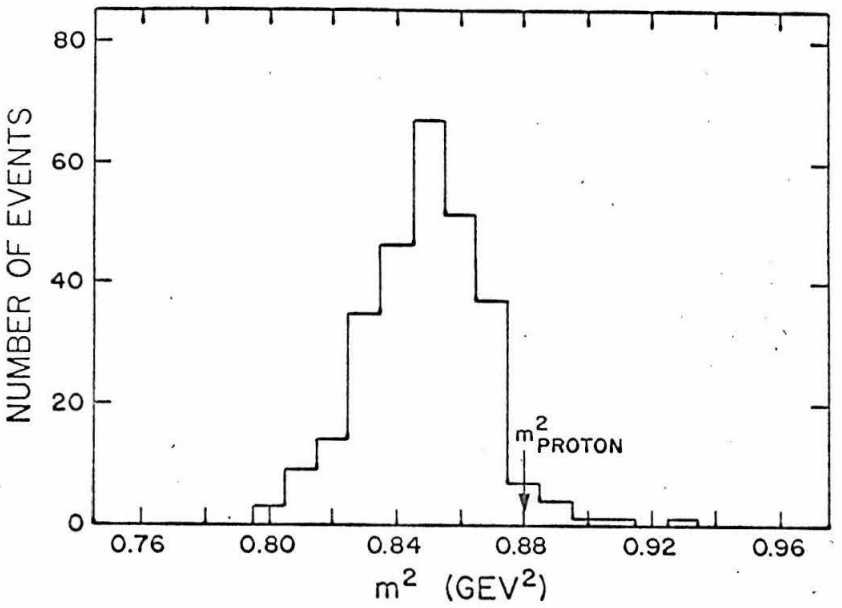

Fig. 4.4 m^2-histogram for antiproton-proton elastic scattering without beam momentum adjustment. Nominal beam momentum = 2.5 GeV/c

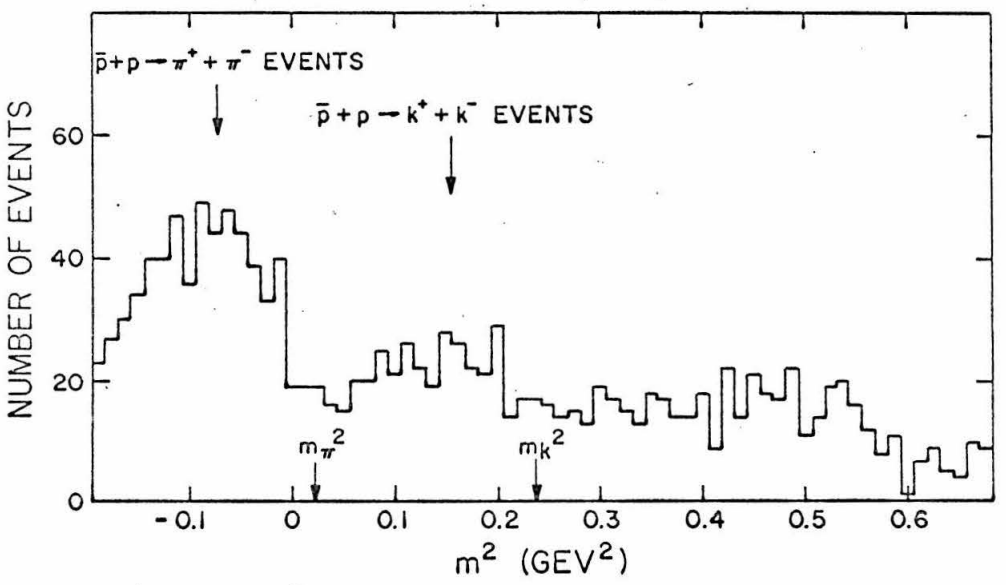

Fig. 4.5 m^2-histogram for spark chamber pictures taken with trigger requirement "N·ϕ·K". Nominal beam momentum = 2.5 GeV/c. No momentum adjustment was made

$$\frac{\partial m^2}{\partial \theta_L} = \frac{2Q^2}{E^2 \sin^3(\theta_L+\theta_R)} \left\{ ME[\sin^2\theta_R \cos(\theta_L+\theta_R) - \sin\theta_L \sin\theta_R] - Q^2 \sin\theta_L \sin^3\theta_R \right\} \qquad 4.5a$$

$$\frac{\partial m^2}{\partial \theta_R} = \frac{2Q^2}{E^2 \sin^3(\theta_L+\theta_R)} \left\{ ME[\sin^2\theta_L \cos(\theta_L+\theta_R) - \sin\theta_L \sin\theta_R] - Q^2 \sin^3\theta_L \sin\theta_R \right\} \qquad 4.5a$$

$$\frac{\partial m^2}{\partial Q} = \frac{Q}{E-M} \left\{ M - \frac{1}{\sin^2(\theta_L+\theta_R)} [M(\sin^2\theta_L + \sin^2\theta_R) + 2\frac{Q^2}{E} \sin^2\theta_L \sin^2\theta_R] \right. \qquad 4.5c$$

The symmetric case, when $\theta_L = \theta_R$, could be shown to give a good average for the data. For $\theta_L = \theta_R$ at 2.5 GeV/c,

$\bar{p} + p \rightarrow \bar{p} + p$

$\frac{\partial m^2}{\partial \theta_L} = \frac{\partial m^2}{\partial \theta_R} = -0.031$ GeV^2/degree

$\frac{\partial m^2}{\partial Q} = -0.26$ GeV-c

$\bar{p} + p \rightarrow \pi^+ + \pi^-$

$\frac{\partial m^2}{\partial \theta_L} = \frac{\partial m^2}{\partial \theta_R} = -0.060$ GeV^2/degree

$\frac{\partial m^2}{\partial Q} = -0.95$ GeV-c

Hence, if the displacement in m^2 was due to a systematic error in the determination of the laboratory polar angles,

$$\frac{\text{displacement for } \bar{p}\,p \to \pi^+\,\pi^-}{\text{displacement for } \bar{p}\,p \to \bar{p}\,p} \approx \frac{-.060}{-.031} \approx 2\,,$$

while if it was due to an error in the calibration of the beam magnets,

$$\frac{\text{displacement for } \bar{p}\,p \to \pi^+\,\pi^-}{\text{displacement for } \bar{p}\,p \to \bar{p}\,p} \approx \frac{-.95}{-.26} \approx 3.7\,.$$

The experimental value of this ratio was $\frac{0.10 \pm 0.005}{0.03 \pm 0.005} \approx 3.3 \pm 0.6$. Therefore, it was concluded that the systematic error was mostly due to the magnet calibration.

For every run, the "average momentum" was adjusted until the $\pi^{\pm}$-pair peak occurred at 0.0195 GeV^2 (m_π^2). Fig. 4.6 shows the adjustments in per cents for the fifteen different beam momenta of this experiment. The average was about 3.5%. Were the error ascribed to a systematic angle error, it would have been about one degree. A table of the adjusted momenta is given in Chapter 6, where all the results from this experiment are presented.

Fig. 4.7 is the adjusted m^2-spectrum for all the events that had values of m^2 from -0.19 to +0.8 GeV^2, obtained from runs with nominal beam momentum 1.75 GeV/c. It is seen that the peak indicating $k^{\pm}$-pair events now also occurs at the correct value of m^2 (0.244 GeV^2). Above the background, the $\pi^{\pm}$-pair peak has a FWHM

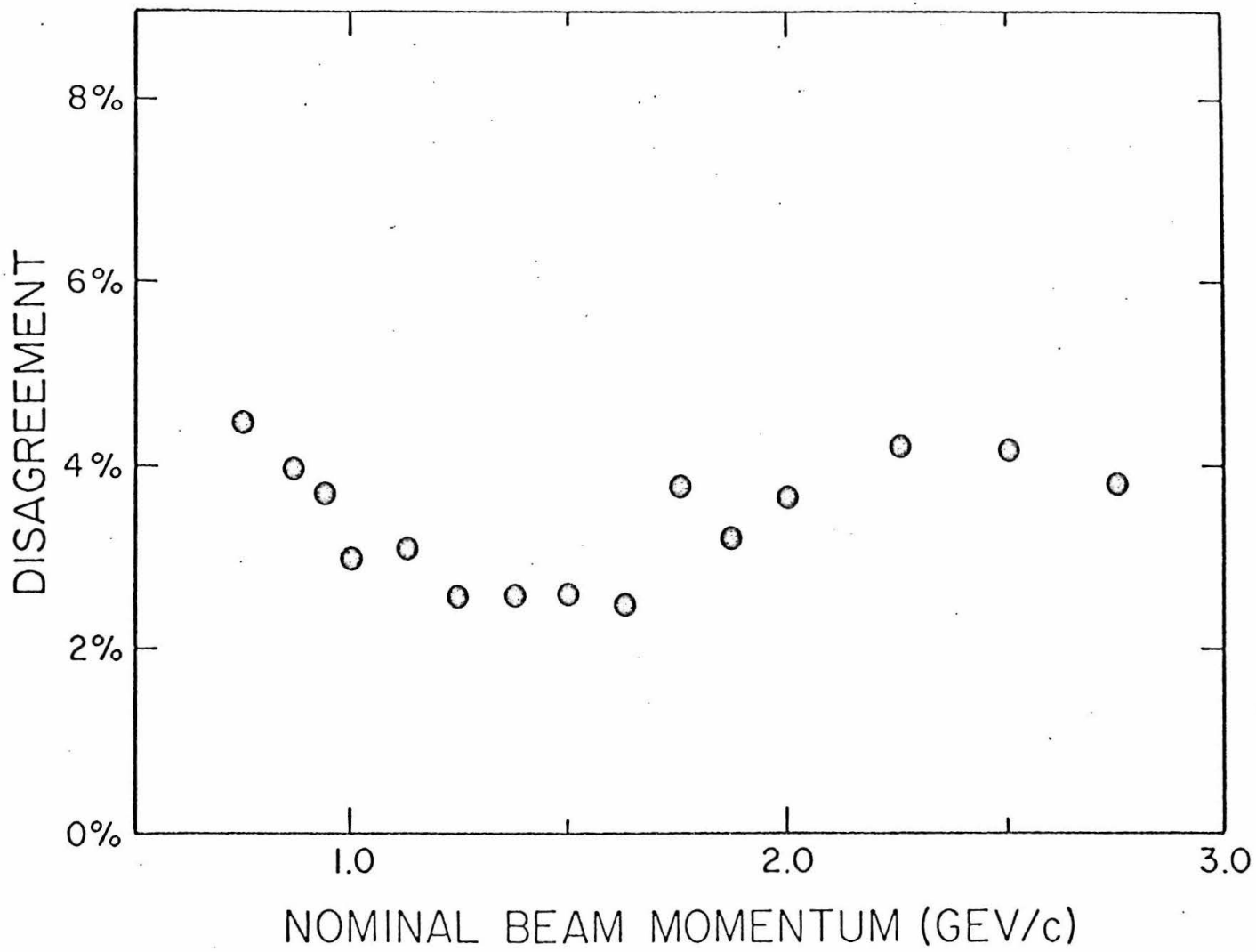

Fig. 4.6 Differences in percents between nominal beam momenta and adjusted beam momenta

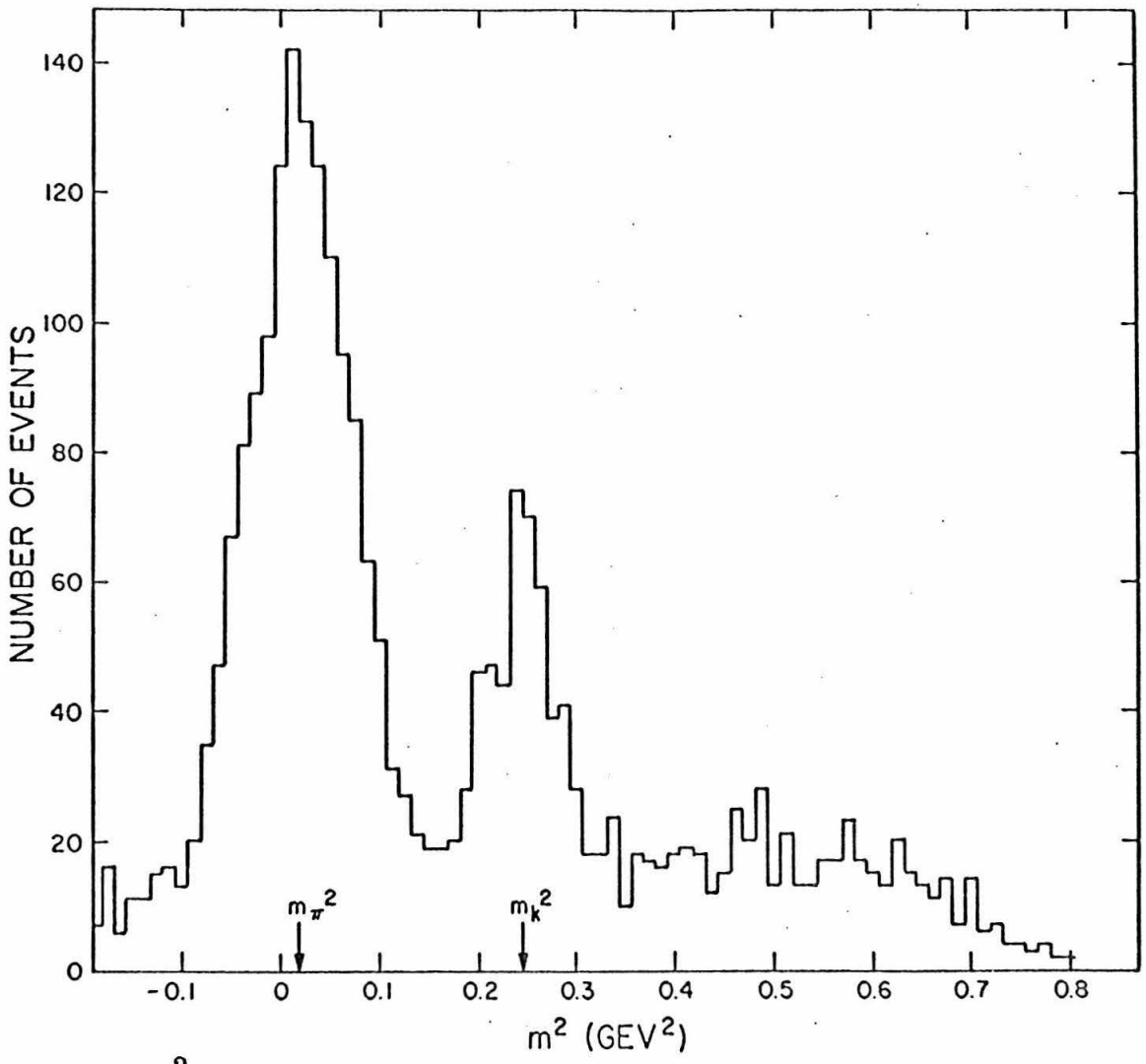

Fig. 4.7 m^2-histogram for the nominally 1.75 GeV/c data after beam momentum adjustment. No limits on $\Delta\phi$, X, Y, Z, DONA were imposed.

of about 0.14 GeV^2. This spread could be understood in terms of the following reasons:

1) Momentum spread in the beam. The antiproton beam was designed to have a momentum acceptance of ±3%. The actual spread was measured and shown in Fig. 4.8. From Eqns. 4.1 and 4.5c,

$$\left.\frac{dm^2}{dQ}\right|_{m=m_\pi,\ Q = 1.675\ GeV/c} \simeq 1.1\ \text{GeV-c}$$

for all values of θ_L and θ_R. Hence, the FWHM in m^2 from the finite momentum acceptance was $\Delta m^2 \simeq 1.1 \times 1.68 \times \frac{6}{100} \approx .11\ GeV^2$.

2) Angular measurement inaccuracy. The FWHM of an angle measurement was 1^o (see Fig. 3.4). From Eqns. 4.5a and b,

$$\left|\frac{dm^2}{d\theta}\right|_{\theta=\theta_L=\theta_R \text{ at } m=m_\pi,\ Q = 1.675\ GeV/c} = 0.054\ GeV^2/\text{degree}\ .$$

The mass was calculated from the values of two polar angles, therefore, the FWHM in m^2 due to measurement inaccuracy was $\Delta m^2 \simeq 0.054 \times \sqrt{2} \simeq .08\ GeV^2$.

3) Multiple scattering of final state particles when passing through the hodoscopes and spark chambers, and angular divergence of the beam, led to negligible effects.

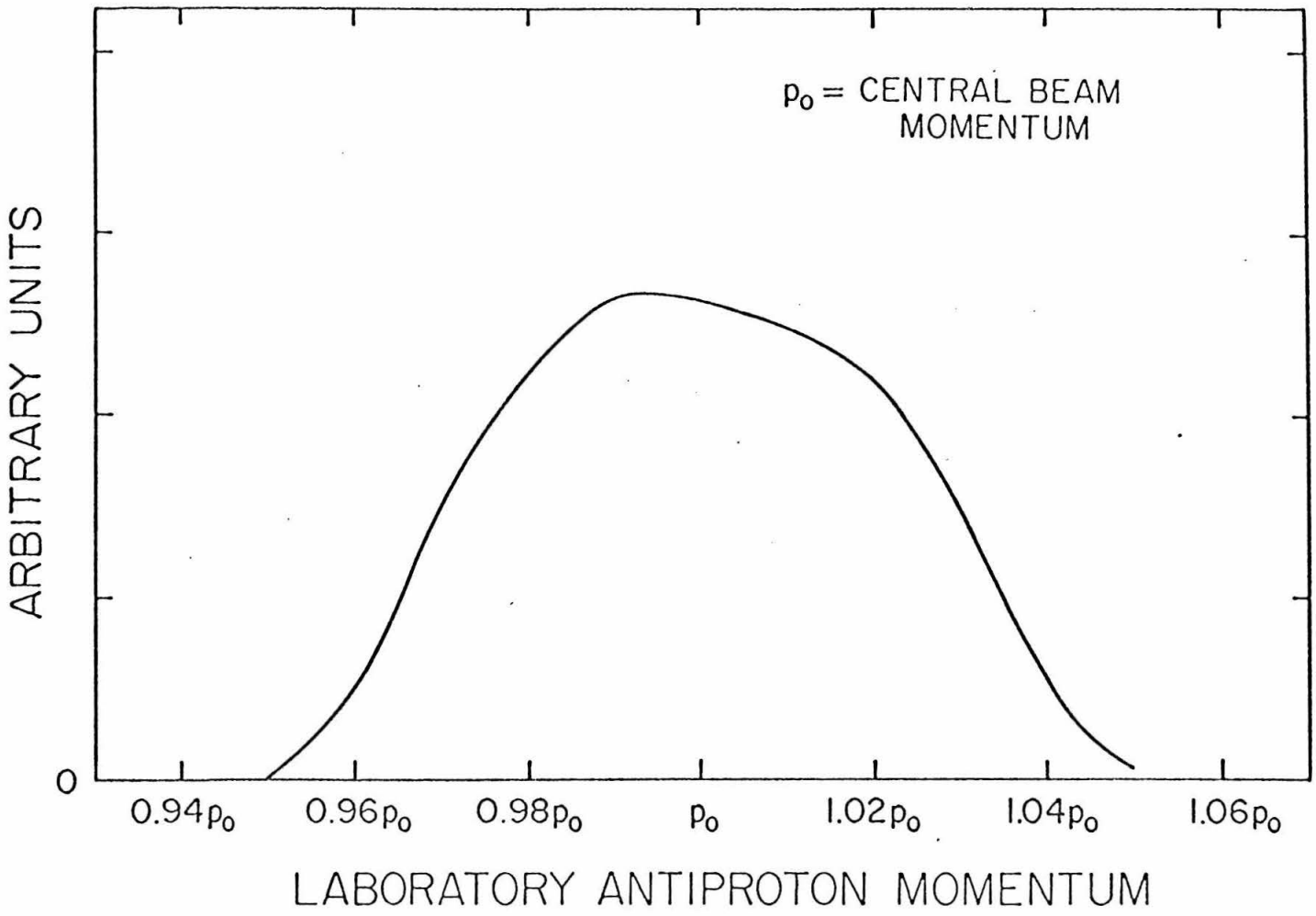

Fig. 4.8 Measured beam momentum spread

Summary

Cause of uncertainty in m^2		FWHM
Beam momentum spread		0.11 GeV^2
Measurement inaccuracy		0.08 GeV^2
Multiple Coulomb scattering of final particles		0.02 GeV^2
Beam divergence		0.03 GeV^2
	Quadratic sum	0.14 GeV^2
	Observed	0.14 GeV^2

D. Conditions for the Acceptance of Events

To obtain the conditions on the values of m^2 for the identification of $\pi^{\pm}$-pair or $k^{\pm}$-pair events, an m^2 spectrum was plotted with a strict requirement on $\Delta\phi$ to get a rich sample of two-body annihilation events. From Fig. 4.2, the requirement was chosen to be $-1.5^{\circ} \leq \Delta\phi \leq 1.0^{\circ}$. Fig. 4.9 is the resulting m^2-histogram. By studying this spectrum, a $\pi^{\pm}$-pair event was defined as one having a value of m^2 in the range from -0.12 to +0.14 GeV^2 and a $k^{\pm}$-pair event as one with m^2 in the range from 0.14 to 0.35 GeV^2. Comparing Fig. 4.9 with Fig. 4.7, it was seen that the widths of the peaks in the m^2-spectrum were not changed by the cut in $\Delta\phi$, but much of the background had been eliminated.

To obtain the conditions on the values of $\Delta\phi$, a $\Delta\phi$-histogram was first made with m^2 limited to $-0.12 \leq m^2 \leq 0.14$ GeV^2 (Fig. 4.10). These were mostly $\pi^{\pm}$-pair events, but there was some background. A $\Delta\phi$-histogram was next plotted with the condition that $m^2 < -0.12$ or $m^2 > 0.35$ GeV^2 (Fig. 4.11). These were the events, which, according to the m^2-histogram Fig. 4.9, were neither $\pi^{\pm}$-pair nor $k^{\pm}$-pair events. Their $\Delta\phi$ distribution showed no peaking, as expected.

The background in Fig. 4.10 was now subtracted by assuming that it had the same distribution as that shown in Fig. 4.11. The counts outside the range -4° to 3.5° (far away from the peak) were used to normalize Figs. 4.10 and 4.11, and as a result, the background in Fig. 4.10 was taken to be 0.336 ± 0.04 times the distribution in Fig. 4.11. Fig. 4.12 shows the result of subtracting the background from Fig. 4.10. From Fig. 4.12, the "coplanarity condition" was defined to be:

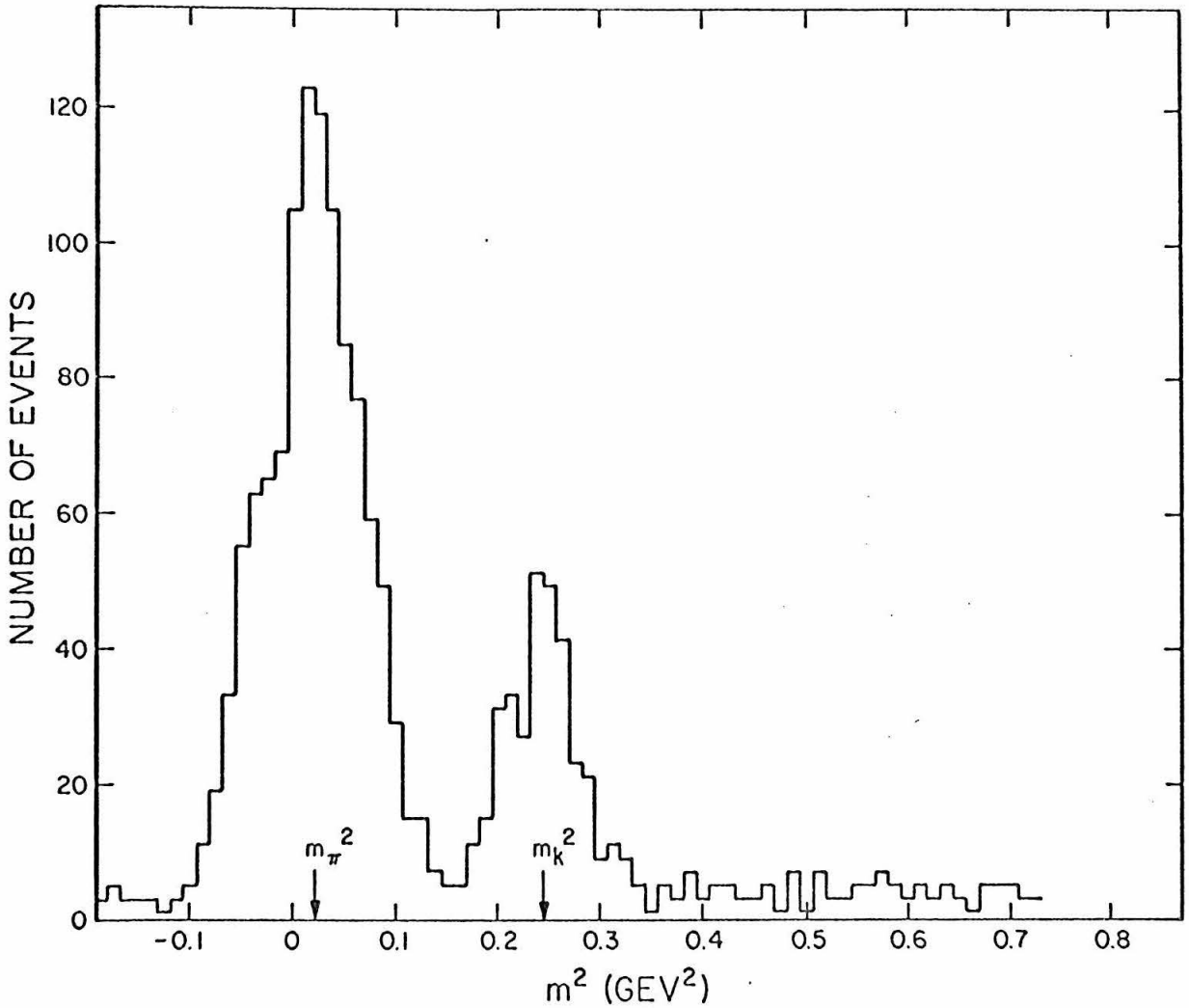

Fig. 4.9 m^2-histogram for nominally 1.75 GeV/c data after beam momentum adjustment. Limits: $-1.5^o \leq \phi \leq 1.0^o$

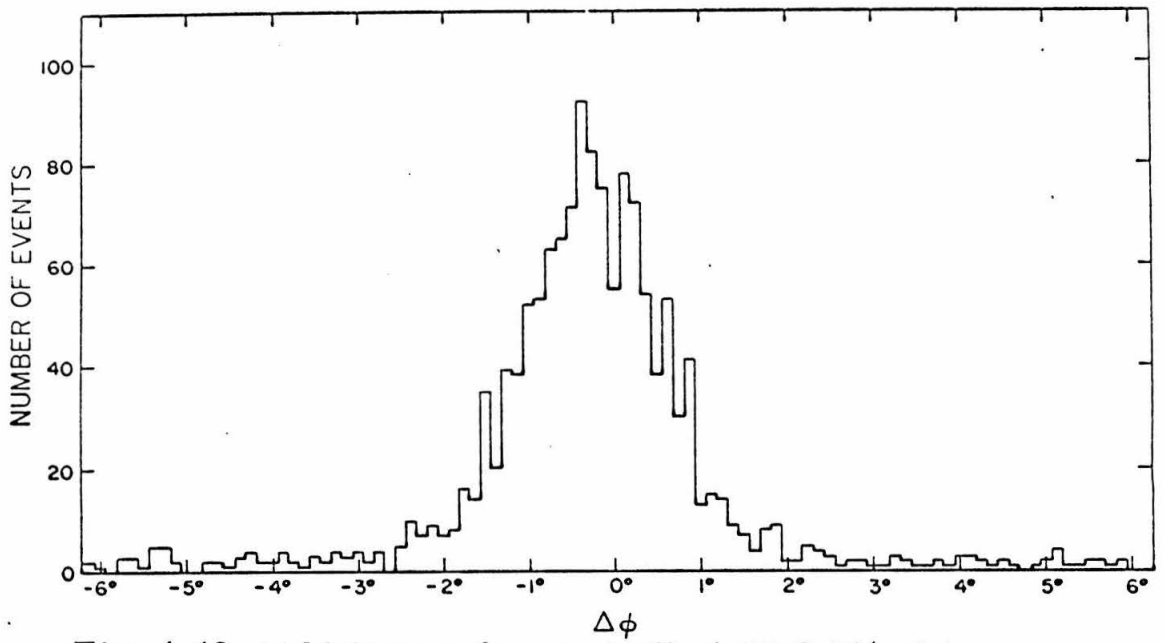

Fig. 4.10 $\Delta\phi$ histogram for nominally 1.75 GeV/c data.
Limits: $-0.12 \leq m^2 \leq 0.014$ GeV^2

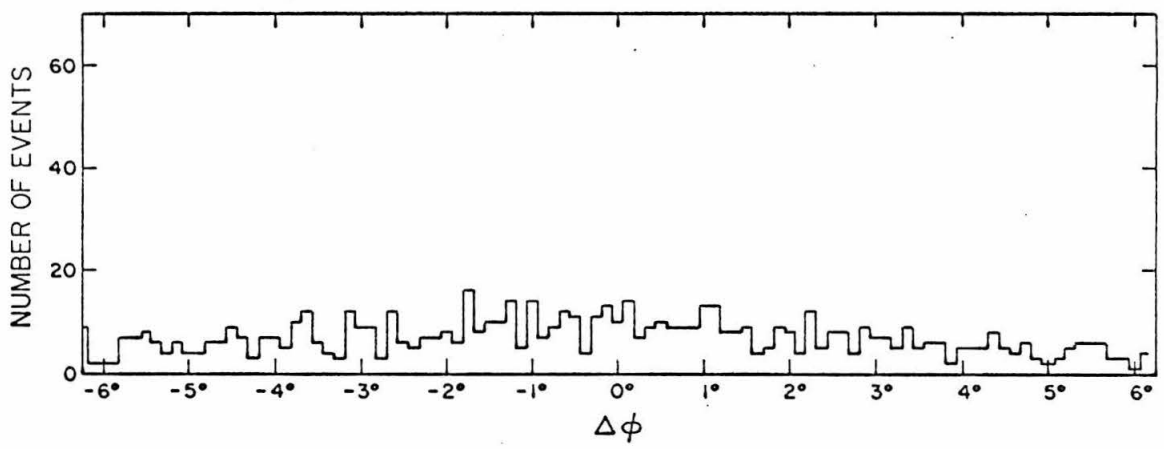

Fig. 4.11 $\Delta\phi$ histogram for nominally 1.75 GeV/c data.
Limits: $m^2 < -0.12$ GeV^2 or $m^2 > 0.35$ GeV^2

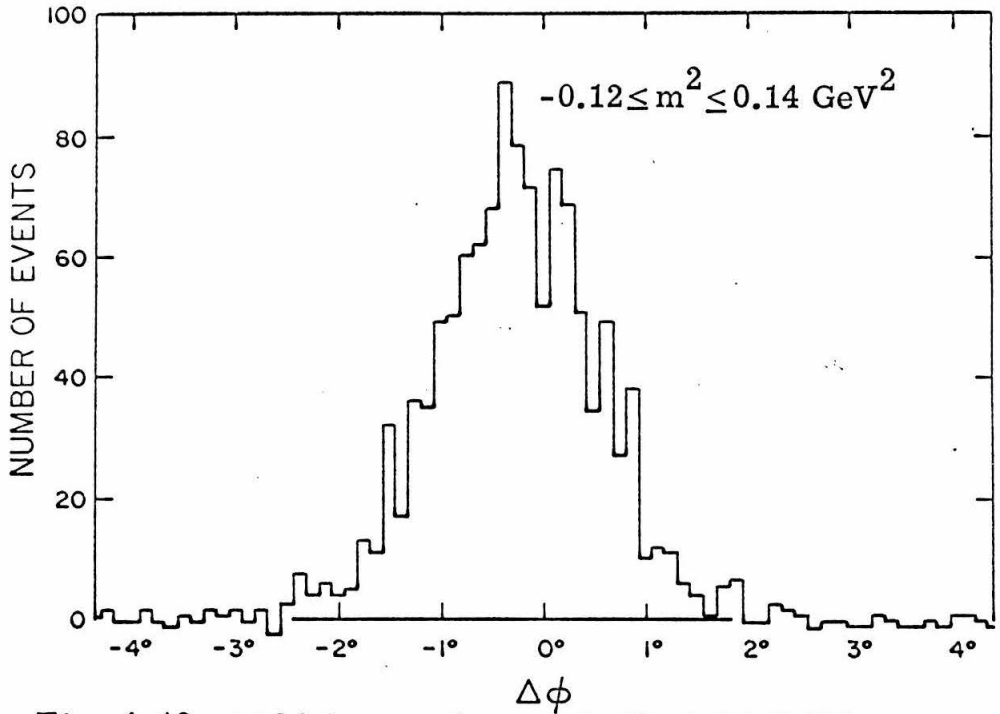

Fig. 4.12 $\Delta\phi$ histogram for nominally 1.75 GeV/c data after background subtraction ($\bar{p} + p \rightarrow \pi^+ + \pi^-$ events)

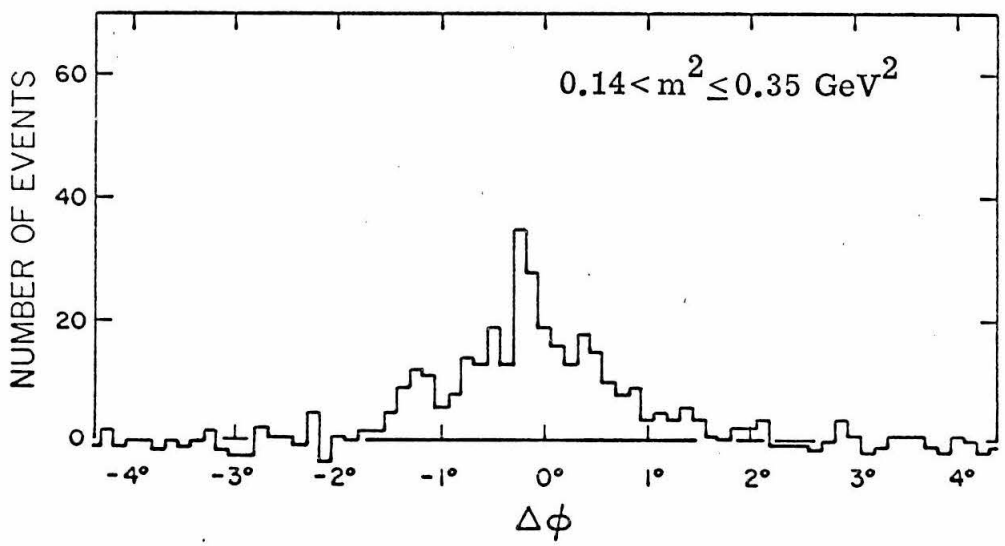

Fig. 4.13 $\Delta\phi$ histogram for nominally 1.75 GeV/c data after background subtraction ($\bar{p} + p \rightarrow k^+ + k^-$ events)

$$-2.5^{o} \leq \Delta\phi \leq 2.0^{o} \quad .$$

By adding up all the counts outside these limits, it was found that the loss of events due to this cut was $0.3 \pm 0.7\%$ and hence negligible. Similar background subtraction was done for the $k^{\pm}$-pair events ($0.14 < m^2 \leq 0.35$ GeV^2). The net $\Delta\phi$ distribution for $k^{\pm}$-pairs is shown in Fig. 4.13, and the above coplanarity condition also caused negligible loss of good events.

Two m^2 histograms were then plotted for events within (Fig. 4.14) and outside (Fig. 4.15) the acceptable $\Delta\phi$ range (-2.5^{o} to 2.0^{o}). Again, assuming the similarity of distribution of background events, the data of Fig. 4.15 were used to subtract the background in Fig. 4.14. From the resulting histogram Fig. 4.16, it could be seen that the following m^2 limits caused negligible ($< 1\%$) loss:

$$-0.12 \leq m^2 \leq 0.14 \text{ for} \qquad \bar{p} + p \rightarrow \pi^+ + \pi^-$$

$$0.14 < m^2 \leq 0.35 \text{ for} \qquad \bar{p} + p \rightarrow k^+ + k^- \quad .$$

The sharp (non-gaussian) cutoff of the $\Delta\phi$ and m^2 distribution was due to the fact that the dominating contributions to their widths, the beam momentum spread and the beam divergence, were not gaussian distributed, but cut off quite sharply.

For the data in Fig. 4.16, the $\pi^{\pm}$-pairs and $k^{\pm}$-pairs were resolved so well that there was no significant correction for the two peaks' overlapping. At all other momenta, this was also found to be true.

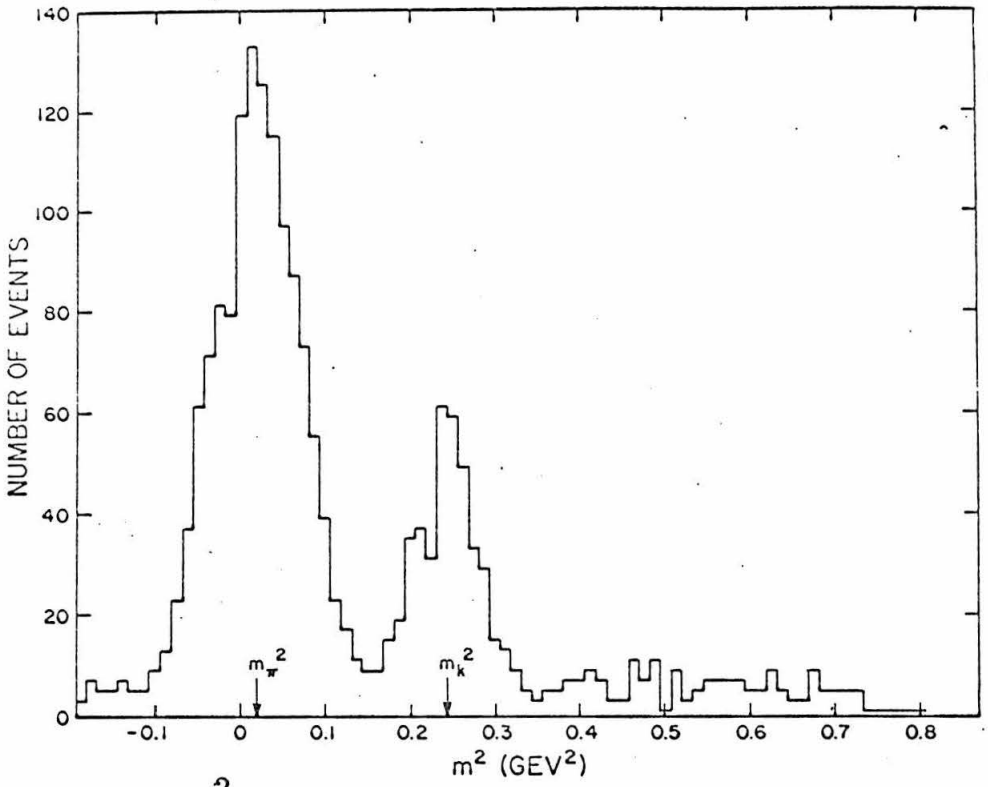

Fig. 4.14 m^2 histogram for nominally 1.75 GeV/c data after beam momentum adjustment. Limits: $-2.5^{o} \leq \Delta\phi \leq 2.0^{o}$

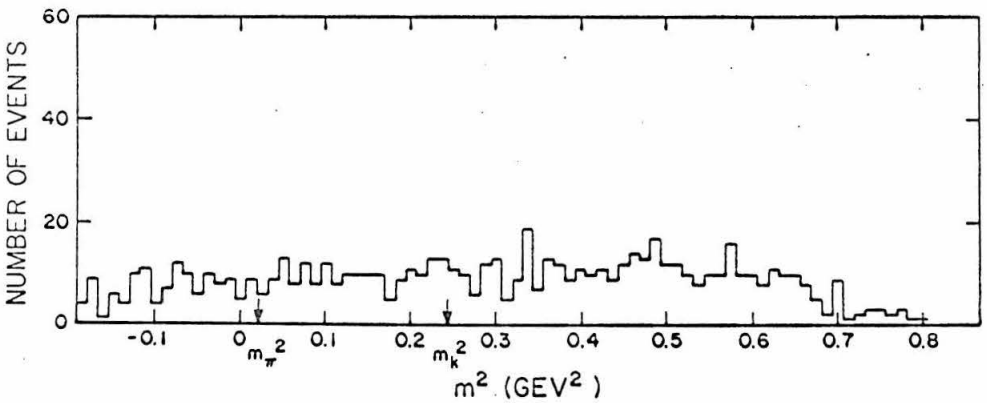

Fig. 4.15 m^2 histogram for nominally 1.75 GeV/c data after beam momentum adjustment. Limits: $\Delta\phi < -2.5^{o}$ or $\Delta\phi > 2.0^{o}$

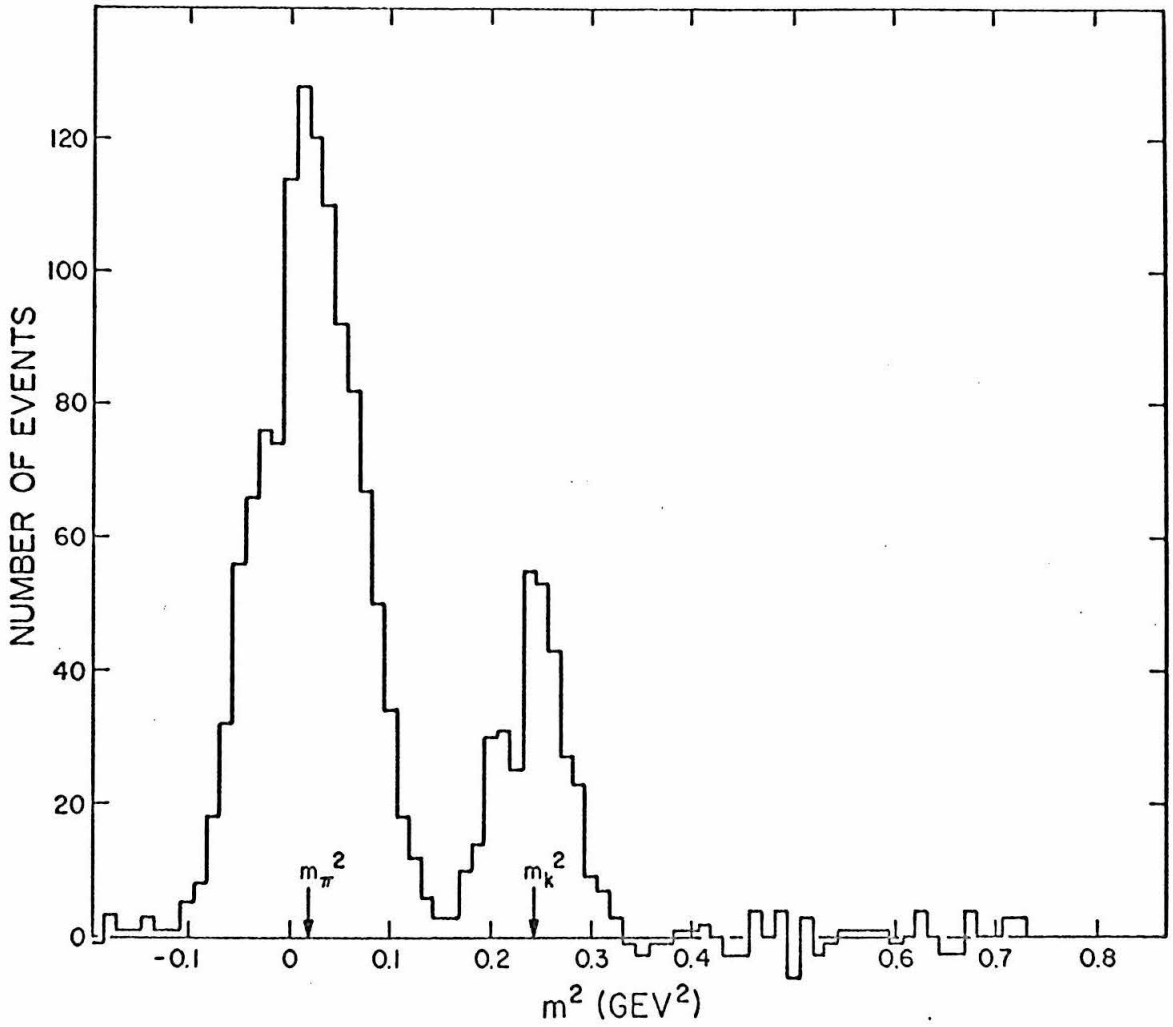

Fig. 4.16 m^2 histogram for nominally 1.75 GeV/c data after beam momentum adjustment and background subtraction. Limits: $-2.5^o \leq \Delta\phi \leq 2.0^o$

Fig. 4.17 is the DONA (distance of nearest approach) histogram for all the events which satisfied the coplanarity and the m^2 conditions for either $\pi^{\pm}$- or $k^{\pm}$-pair annihilations. It showed that a single vertex event could be defined as one with DONA $\leq 0.5''$. The loss due to this condition was again negligible.

Finally, limits on X, Y, and Z were set to insist that the annihilation occurred inside the target:

$$-2'' \leq X \leq 2'' \qquad -2'' \leq Y \leq 2'' \qquad -40'' \leq Z \leq 40''.$$

Figs. 4.18 - 20 are histograms of X, Y, Z for events which satisfied the previously mentioned limits in $\Delta\phi$, DONA, and m^2. Again, no loss was caused by these conditions on X, Y, and Z.

In summary, the limits used to select events were:

Interaction	X	Y	Z	DONA	m^2	$\Delta\phi$
$\bar{p} + p \rightarrow \pi^+ + \pi^-$					-0.12 to 0.14 GeV^2	
	$\pm 2''$	$\pm 2''$	$\pm 40''$	$0.5''$		-2.5° to 2°
$\bar{p} + p \rightarrow k^+ + k^-$					0.14 to 0.35 GeV^2	

The loss of good data which fell outside these limits was estimated to be $\leq 1\%$. There were still a significant number of background events lying within these limits, and the background subtraction will be discussed in the following section.

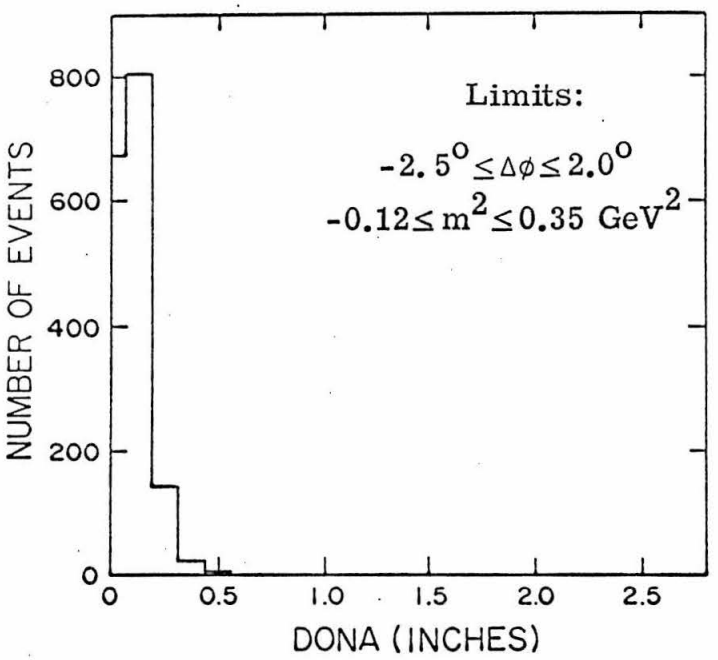

Fig. 4.17 DONA-histogram for nominally 1.75 GeV/c data

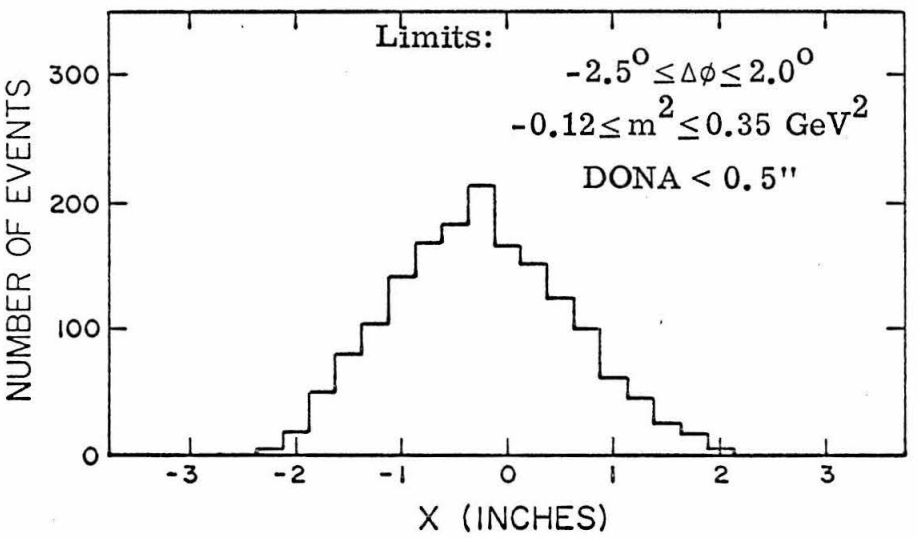

Fig. 4.18 X histogram for nominally 1.75 GeV/c data

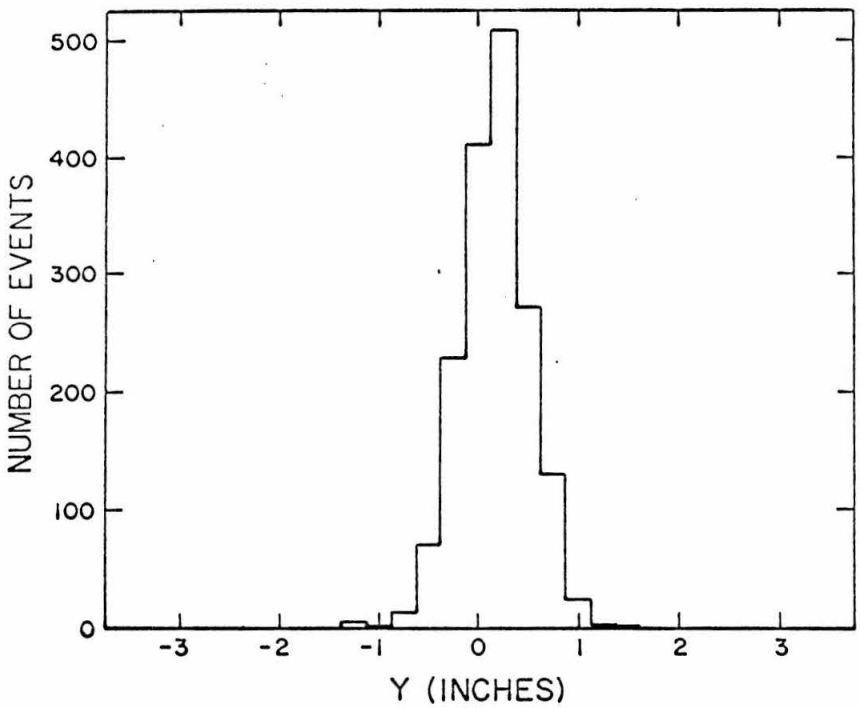

Fig. 4.19 Y histogram for nominally 1.75 GeV/c data.
Limits: Same as Fig. 4.18

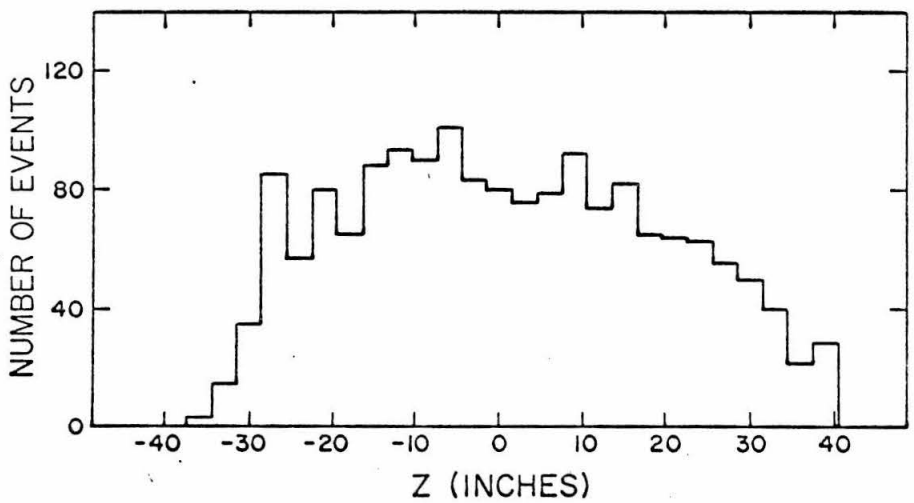

Fig. 4.20 Z histogram for nominally 1.75 GeV/c data.
Limits: Same as Fig. 4.18

E. $\Theta_{LC.M.}$ - m^2 Matrices. Background Subtraction

Fig. 4.21 is a matrix (two-variable histogram) for the 1.75 GeV/c data which satisfied the acceptance requirements on X, Y, Z, DONA, and $\Delta\phi$ for $\pi^{\pm}$-pair or $k^{\pm}$-pair events. The matrix in Fig. 4.22 is the complement of that in Fig. 4.21. It is a two-variable histogram for the 1.75 GeV/c events which did not satisfy the same requirements. The vertical variable of these matrices is m^2, divided in bins of 0.25 GeV^2, and the horizontal variable is the left center-of-mass polar angle, $\Theta_{LC.M.}$, in bins of 5^o.

In calculating $\Theta_{LC.M.}$, Eqn. 4.2 was used. The ambiguity in $\Theta_{LC.M.}$ was removed by insisting that

$$\Theta_{LC.M.} \geq 90^o \text{ if } \theta_L \geq \theta_R, \text{ and}$$

$$\Theta_{LC.M.} < 90^o \text{ if } \theta_L < \theta_R .$$

The value of $\Theta_{C.M.}$ should be defined as the angle between the direction of the final state particle with a particular charge (e.g., the negative particle) and the incident antiproton. Thus, in this experiment, where the charges were unknown, $\Theta_{C.M.}$ could be either $\Theta_{LC.M.}$ or $\Theta_{RC.M.}$ (which was $180^o - \Theta_{LC.M.}$). Because of this ambiguity, the $\Theta_{LC.M.}$ - m^2 matrices would ultimately be folded across $\Theta_{LC.M.} = 90^o$, and the results given as $\left[\frac{d\sigma}{d\Omega}(\Theta_{C.M.}) + \frac{d\sigma}{d\Omega}(\pi - \Theta_{C.M.})\right]$.

M**2 VS CM THETA L HISTOGRAM

LIMITS				
	CPHI	-2.5	TO	2.0
	M**2	NONE		
	MISS	0.5		
	X	-2.0	TO	2.0
	Y	-2.0	TO	2.0
	Z	-40.	TO	40.
	PHI L	NONE		
	PHI R	NONE		
	THETA L	NONE		
	THETA R	NONE		

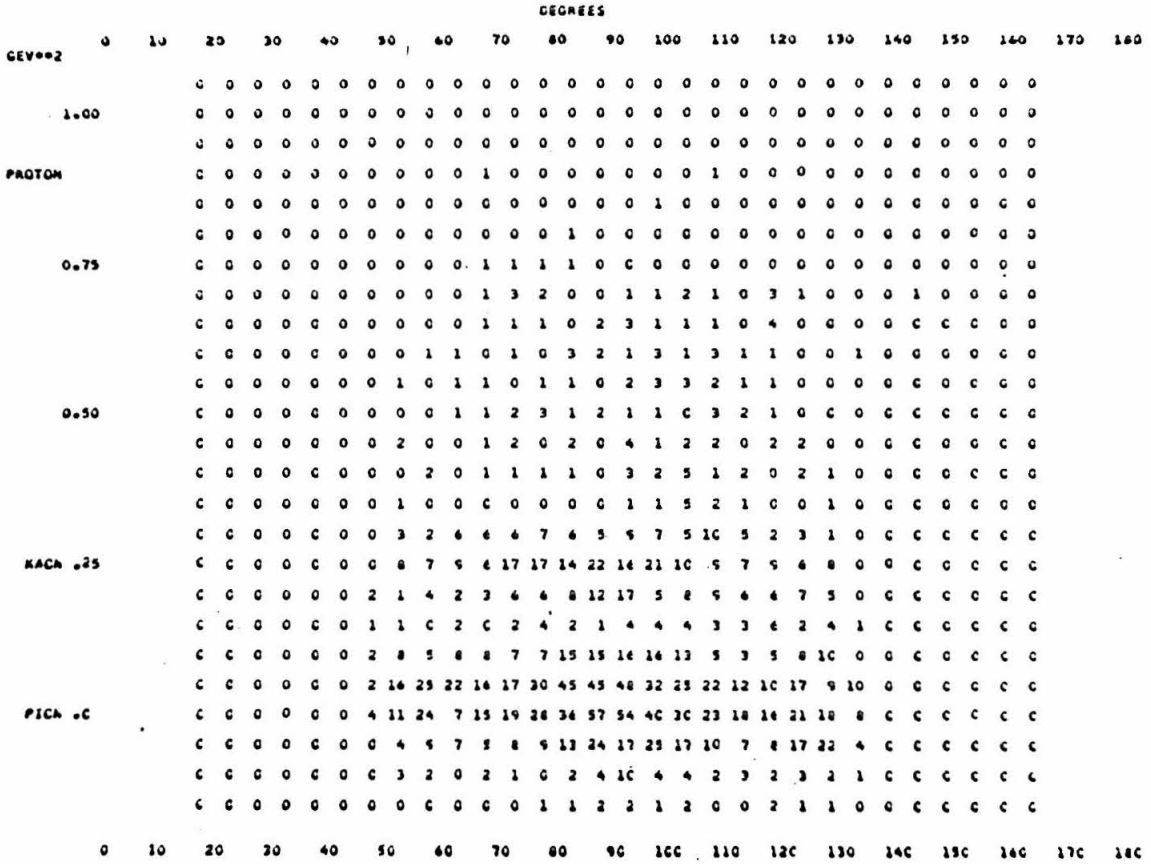

TOTAL NUMBER OF EVENTS PLOTTED HERE 1614

TOTAL NUMBER OF EVENTS COMPLETELY ANALYZED 2967

Fig. 4.21 $\Theta_{LC.M.}$ - m^2 matrix for nominally 1.75 GeV/c data

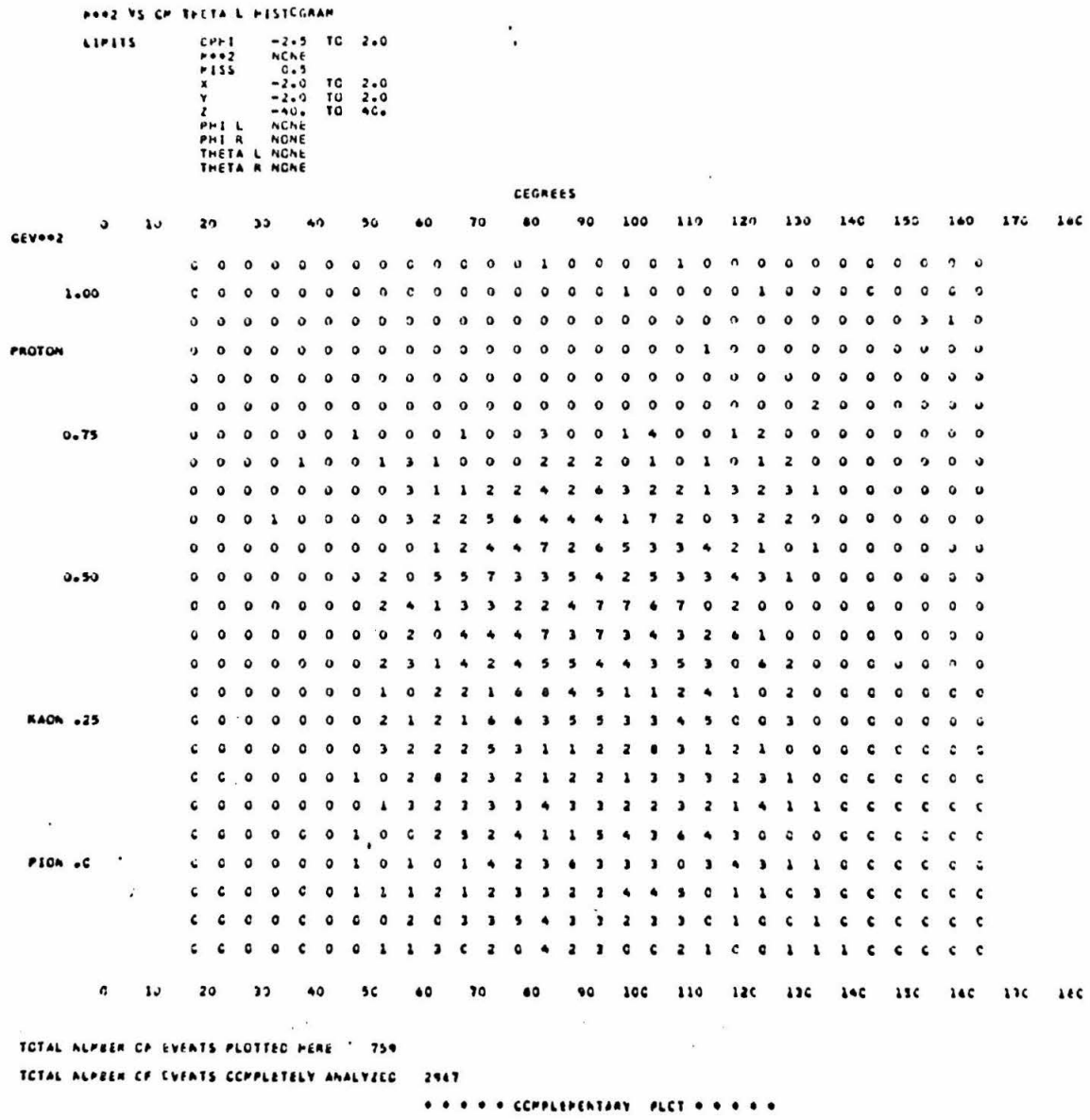

Fig. 4.22 $\Theta_{LC.M.}$ - m^2 matrix for nominally 1.75 GeV/c data. Complement of Fig. 4.21

Background subtraction was done in a manner analogous to that discussed in the previous section. The distribution of the background in the $\Theta_{LC.M.} - m^2$ matrix 4.21 was assumed to be the same as 4.22. In Fig. 4.21, the total count in the range $0.375 \leq m^2 \leq 0.775$ GeV^2 is 108. For 4.22, it is 265. The ratio is 0.407 ± 0.046. Thus, for a given $\Theta_{LC.M.}$ bin, the background in Fig. 4.21 is $0.406\ (1 \pm 0.114)$ times the number of events in Fig. 4.22 in the corresponding matrix element.

When the mass limits for $\pi^{\pm}$-pair and $k^{\pm}$-pair events were applied, and the background was subtracted, the results were as summarized in Table 4.1. For $\pi^{\pm}$-pairs, the background was $\lesssim 10\%$, and the statistical uncertainty in the background did not appreciably increase the uncertainty in the data. For $k^{\pm}$-pairs, which were less numerous, the background was about 20 to 25%.

TABLE 4.1

The Background and Accepted Counts for Nominal Beam Momentum 1.75 GeV/c

	π-pair Events		k-pair Events	
$\Theta_{C.M.}$ or $(\pi - \Theta_{C.M.})$	Background	Final Accepted Counts	Background	Final Accepted Counts
45^o - 50^o	3.8 ± 1.3	28.2 ± 5.8	.3 ± .36	1 ± 1.8
50^o - 55^o	1.8 ± .9	103.2 ± 10.3	5.6 ± 1.6	25.4 ± 5.8
55^o - 60^o	6.6 ± 1.8	130.4 ± 11.8	4.9 ± 1.5	25.1 ± 5.7
60^o - 65^o	7.7 ± 2.0	81.3 ± 9.6	6.7 ± 1.8	30.3 ± 6.3
65^o - 70^o	9.4 ± 2.2	80.6 ± 9.7	9.0 ± 2.2	26.0 ± 6.3
70^o - 75^o	13.1 ± 2.7	100.9 ± 11.0	11.7 ± 2.5	51.3 ± 8.3
75^o - 80^o	13.3 ± 2.8	153.7 ± 13.2	13.8 ± 2.8	45.2 ± 8.2
80^o - 85^o	12.2 ± 2.7	218.8 ± 15.4	9.7 ± 2.3	54.3 ± 8.3
85^o - 90^o	13.3 ± 2.8	275.7 ± 17.2	11.9 ± 2.6	75.1 ± 9.7

F. Available Target Length

Because of the layout of the apparatus, the efficiency for registering events was not constant for different configurations. It was highest for symmetric ones ($\theta_L = \theta_R$), and tapered off for asymmetric events. This effect could be best visualized by considering which part of the target was available for a given value of $\Theta_{C.M.}$. Fig. 4.23 shows the effective target length AB, for each of two event configurations, as defined by the apparatus.

For a given $\Theta_{C.M.}$, the positions of points A and B depended slightly on ϕ, and the "average target length", $L(\Theta_{C.M.})$, was defined as $L(\Theta_{C.M.}) = \int d\phi \ell(\Theta_{C.M.}, \phi)/\int d\phi$, where $\ell(\Theta_{C.M.}, \phi)$ represented the length "AB".

Because of the kinematic matrix in the CC1, there was a lab-θ cutoff, defined by the range:

$$23 \leq \theta \text{ channel sum} \leq 38 \ .$$

Values of 23 and 38 for the θ channel sum corresponded to angles of about 106^o and 26^o respectively in the laboratory. The effect of this cutoff was calculated as illustrated in 4.24. For the angle as shown, the CC1 θ channel sum could be either 38 (shaded) or 39 (unshaded) depending on where the vertex was along the target. Specifically, the probability for a track with this polar angle being registered as 38 was a/(a+b) and that as 39 was b/(a+b). Consequently, the true effective target length at this forward angle was:

$$\ell'(\theta, \phi) = \ell(\theta, \phi) \frac{a}{a+b}$$

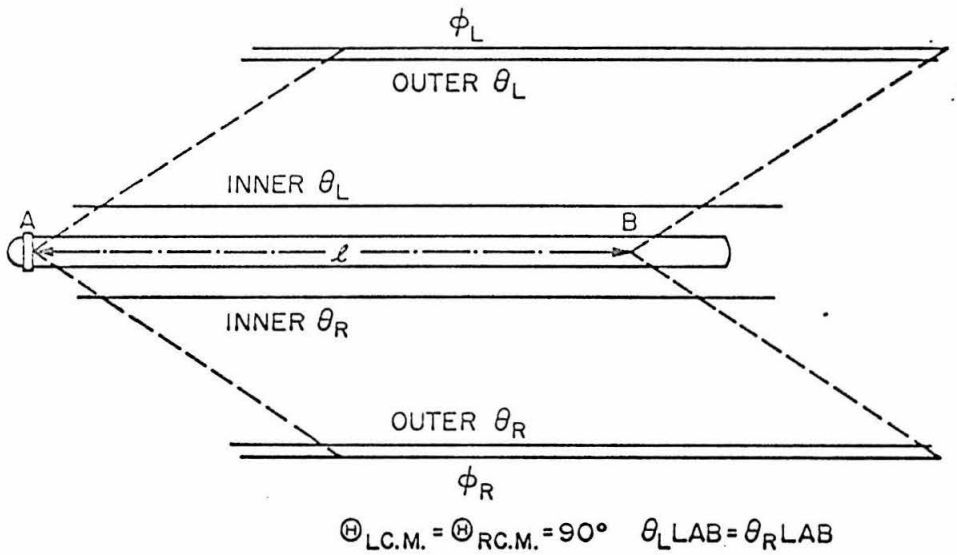

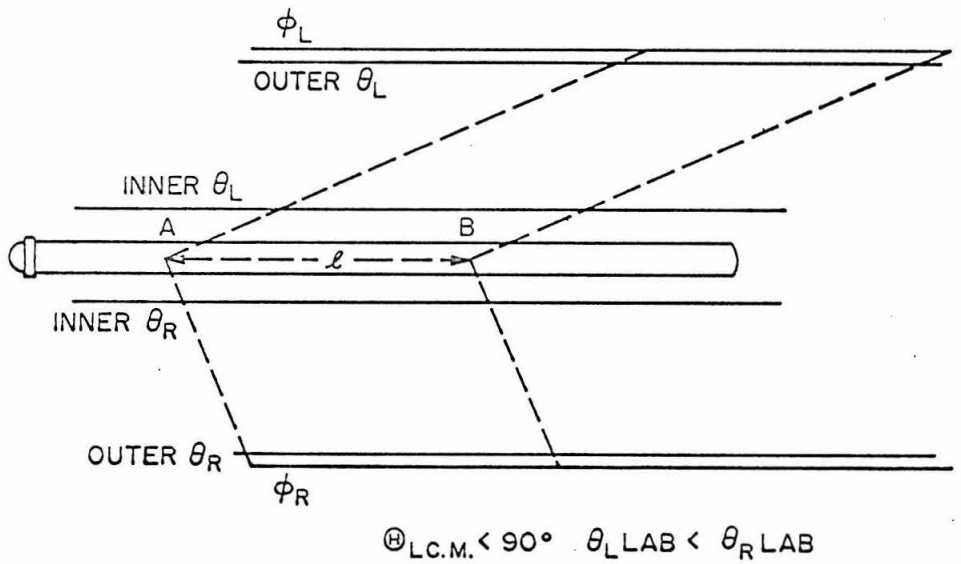

Fig. 4.23 Effect of the value of $\Theta_{LC.M.}$ on the available target length "AB"

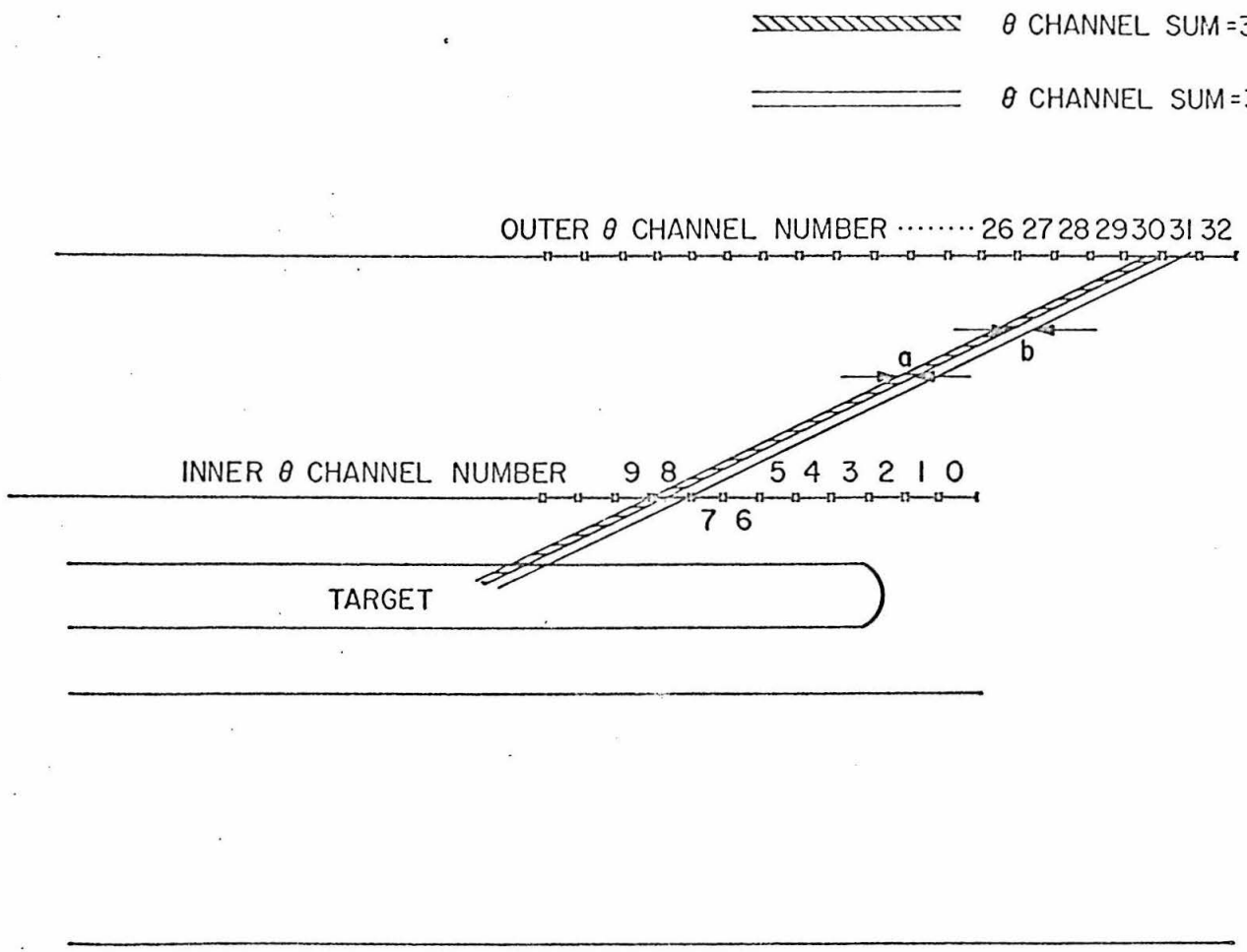

Fig. 4.24 Effect of the CC1 matrix θ-channel-sum cutoff on effective target length

where a+b was just the width of one theta hodoscope channel. The backward angle cutoff was calculated in a similar fashion.

Fig. 4.25 shows $L(\Theta_{C.M.})$ for $\bar{p} + p \rightarrow \pi^+ + \pi^-$ with and without the cutoff for 1.75 GeV/c antiprotons. By plotting Z-histograms of events with definite $\Theta_{C.M.}$, the calculated values of $L(\Theta_{C.M.})$ were checked at a few angles, as shown in Fig. 4.25. However, the lack of a sufficiently large number of events prohibited accurate experimental determination of $L(\Theta_{C.M.})$.

In the calculation of available target length, the beam was taken to be a geometric line along the axis of the target. In reality, the beam was of finite cross section. Also, the hodoscope positions were uncertain to about 1/4". The error in the effective target length due to these effects was studied and found to be less than 1%.

For beam momenta 0.75 GeV/c and 0.875 GeV/c, the CC1 matrix was not used because of the low intensity $\bar{p}$ beam. No cutoff correction was necessary in the calculation of angular distributions at these momenta.

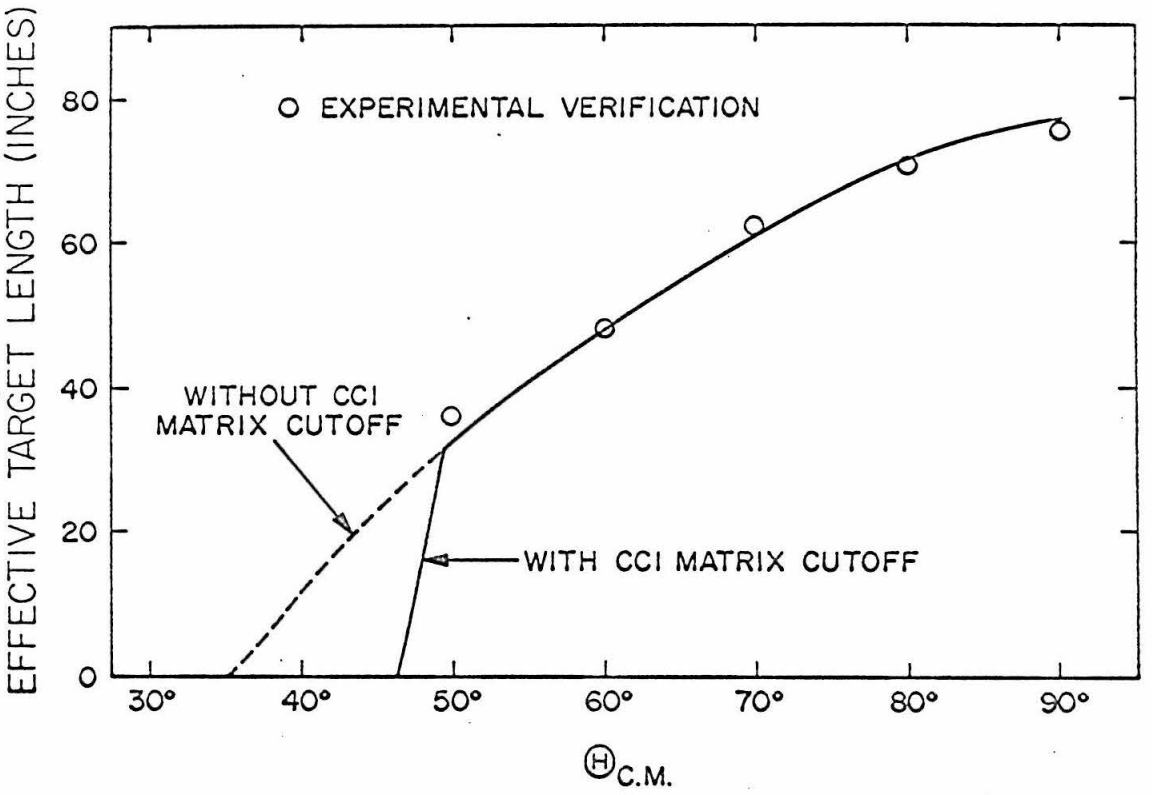

Fig. 4.25 Average effective target length $L(\Theta_{C.M.})$ as a function of $\Theta_{C.M.}$ with and without the CC1 matrix θ-channel-sum cutoff for $\bar{p} + p \rightarrow \pi^+ + \pi^-$. $\bar{p}$ momentum = 1.75 GeV/c

G. Beam Attenuation

Antiprotons in the beam were removed as they passed through the target due to their interactions with the protons. Therefore, to obtain accurate cross sections, the beam attenuation had to be considered.

If the beam electronics counted N_o antiprotons entering the target, then at a position Z inside the target, the number of antiprotons left, N, was given by

$$N = N_o e^{-(Z + 40)/\lambda}$$

where Z was measured in inches from the center of the 80" long target, and λ is the interaction length in inches of antiprotons in liquid hydrogen. Thus, from A to B in Fig. 4.23 (coordinates Z(A), Z(B) respectively),

No of antiprotons x thickness of liquid hydrogen passed through =

$$\int_{Z(A)}^{Z(B)} N_o e^{-(Z+40)/\lambda} dZ = \lambda N_o (e^{-(Z(A)+40)/\lambda} - e^{-(Z(B)+40)/\lambda})$$

Without attenuation, this number would have been $N_o(Z(B) - Z(A))$. Therefore, an attenuation factor $A(\Theta_{C.M.}, \phi)$ could be defined:

$$A(\Theta_{C.M.}, \phi) = \lambda(e^{-(Z(A)+40)/\lambda} - e^{-(Z(B)+40)/\lambda})/(Z(B)-Z(A)) \qquad 4.6$$

Taking .069 gm/cm^2 as the density of liquid hydrogen, λ was related to the antiproton-proton total cross section σ in millibarns by

$$\lambda = \frac{10^4}{1.049\,\sigma} \quad \text{inches}$$

By fitting a smooth curve through σ as measured by Kycia et al.,[1] λ was approximated by

$$\lambda(q) = 45.5 + 38.9\,q - 4.2\,q^2 \quad \text{inches}, \qquad 4.7$$

where q is the antiproton momentum in GeV/c. This fit was found to be good to $\pm$ 1.3% in the range $1 \leq q \leq 2.75$ GeV/c. This inaccuracy is of the same order of magnitude as the uncertainties in the total cross section data ($\simeq$ 1%).

In the acceptance of an event, limits were set to separate $\pi^{\pm}$-pair and $k^{\pm}$-pair final states from background of multiparticle final states. These limits were generous enough to allow some small angle elastic scattering of the antiprotons before annihilation. Therefore, the beam attenuation as calculated from the total cross section was too large. However, taking 1.61 GeV/c as an example, the maximum allowed scattering was about 2^o in the lab.system or about 5^o in the center-of-mass system. The differential elastic scattering cross section of antiprotons at 1.61 GeV/c is $\left.\frac{d\sigma}{d\Omega}\right|_{e\ell}(0) \simeq 50$ mb/sr.[7] Thus, the cross section for scattering at $\leq 5^o$ was about 1.2 mb, which is about 1.2% of the total cross section. This inaccuracy is again of the same order of magnitude as the uncertainties in the total cross section data.

The values of the attenuation factor, $A(\Theta_{C.M.}, \phi)$ varied from about 2 for 0.75 GeV/c beam momentum to about 1.3 for 2.75 GeV/c beam momentum. The uncertainty in percents in its determination was estimated to be ± 1.5%.

H. Calculation of Cross Sections

For most of the beam momenta, the antiproton beam intensity was high enough that the spark chamber trigger rate was greater than one per beam pulse, while the spark-chamber-camera system was able to take only one picture per pulse. Of the pictures taken, some were impossible to measure for various reasons. However, it was assumed that the analysis of a picture did not depend on the angles of any annihilation event in that picture. The pictures analyzed were taken to be an unbiased sample of data.

In a run, if the antiproton count (TOF $\bar{p}$) was N, the trigger count was n, and M pictures were taken and analyzed, the effective number of antiprotons that yielded the result of the analysis was then NM/n. At beam momenta for which more than one run were taken, the total effective number of antiprotons, B, was given by

$$B = \sum_{\substack{\text{runs with this} \\ \text{beam momentum}}} (NM/n)_i .$$

After the $\Theta_{LC.M.} - m^2$ matrices were folded across $\Theta_{LC.M.} = 90^o$, the yield, ΔY, for this experiment, at ϕ and center-of-mass angle $\Theta_{C.M.}$, within the solid angle $\Delta\Omega(=\sin\Theta_{C.M.}\,\Delta\Theta_{C.M.}\,\Delta\phi)$ was

$$\Delta Y = \left[\frac{d\sigma}{d\Omega}(\Theta_{C.M.}) + \frac{d\sigma}{d\Omega}(\pi - \Theta_{C.M.})\right] \ell'(\Theta_{C.M.}, \phi) A(\Theta_{C.M.}, \phi) \rho_p B \Delta\Omega,$$

where $\ell'(\Theta_{C.M.}, \phi)$ = effective target length,

$A(\Theta_{C.M.}, \phi)$ = attenuation factor, and

ρ_p = proton density in target.

In the presentation of the results of this experiment, the events were put in 5^o center-of-mass angle bins. For a bin labeled by $\Theta_{C.M.}$, the value of $[\frac{d\sigma}{d\Omega}(\Theta_{C.M.}) + \frac{d\sigma}{d\Omega}(\pi - \Theta_{C.M.})]$ was therefore given by

$$\frac{d\sigma}{d\Omega}(\Theta_{C.M.}) + \frac{d\sigma}{d\Omega}(\pi - \Theta_{C.M.})$$

$$= \text{Counts in bin } (\Theta_{C.M.}) \Big/ \left[B\rho_p \int d\phi \int_{\Theta=\Theta_{C.M.}-2.5}^{\Theta=\Theta_{C.M.}+2.5} d\Theta \sin\Theta \ell'(\Theta,\phi) A(\Theta,\phi) \right].$$

The effective target length without CC1 cutoff, ℓ, was used in place of ℓ' for the two lowest beam momenta 0.75 GeV/c and 0.875 GeV/c. The result calculated above did not include systematic corrections, which are discussed in the next chapter.

In the course of the experiment, the detailed trigger conditions sometimes varied. To make sure that the variation did not affect the final cross sections, and to see the overall internal consistency of the data, the number of antiprotons per $\pi^{\pm}$-pair or $k^{\pm}$-pair event was found for each run. These data are plotted in Fig. 4.26, which shows all the runs except nine which were taken before

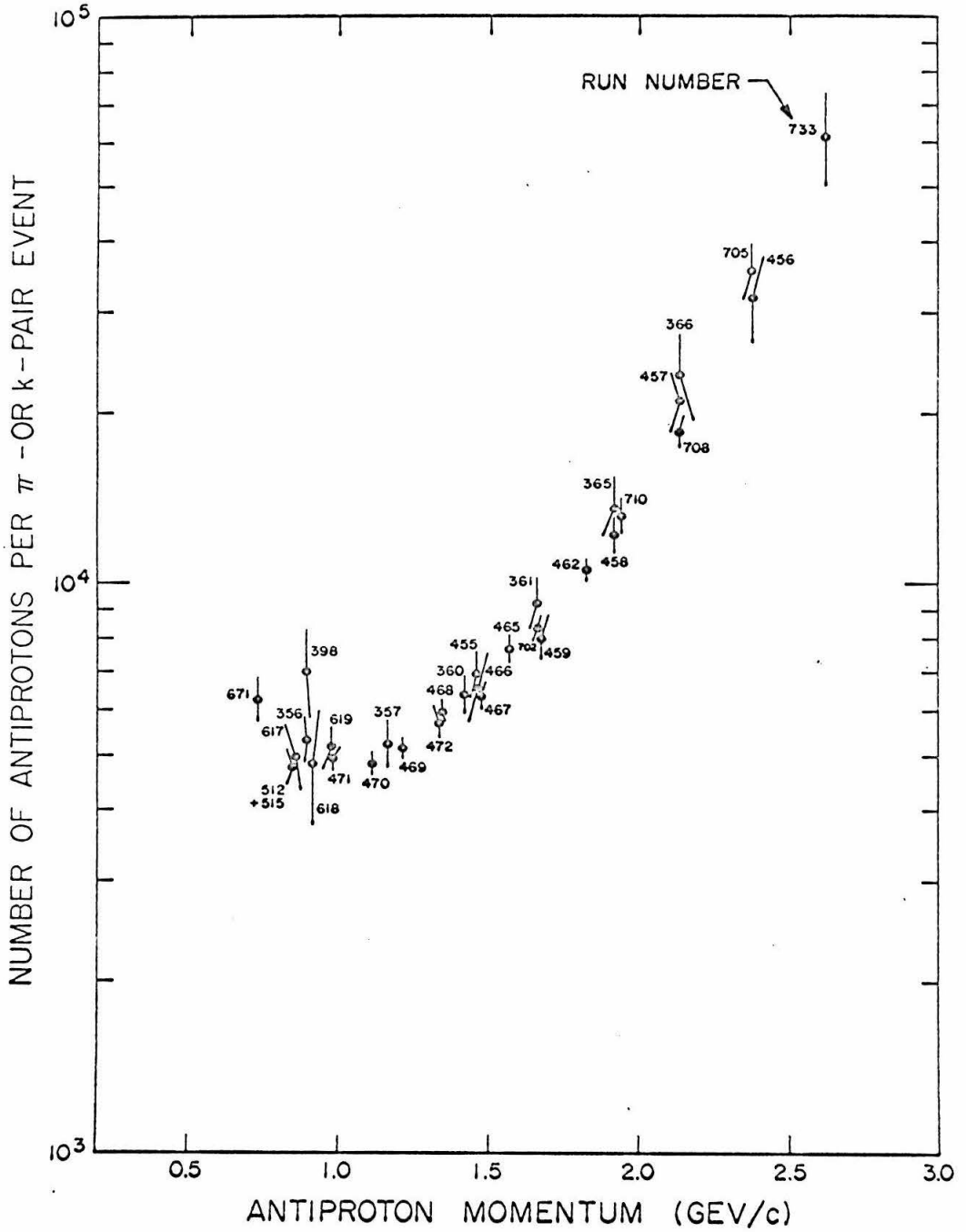

Fig. 4.26 Number of antiprotons per $\pi^{\pm}$-pair or $k^{\pm}$-pair event

an error in the counting of beam antiprotons was discovered. For these nine runs, the results were normalized to those of the runs taken after the error was corrected.

V. SYSTEMATIC CORRECTIONS

A. Introduction

In this chapter, the systematic corrections for this experiment are considered. The following effects were found to affect the cross sections substantially. A rough indication of the size of the correction is given here, in parentheses, for each effect.

1. Radiative correction (6%),
2. Hodoscope inefficiency (8%),
3. Loss of events due to the "ϕ" condition of the trigger requirements (1%),
4. Loss due to the decay of the particles in the final state ($<<$ 1% for $\pi^{\pm}$-pairs, and about 10% for $k^{\pm}$-pairs),
5. Loss due to interaction of the final particles with the equipment (7%),
6. Multiples veto inefficiency (3%).

The loss of events due to measurement errors was 1.5%, as discussed in Chapter 3.

The attenuation of the antiproton beam in the target could be regarded as a systematic error, but it has already been taken into consideration, as described in the last chapter.

The total uncertainty in the absolute normalization was estimated to be $\pm 6.5\%$ for both $\pi^{\pm}$-pair and $k^{\pm}$-pair annihilations. The uncertainty in the normalization at one beam momentum relative to that at another momentum was estimated to be 1% per GeV/c. The

uncertainty in the normalization for a given beam momentum at one center-of-mass angle relative to that at another angle was estimated to be 0.08% per degree. Both of the last two uncertainties were negligible compared to the statistical errors of this experiment.

A sample summary of all the systematic corrections for the 1.75 GeV/c data is given in Table 5.4 at the end of this chapter.

B. Radiative Correction

In any interaction in which there is acceleration or deceleration of charges, photons are emitted. This is simply the Bremsstrahlung phenomenon. Thus, in the reaction $\bar{p} + p \rightarrow \text{meson}^+ + \text{meson}^-$, some photons are always present in the final state:

$$\bar{p} + p \rightarrow \text{meson}^+ + \text{meson}^- + n\gamma \ .$$

This can be represented by diagrams as shown in Fig. 5.1. With every extra photon, the contribution of the diagram to the cross section goes down by a factor of $\alpha = 1/137$. Therefore, to a good approximation, the diagrams with more than one photon can be neglected.

In the center-of-mass system, the presence of the photon changes the interaction from the idealization Fig. 5.2a to Fig. 5.2b. Consequently, in the laboratory system, the directions of the final charged particles depart from those dictated by ideal two-body kinematics.

In this experiment, the $\pi^{\pm}$-pair and $k^{\pm}$-pair events were identified by coplanarity and the value of m^2 which was calculated from the polar angles of the final charged particles. A $\pi^{\pm}$-pair or $k^{\pm}$-pair event was therefore rejected if the presence of the photon caused the directions of the final charged particles to deviate beyond certain limits.

A correction for this type of phenomenon is usually called a "radiative correction." A calculation was done for this experiment using the method described by Y. S. Tsai in Ref. 8. The correction $\delta'(\theta)$ is defined by the following relationship:

$\bar{p} + p \rightarrow \text{MESON}^+ + \text{MESON}^- =$

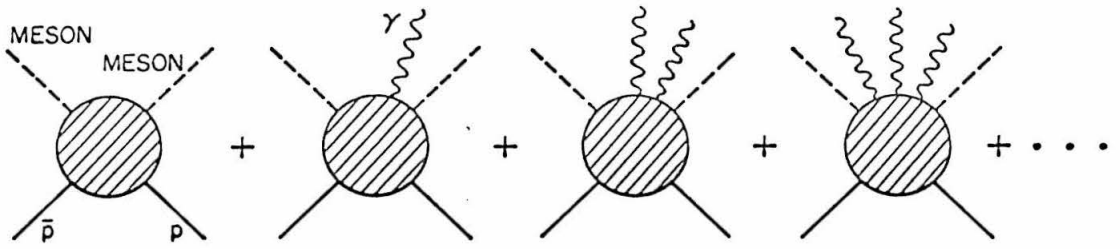

Fig. 5.1 Diagrams for $\bar{p} + p \rightarrow \text{meson}^+ + \text{meson}^-$ with emission of photons

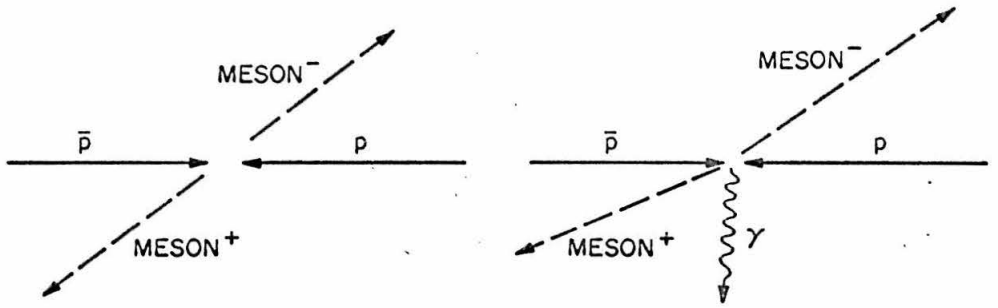

Fig. 5.2 Annihilation of antiproton and proton into a pair of charged mesons in the center-of-mass system with
(a) no emission of photon
(b) emission of one photon

$$\left[\frac{d\sigma}{d\Omega}(\Theta) + \frac{d\sigma}{d\Omega}(\pi - \Theta)\right]_{\text{OBSERVED}} = \left[\frac{d\sigma}{d\Omega}(\Theta) + \frac{d\sigma}{d\Omega}(\pi - \Theta)\right]_{\text{TOTAL}} (1 + \delta'(\Theta)).$$

The results for three antiproton beam momenta are shown in Figs. 5.3a and 5.3b. For other momenta, the correction can be obtained by interpolation or extrapolation. An account of the calculation is given in Appendix 4.

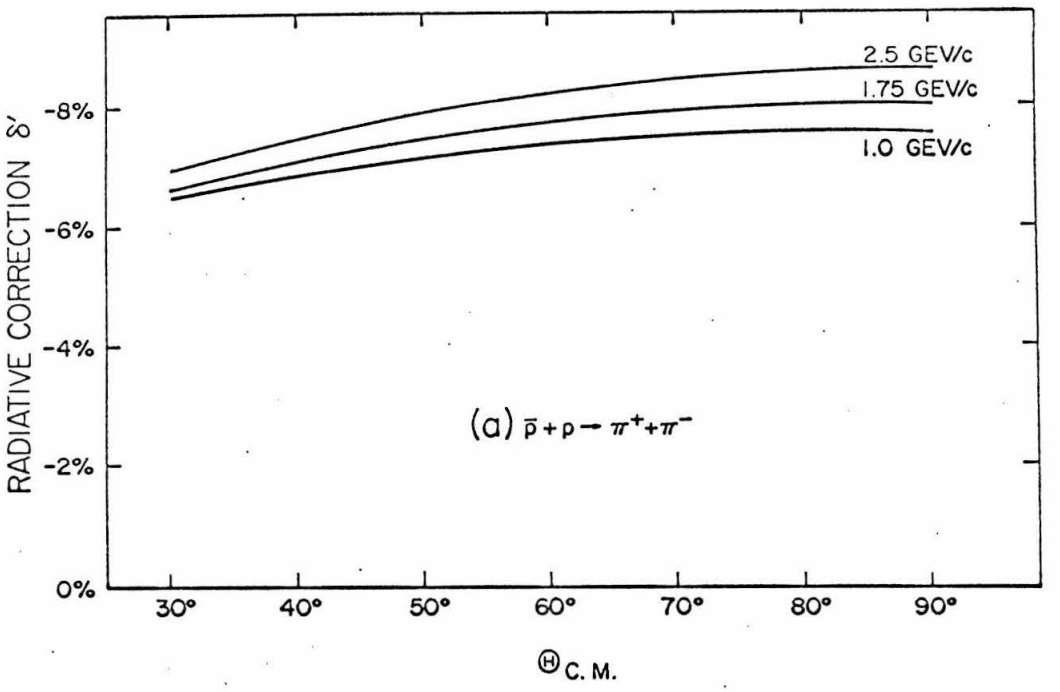

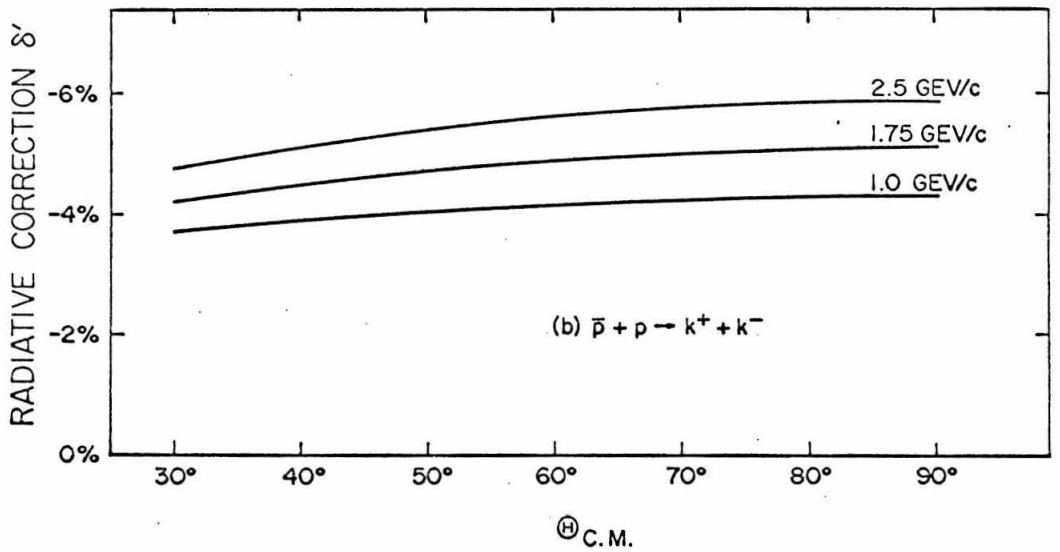

Fig. 5.3 Values of radiative correction δ' in percents for three antiproton beam momenta

(a) $\bar{p} + p \rightarrow \pi^+ + \pi^-$ (accurate to ± 50% of the values)

(b) $\bar{p} + p \rightarrow k^+ + k^-$

C. Hodoscope Inefficiency

The hodoscope inefficiency was determined by utilizing the fact that the counters in a hodoscope tray were overlapped. In a tray, if only one counter detected the passage of a charged particle, the hodoscope channel number was even, and, if both of two adjacent counters were fired, the channel number was odd.

During the experiment, for every event, the numbers of the counters that were fired were punched out on a card by an on-line IBM card punch (BS1 card). From this card, the channel number for each hodoscope tray could be calculated for each event.

The positions of the hodoscopes were carefully surveyed. Thus, after each event was measured in the spark chambers and geometrically reconstructed, the points at which the tracks intersected the hodoscopes could be calculated. For each theta (and phi) hodoscope, the z (or y) co-ordinate of the point of intersection was plotted against the channel number for that tray. This was done for 4369 events which were identified as either $\pi^{\pm}$-pairs or $k^{\pm}$-pairs. The points were grouped into bins of 0.25" (0.22" in the case of the phi hodoscopes) and the counts were written out as in Fig. 5.4. Here, a section of the theta-outer-left (THOL) hodoscope is shown.

The distance from the center of the spark chamber to the THOL tray was about 10". Since the angular measurement inaccuracy was about $\pm 0.5^{o}$, taking 45^{o} as the average lab.polar angle of a track, the inaccuracy of determining the z co-ordinate at the THOL tray was about ± 0.17". This was the main reason for the overlapping as indicated by the shaded areas.

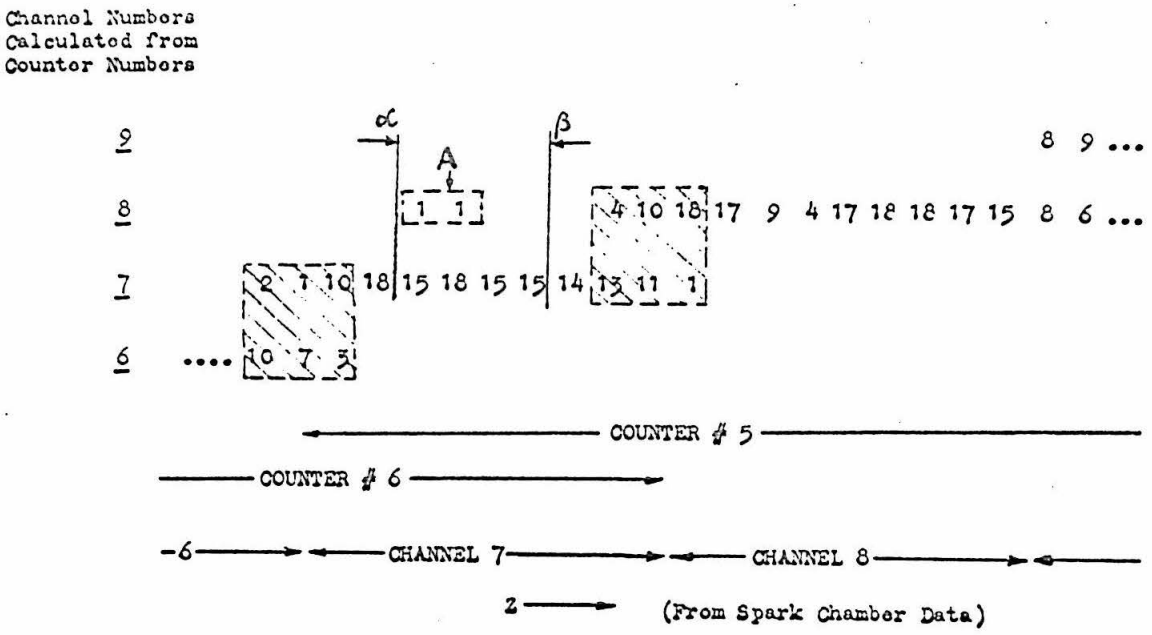

Fig. 5.4 THOL hodoscope channel number counts vs. z co-ordinate of points of impact on THOL hodoscope

For the two counts in the area marked "A," it was recorded that only one counter (#5) detected a charged particle, and hence the THOL channel number was 8. However, according to geometric reconstruction, the track passed through channel 7, where counters #5 and #6 overlapped. Measurement error was not acceptable as an explanation for this discrepancy, and therefore they are interpreted as the result of inefficiency of counter #6.

A 1" wide strip at the center of each channel, from α to β in Fig. 5.4, was used as a region where inefficiency could be unambiguously checked. In such a region, counter #6 failed to detect the passage of charge particles twice out of 15 + 18 + 15 + 15 + 2 = 65 times. In this manner, by counting these "off" counts in the trays, the overall counter inefficiency was determined.

The following table gives the average counter inefficiency in each tray, with statistical errors,

THIL (inner theta left)	1.15 ± 0.32%
THOL (outer theta left)	3.26 ± 0.65%
PHIL (phi left)	2.24 ± 0.46%
THIR (inner theta right)	0.87 ± 0.27%
THOR (outer theta right)	4.23 ± 0.68%
PHIR (phi right)	2.13 ± 0.43%

Approximately half of the area of the hodoscope trays was covered by single counters while the other half involved overlapping

counters. The net effect of the counter inefficiency was as follows: Half the time, the failure of a counter to detect the passage of a charged particle caused that event to be missed, since the trigger requirement "Necessary" required the firing of at least one counter in each tray. However, the other 50% of the time, the failure only caused the corresponding hodoscope channel number of the event to be displaced by one. (For instance, in the case of the counts in area "A" of Fig. 5.4, the THOL channel numbers were recorded as 8 instead of 7.)

Fig. 5.5 shows the distribution of the theta-left-channel-sum vs. theta-right-channel-sum matrix of 1507 events which were identified as either $\pi^{\pm}$-pair or $k^{\pm}$-pair annihilations (nominal beam momentum = 1.75 GeV/c). The boundary marks the "K" trigger requirement. The total count in the matrix elements at the boundary is 102. From the measured counter inefficiencies, the chance that an event was displaced into a neighboring matrix element was found to be $4.75 \pm 1.03\%$. For the events in the boundary matrix elements, assume that half of the displacements caused loss of events. The estimated loss is then only 2.5 ± 0.5 out of 1507 events. Therefore, at this momentum, loss due to displacement in the theta trays was negligible, and the theta tray inefficiency was just half of the overall counter inefficiency. Similar results were obtained at all other momenta.

Fig. 5.6 is a phi-channel-sum histogram of the same 1507 events. By an argument similar to above, channel sum displacement due to counter inefficiency was found to cause a loss of about 1%.

The net hodoscope inefficiency is then as summarized in the following table:

0	0	0	0	0	0	0	0	0	0	0	0	0	0	0	0	0	0	0	0	0
0	0	0	0	0	0	0	0	0	0	0	0	0	0	0	0	0	0	0	0	0
0	0	0	0	0	0	0	0	0	0	0	0	0	0	0	0	0	0	0	0	0
0	0	0	0	0	0	0	0	0	0	0	0	0	0	1	7	14	15	0	0	0
0	0	0	0	0	0	0	0	0	0	0	0	0	2	16	34	24	14	0	0	0
0	0	0	0	0	0	0	0	0	0	0	0	10	25	28	11	4	1	0	0	0
0	0	0	0	0	0	0	0	0	0	10	25	40	22	9	1	0	0	0	0	0
0	0	0	0	0	0	0	0	1	26	73	61	14	7	3	1	0	0	0	0	0
0	0	0	0	0	0	0	3	34	116	67	15	1	0	0	0	0	0	0	0	0
0	0	0	0	0	0	1	29	113	93	17	0	0	0	0	0	0	0	0	0	0
0	0	0	0	0	0	9	70	71	17	1	0	0	0	0	0	0	0	0	0	0
0	0	0	0	0	1	32	56	11	0	0	0	0	0	0	0	0	0	0	0	0
0	0	0	0	0	10	35	17	2	0	0	0	0	0	0	0	0	0	0	0	0
0	0	0	0	2	27	23	2	0	0	0	0	0	0	0	0	0	0	0	0	0
0	0	0	3	14	18	10	0	0	0	0	0	0	0	0	0	0	0	0	0	0
0	0	0	3	28	11	2	0	0	0	0	0	0	0	0	0	0	0	0	0	0
0	0	1	9	9	2	0	0	0	0	0	0	0	0	0	0	0	0	0	0	0
0	0	3	12	6	2	0	0	0	0	0	0	0	0	0	0	0	0	0	0	0
0	0	0	0	0	0	0	0	0	0	0	0	0	0	0	0	0	0	0	0	0
0	0	0	0	0	0	0	0	0	0	0	0	0	0	0	0	0	0	0	0	0
0	0	0	0	0	0	0	0	0	0	0	0	0	0	0	0	0	0	0	0	0

Fig. 5.5 "THETA LEFT channel sum" vs. "THETA RIGHT channel sum" matrix for 1507 nominally 1.75 GeV/c events which were identified as either $\pi^{\pm}$-pair or $k^{\pm}$-pair annihilations

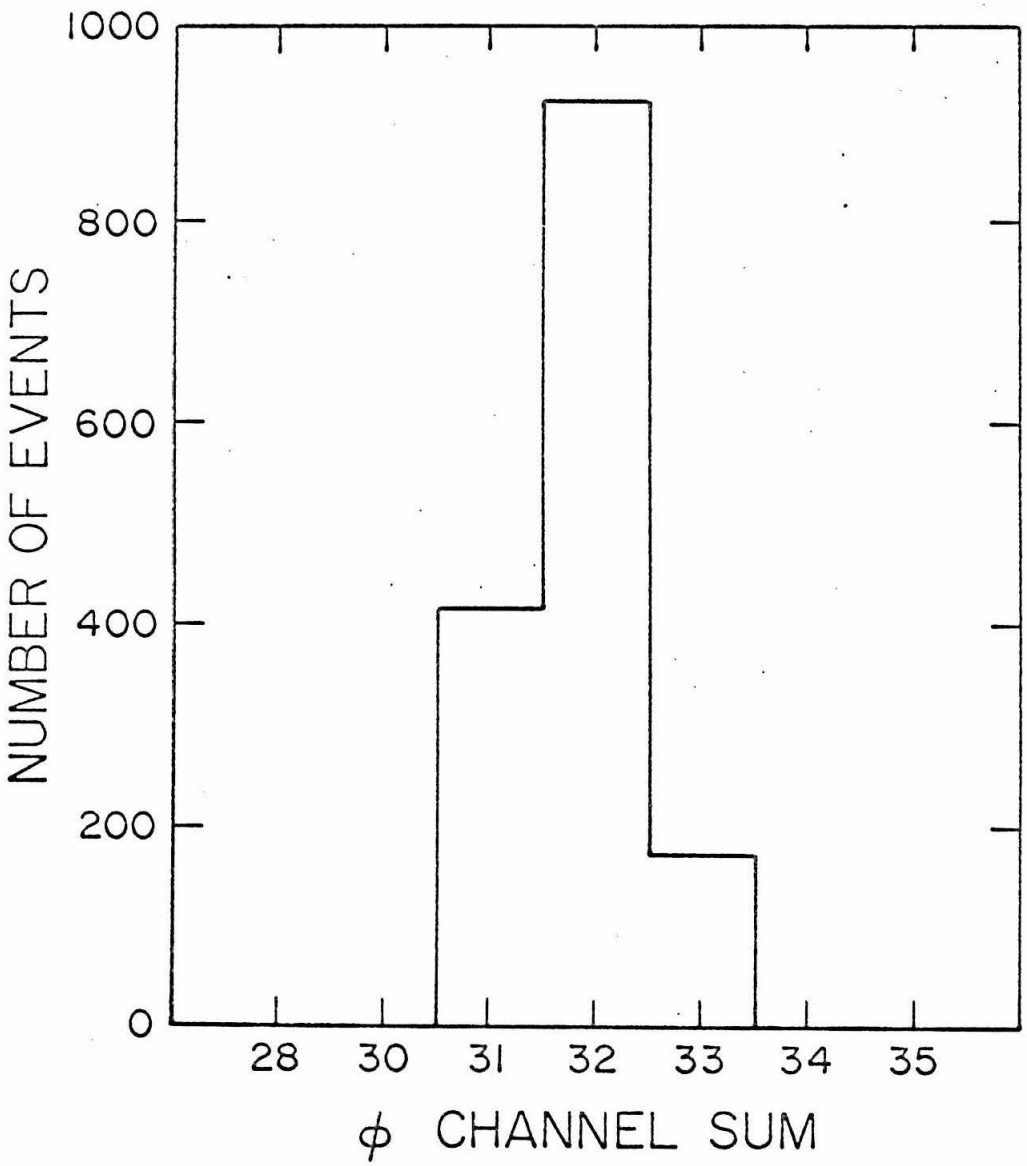

Fig. 5.6 "PHI channel sum" histogram for 1507 nominally 1.75 GeV/c events which were identified as either $\pi^{\pm}$-pair or $k^{\pm}$-pair annihilations

TABLE 5.1 Hodoscope Inefficiency

THIL (theta inner left)	0.58 ± 0.16%
THOL (theta outer left)	1.63 ± 0.33%
PHIL (phi left)	1.62 ± 0.23%
THIR (theta inner right)	0.43 ± 0.13%
THOR (theta outer right)	2.12 ± 0.34%
PHIR (phi right)	1.56 ± 0.21%

From the sum of these inefficiencies, the overall detection inefficiency was 7.8 ± 0.6%.

D. Loss Due to the Condition "ϕ" in the Trigger Requirements

Fig. 5.7 is a ϕ-channel-sum histogram of all the events in one run (at 1.5 GeV/c) which satisfied only the condition "N" (Necessary). The events in the peak were mainly those with only two charged particles in the final state, the majority of them being $\bar{p}$ - p elastic scattering events. It can be seen that the peak appears to include some cases with ϕ-channel-sums 30 and 34. Assuming that the background had no peak in the region ϕ-sum = 30 to 34, the events with ϕ-sums 30 and 34 contributed about 6% to the total signal above the background (see solid normalized histogram in Fig. 5.8). Since in triggering the spark chambers for $\pi^{\pm}$-pair and $k^{\pm}$-pair events, ϕ-sum was required to be 31, 32 or 33, there was a loss of events due to this "ϕ" requirement.

The spread in the distribution in Fig. 5.8 could be caused by the following reasons:

1) The finite cross section of the beam inside the target (see Figs. 4.18 and 4.19),

2) The deviation from ideal coplanarity of a two-body event due to beam divergence and multiple scattering of the final particles as discussed in the last chapter,

3) The deviation from perfect alignment of the ϕ-hodoscope trays,

4) The interaction of the final particles with the material in the equipment producing charged particles in directions different from the original tracks.

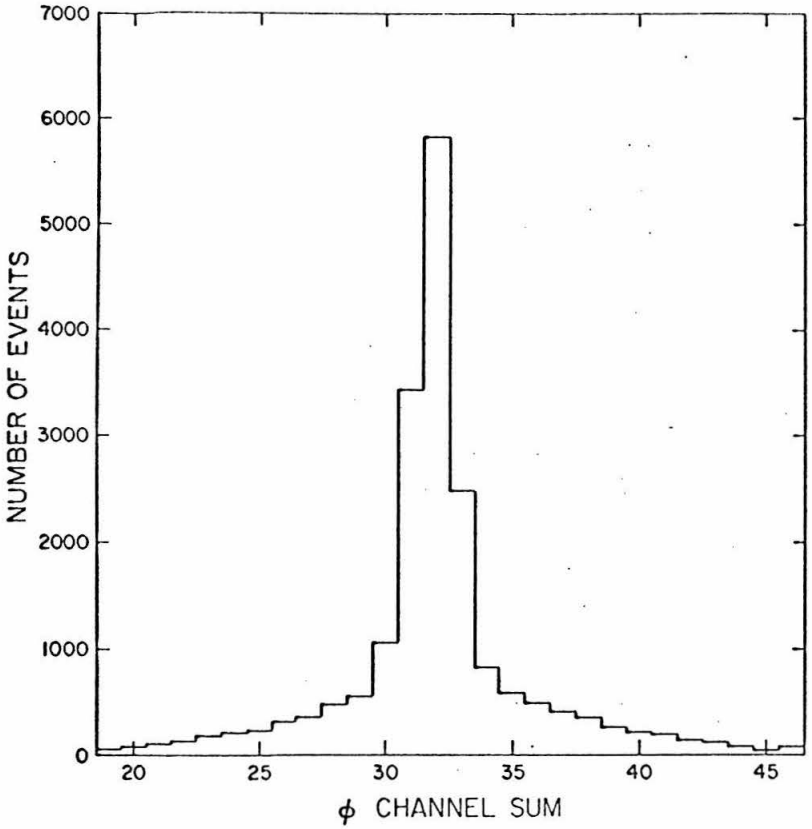

Fig. 5.7 "PHI channel sum" histogram for nominally 1.5 GeV/c events which satisfied condition "N" only

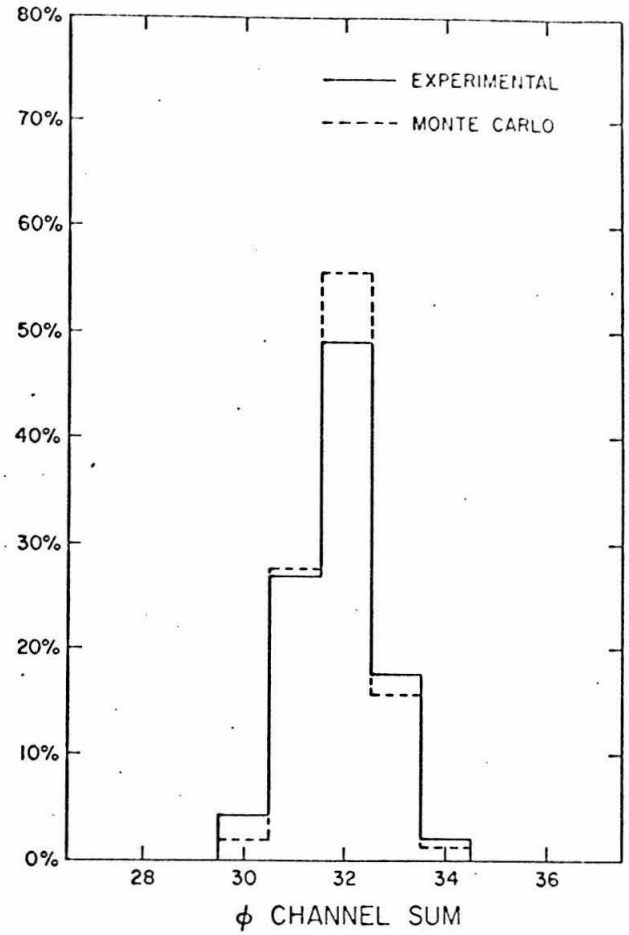

Fig. 5.8 Normalized "PHI channel sum" histograms for nominally 1.5 GeV/c events

The effects of the first three reasons were studied with Monte-Carlo method. The beam profile used was obtained from the measured x-y values of the spark chamber events. It was found that the possible loss at any position in the beam due to the ϕ requirement was less than 10%, and for 80% of the cross section of the beam, the possible loss was less than 5%. Thus, the beam profile obtained from the measurements was not significantly different of that of the actual beam.

The distribution of deviations from perfect coplanarity was also obtained from the spark chamber measurements. The misalignment of the ϕ-trays was found from the plots similar to Fig. 5.4 for the ϕ-hodoscopes (i.e., the BS1-information vs. impact-point plots). Due to a lack of statistics, this could not be done very accurately.

The histogram in dotted lines in Fig. 5.8 is the result (also normalized) of this Monte-Carlo study. 250 pairs of experimental values for vertex position (X, Y) were used, each generating 300 tries. It is seen that the lopsidedness of the distribution was quite accurately reproduced. However, 3.5% of the counts were found in channels 30 and 34 instead of the experimental 6%. The disagreement could be roughly accounted for by the fourth reason stated above. A calculation indicated that the effect of $\bar{p}$ interactions was of about the right order of magnitude. However, the disagreement could also be partly due to ϕ-tray misalignment, which could not be accurately determined.

For $\pi^{\pm}$-pair and $k^{\pm}$-pair events, loss due to interaction with the material in the equipment was considered separately (see Section F of this chapter), its effect on the loss due to the "ϕ" requirement was therefore not included in this consideration.

Figs. 5.9 and 5.10 show the experimental and Monte-Carlo ϕ-channel-sum distribution at nominal beam momenta 0.75 and 0.875 GeV/c respectively. The loss due to the "ϕ" requirement was worst at these two lowest momenta because of the large beam cross section as a result of greater multiple scattering of the antiprotons in the beam.

Table 5.2 gives the loss due to the ϕ-requirement for all the beam momenta in this experiment as determined by the Monte-Carlo method.

Because of multiple scattering, the size of the beam cross section increased along the target. Since the cross section directly affected the loss of events due to the "ϕ" requirement, this phenomenon might have affected the angular distribution as measured in this experiment because different parts of the target favored different directions of the final particles.

The events of nominal beam momentum 0.875 GeV/c were separated into four groups according to their values of Z (position along the target), and their X-Y co-ordinates were used in a Monte-Carlo study. Table 5.3 shows the result. The conclusion was that the loss due to the ϕ-requirement could not have produced significant angular bias.

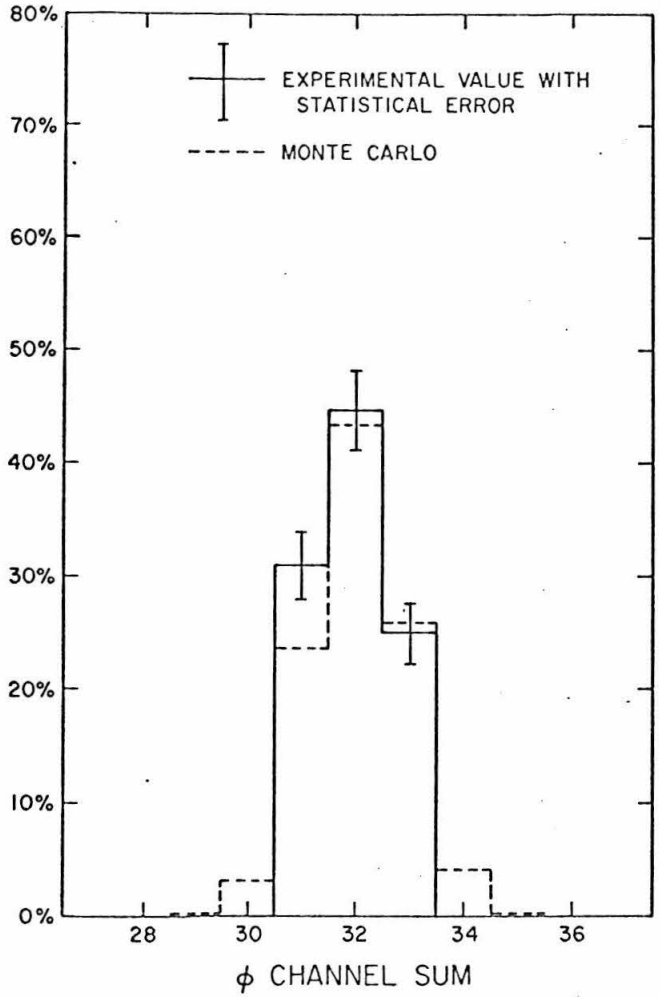

Fig. 5.9 Normalized "PHI channel sum" histograms for nominally 0.75 GeV/c $\pi^{\pm}$-pair or $k^{\pm}$-pair events

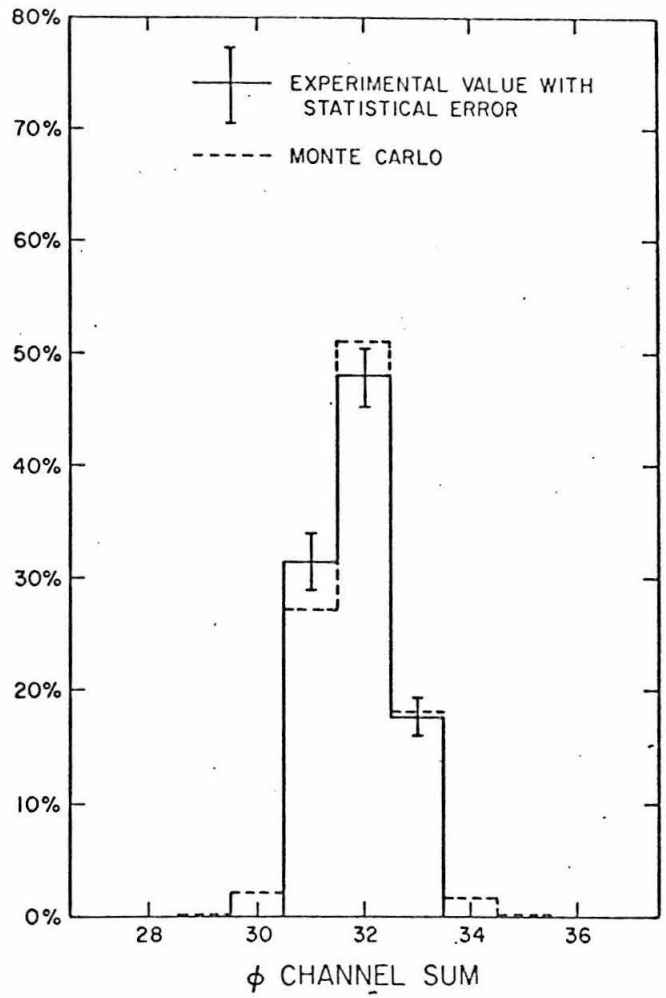

Fig. 5.10 Normalized "PHI channel sum" histograms for nominally 0.875 GeV/c $\pi^{\pm}$-pair or $k^{\pm}$-pair events

TABLE 5.2 Loss Due to "ϕ"-requirement

Nominal beam momentum	loss
0.75 GeV/c	7.2 ± 1.0 %
0.875	3.9 ± 1.0 %
0.94	3.3 ± 1.0 %
1.00	2.3 ± 1.0 %
1.125	2.4 ± 1.0 %
1.25	1.6 ± 1.0 %
1.375	1.4 ± 1.0 %
1.5	1.3 ± 1.0 %
1.625	1.6 ± 1.0 %
1.75	0.8 ± 0.7 %
1.875	1.0 ± 0.7 %
2.0	0.5 ± 0.7 %
2.25	0.4 ± 0.5 %
2.50	0.5 ± 0.5 %
2.75	0.5 ± 0.5 %

TABLE 5.3 Dependence of Loss Due to "ϕ"-requirement on "Z" for 0.875 GeV/c Nominal Antiproton Beam Momentum

Z =	-40" to -17"	-17" to -1."	-1." to 13"	13" to 40"
Loss due to "ϕ"	2.7 ± 1.0%	3.9 ± 1.0%	3.3 ± 1.0%	5.4 ± 1.0%

E. Loss due to Decay

The final particles in this experiment had finite lifetimes:

π^+, π^-	2.55×10^{-8} sec.,
k^+, k^-	1.23×10^{-8} sec.

Before the particles could pass through the spark chambers, they might decay, causing some possible loss of events.

In an event, the particle with the smaller polar angle θ_{lab} had a larger velocity. However, it also had a longer distance to travel before it passed through the spark chamber. A calculation showed that the probability of decaying before leaving the spark chamber was the same for each of the two final particles in a $\pi^{\pm}$-pair or $k^{\pm}$-pair event.

For $\pi^{\pm}$-pairs, the number of events with a decay was $\lesssim 3\%$. Moreover, in this experiment, the $\pi \rightarrow \mu + \nu$ kinematics caused the μ to be within 1.5^{o} of the π-direction in about 90% of the decays. Therefore, the loss of $\pi^{\pm}$-pairs due to decays was negligible.

In the case of k-mesons, the most important decay modes are:

$k^{\pm} \rightarrow \pi^{\pm} + \pi^{o}$	21.3%
$k^{\pm} \rightarrow \mu^{\pm} + \overset{\nu}{\underset{\nu}{}}$	63.2% .

Fig. 5.11 gives the kinematics for the second decay mode. The original k-meson direction is taken to be the reference direction.

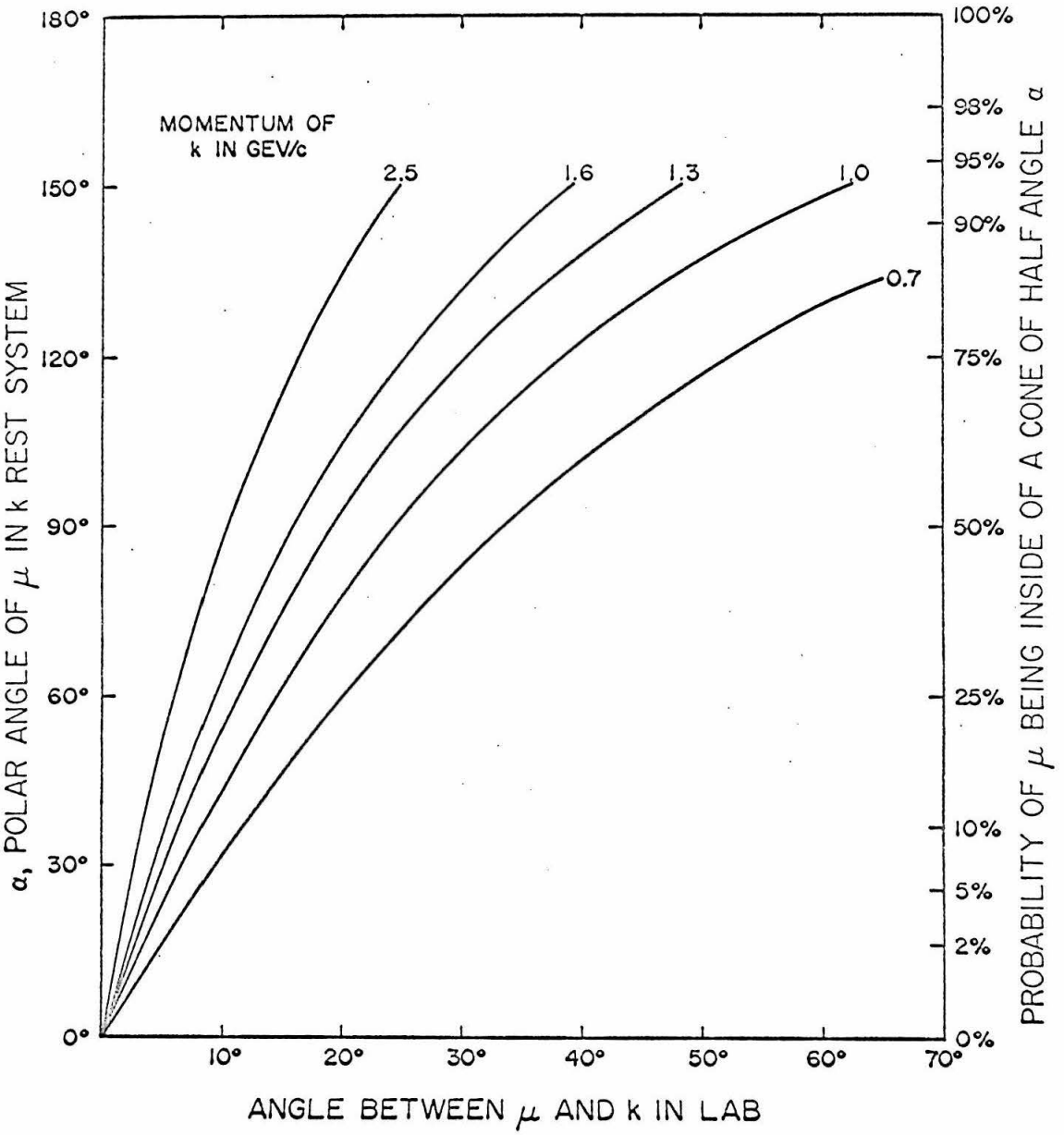

Fig. 5.11 Kinematics for k-meson decay mode $k \rightarrow \mu + \nu$

The vertical co-ordinate on the left is the polar angle of the direction of the μ-meson in the rest system of the original k, and the horizontal co-ordinate is the angle between the direction of the μ and that of the k in the laboratory. The transformation is shown for four different k-meson momenta in the laboratory.

The spin of k is zero, and thus the decay is isotropic in the rest frame of the k. Consequently, the probability of the direction of the final μ being within a cone of half-angle α is $(1 - \cos \alpha)/2$. This quantity is the vertical co-ordinate on the right in Fig. 5.11. The rest-frame-to-lab transformation for the first decay mode is not significantly different.

The range of the momenta which the k-mesons could have in this experiment was about 0.7 GeV/c to 2.5 GeV/c. From Fig. 5.11, it was evident that if a k-meson in the experiment decayed, more than 95% of the time the direction of the charged particle in the decay product changed more than 2^{o} from the original direction of the k-meson. It was therefore assumed that a k-pair event was lost if the decay occurred before both of the k-mesons had gone through two thirds the width of the spark chambers. The loss of k-events due to decay, averaged over the range of the azimuthal angle ϕ, was calculated with this assumption, and the result is shown in Fig. 5.12. This correction was estimated to be accurate to $\pm$ 50%.

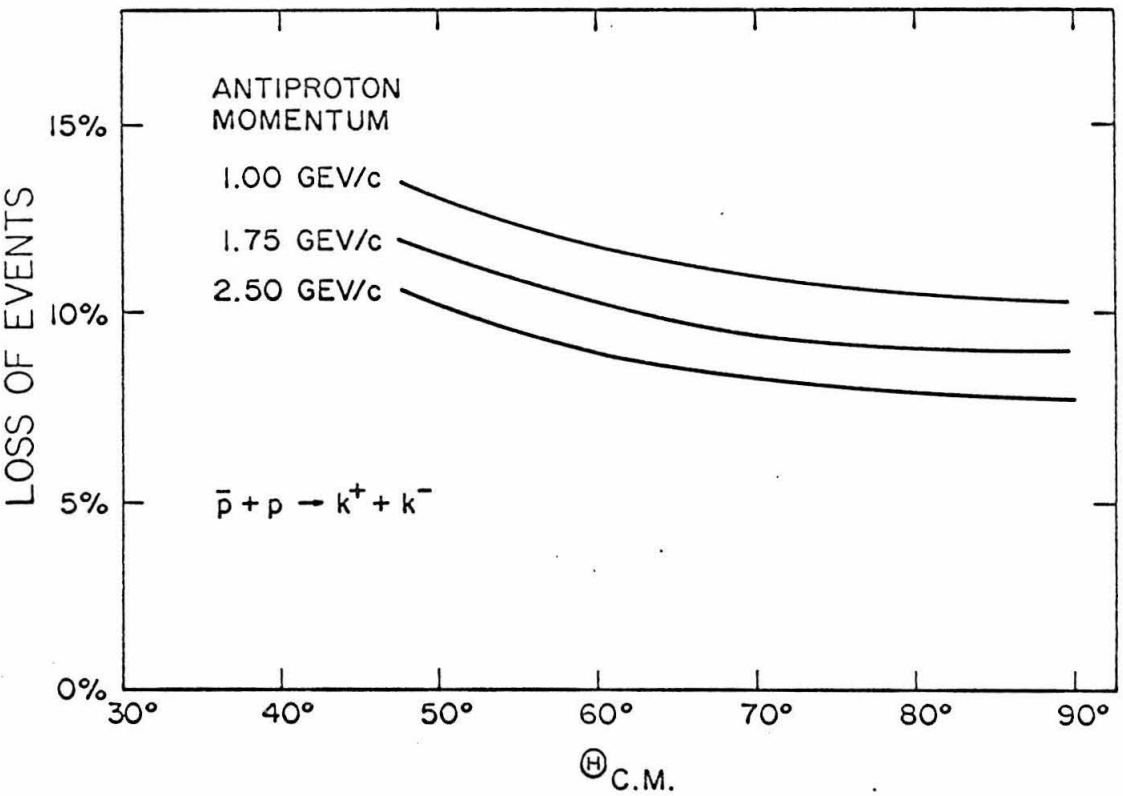

Fig. 5.12 Loss of $\bar{p} + p \rightarrow k^+ + k^-$ events in percents due to the decay of k-mesons (accurate to ± 50% of its value)

F. Loss due to Interaction

Loss of events could also be caused by the interactions of the final state particles in the material of the target, the spark chambers, and the hodoscopes. Below is a list of the material on each side of the beam including the ϕ hodoscopes.

1" of liquid hydrogen,

0.068" of mylar,

10" of air,

0.049" of aluminum,

6.4" of spark chamber gas mixture (10% He and 90% Ne) at atmospheric pressure,

1.125" of scintillator.

The total amount was about 3.95 gm/cm^2 of material. The major contributor was the hodoscopes, each consisting of 1 gm/cm^2 of carbon and 0.14 gm/cm^2 of aluminum.

On each side of the target, the average separation between the outer θ hodoscope and the ϕ tray was about 6". To satisfy the trigger requirement, if the final particle interacted with the material in the outer θ tray, a charged particle was required to strike the ϕ tray on a horizontal strip 6.6" wide (the width of three ϕ-hodoscope channels). In the momentum range of the final state particles in this experiment (0.7 to 2.5 GeV/c), charged particles from nuclear interactions mostly go forward. Therefore, it was assumed that an event was lost only if one of the final particles interacted with the material in the equipment before the outer θ hodoscope. Thus, the

amount of material that caused the loss of events was taken to be 1.73 gm/cm^2 on each side of the beam. By weight, the material was

70% carbon, 17% aluminum, 10.5% hydrogen, and the rest air.

For the entire momentum range of the final particles, the following average values of the π-nucleus total cross sections were used:

π - hydrogen ..... 32 mb, [9]

- carbon ..... 320 mb, [10]

- aluminum ..... 630 mb, [10]

The error resulting from this approximation was estimated to be about 50% in the calculated correction to the loss due to interaction.

Cross sections for k-mesons on carbon and aluminum were not found in the literature. However, since σ_T(k-nucleon) $\tilde{=} \frac{2}{3} \sigma_T$($\pi$-nucleon), [11] it was assumed that

$$\sigma_T(k - C) = \frac{2}{3} \sigma_T(\pi - C) \quad \text{and}$$

$$\sigma_T(k - Al) = \frac{2}{3} \sigma_T(\pi - Al) .$$

The resulting error was estimated not to exceed $\pm 50\%$ of the correction.

With these approximations, the loss due to interaction of the final particles was calculated. It is summarized in Figs. 5.13a and 5.13b for three incident antiproton momenta.

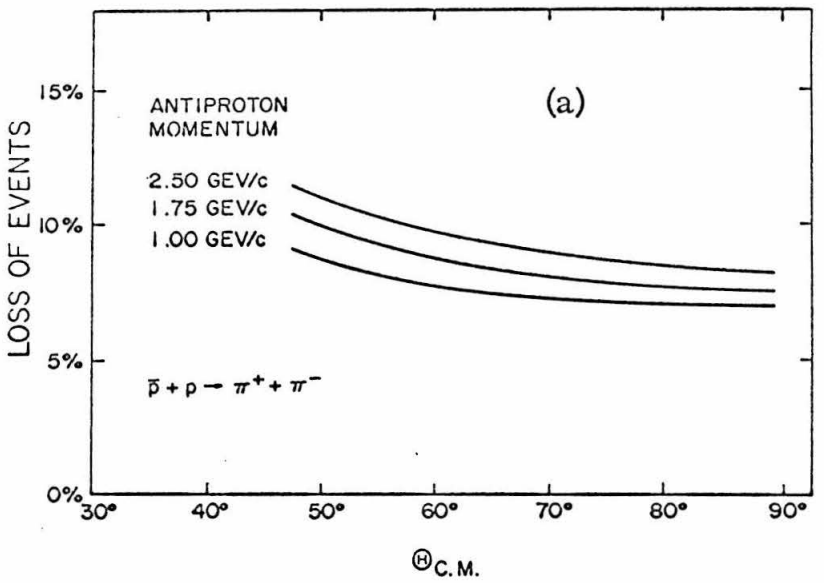

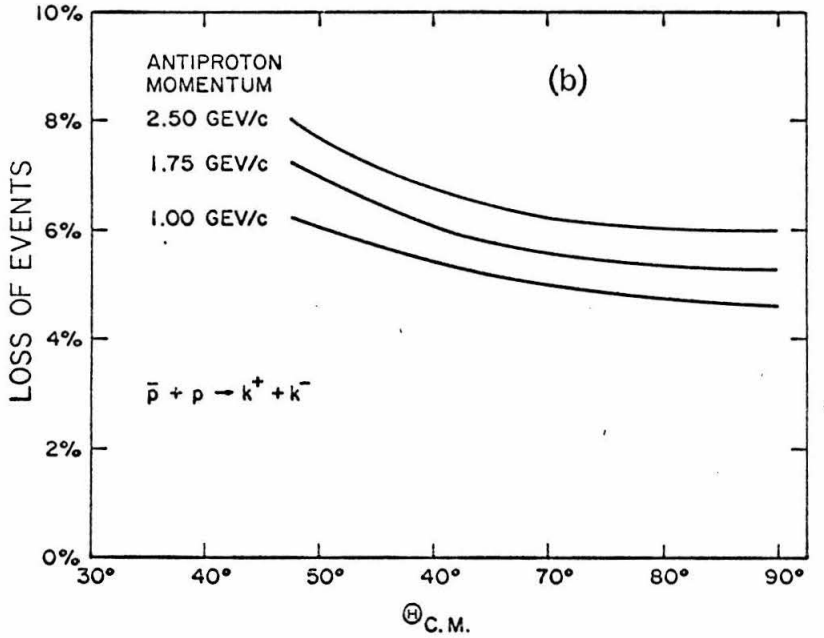

Fig. 5.13 Loss of events in percents due to interaction for
(a) $\bar{p} + p \rightarrow \pi^+ + \pi^-$ (accurate to ± 50% of its value)
(b) $\bar{p} + p \rightarrow k^+ + k^-$

G. Multiples veto Inefficiency

Due to the presence of phototube noise, calibration sources and other forms of background radiation in the laboratory, the hodoscopes could register the passage of charged particles accidentally. Since the "multiples veto" incorporated in the trigger condition "N" (Necessary) required that one and only one channel in each tray was fired for an event, these accidentals caused a loss of events.

To study this effect, "compute" signals were sent into the fast electronics at random from a pulser during AGS beam pulses, and the number of times any one of the hodoscope trays fired in coincidence with the "compute" signal was counted. From these counts, the multiple veto inefficiency was calculated and found to be $3.0 \pm 0.2\%$. A similar result was obtained with the AGS off, and the major part of the effect was ascribed to noise and radiation not associated with the AGS.

H. Systematic Uncertainties

Three kinds of uncertainties are discussed in this section. The first one is the overall uncertainty in the absolute normalization. The second is the uncertainty in the normalization at one beam momentum relative to that at another beam momentum, and the third is the uncertainty for a given beam momentum at one center-of-mass angle relative to that at a different angle.

1) Uncertainty in the absolute normalization. The following is a list of the average uncertainties for all center-of-mass angles and beam momenta:

	$\bar{p}+p\rightarrow\pi^{+}+\pi^{-}$	$\bar{p}+p\rightarrow k^{+}+k^{-}$
Radiative correction	4 %	3 %
Hodoscope inefficiency	0.6%	0.6%
Loss due to "ϕ" requirement	1 %	1 %
Loss due to decay	1 %	5 %
Loss due to interaction	4.5%	3 %
Multiples veto	0.2%	0.2%
Measurement errors	0.5%	0.5%
Calculation of attenuation factor, $A(\Theta_{C.M.}, \phi)$ (see Chapter 4, Section G)	1.5%	1.5%
Calculation of effective target length	1 %	1 %
Liquid hydrogen density	1 %	1 %

The total estimated uncertainty in the absolute normalization was the quadratic sum of the above, and was ±6.5% for both $\pi^{\pm}$-pair and $k^{\pm}$-pair events.

2) Uncertainty in the relative normalization between different beam momenta. The following is a list, for two extreme momenta, of the estimated uncertainties in the momentum dependent systematic corrections for the $\pi^{\pm}$-pair cross sections, averaged over all center-of-mass angles:

Nominal beam momentum	1.00 GeV/c	2.5 GeV/c	Difference
Radiative correction	3.5%	4.0%	0.5%
Loss due to "ϕ" requirement	0.5%	1.0%	0.5%
Loss due to interaction	4.0%	5.0%	1.0%

The quadratic sum of the differences was 1.2%. Therefore, the uncertainty in the normalization at one beam momentum relative to that at another momentum was 0.8% per GeV/c momentum difference for the $\pi^{\pm}$-pair cross sections. For $\bar{p}$-p annihilation into $k^{\pm}$-pairs, it was found to be 1% per GeV/c. These were both small and insignificant compared to the statistical uncertainty of this experiment.

3) Systematic uncertainty between different center-of-mass angles. Because of the assumptions made in the calculation of the radiative correction, the loss due to decay, and the loss due to interaction, the uncertainty in the corrections at one center-of-mass angle relative to that at another angle was difficult to determine. It was

estimated not to exceed 0.08% per degree center-of-mass angle for all beam momenta. Over the 50^{o} angular range of this experiment, this amounted to an uncertainty of ± 4%. At no beam momentum was it of comparable importance to the statistical uncertainties.

I. Summary

As an example, the systematic corrections for the 1.75 GeV/c data are summarized in Table 5.4. The $\pi^{\pm}$-pair and $k^{\pm}$-pair cross sections before and after the corrections are also given for comparison.

Table 5.4 Systematic corrections (1.75 GeV/c nominal antiproton momentum)

$\theta_{C.M.}$	Radiative Corrections	Hodoscope Inefficiency	Loss due to "φ" Requirement	Loss due to Decay	Loss due to Interactions	Multiples veto Inefficiency	Measure-ment errors	Average attenuation factor $\int A(\theta_{C.M.}, z)dz / \int dz$	$\frac{d\sigma}{d\Omega}(\theta_{C.M.})_+ \frac{d\sigma}{d\Omega}(\pi - \theta_{C.M.})$ μb/sr Preliminary	Final
	$\bar{p} + p \to \pi^+ + \pi^-$									
47.5	7.4 ± 4.0%	7.8 ± 0.6%	0.8 ± 0.7%	↑	10.3 ± 4.0%	3.0 ± 0.2%	1.5 ± 0.5%	1.49 ± 0.02	15.5 ± 3.2	21.0 ± 4.3
52.5	7.5 ± 4.0	↓	↓	Negligible	9.6 ± 4.0	↓	↓	1.51 ± 0.02	26.1 ± 2.6	35.1 ± 3.5
57.5	7.7 ± 4.0				9.0 ± 4.0			1.52 ± 0.02	24.9 ± 2.3	33.3 ± 3.1
62.5	7.8 ± 4.0				8.5 ± 4.0			1.54 ± 0.02	13.6 ± 1.6	18.1 ± 2.1
67.5	7.9 ± 4.0				8.1 ± 4.0			1.54 ± 0.02	11.6 ± 1.4	15.5 ± 1.9
72.5	8.0 ± 4.0				7.8 ± 4.0			1.55 ± 0.02	12.9 ± 1.4	17.1 ± 1.9
77.5	8.0 ± 4.0				7.6 ± 4.0			1.55 ± 0.02	17.8 ± 1.5	23.6 ± 2.0
82.5	8.0 ± 4.0				7.6 ± 4.0			1.54 ± 0.02	23.6 ± 1.7	31.3 ± 2.2
87.5	8.1 ± 4.0	↓	↓	↓	7.6 ± 4.0	↓	↓	1.52 ± 0.02	28.2 ± 1.8	37.4 ± 2.3
	$\bar{p} + p \to k^+ + k^-$									
47.5	4.6 ± 3.0%	7.8 ± 0.6%	0.8 ± 0.7%	12.3 ± 5.0%	7.0 ± 3%	3.0 ± 0.2%	1.5 ± 0.5%	1.46 ± 0.02	3.3 ± 2.1	4.8 ± 3.1
52.5	4.7 ± 3.0	↓	↓	11.5 ± 5.0	6.6 ± 3	↓	↓	1.48 ± 0.02	6.3 ± 1.4	9.2 ± 2.1
57.5	4.8 ± 3.0			10.8 ± 5.0	6.2 ± 3			1.50 ± 0.02	4.9 ± 1.2	7.1 ± 1.6
62.5	4.8 ± 3.0			10.2 ± 5.0	5.9 ± 3			1.51 ± 0.02	5.0 ± 1.0	7.1 ± 1.5
67.5	4.9 ± 3.0			9.8 ± 5.0	5.6 ± 3			1.52 ± 0.02	3.7 ± 0.9	5.2 ± 1.3
72.5	4.9 ± 3.0			9.4 ± 5.0	5.5 ± 3			1.52 ± 0.02	6.5 ± 1.1	9.1 ± 1.5
77.5	5.0 ± 3.0			9.2 ± 5.0	5.4 ± 3			1.52 ± 0.02	5.1 ± 0.9	7.2 ± 1.3
82.5	5.0 ± 3.0			9.2 ± 5.0	5.3 ± 3			1.52 ± 0.02	5.7 ± 0.9	8.0 ± 1.2
87.5	5.0 ± 3.0	↓	↓	9.2 ± 5.0	5.3 ± 3	↓	↓	1.51 ± 0.02	7.5 ± 1.0	10.5 ± 1.4

The errors in the final cross sections are statistical. The uncertainty in the normalization is ± 6.5%.

VI. RESULTS AND DISCUSSIONS

A. Introduction and Summary

In this chapter, the results of this experiment are presented and compared with other data for the two-meson annihilations. The application of a Regge-resonance interference model to the annihilation modes is discussed. It is found that within the angular range of this experiment, Regge contribution is small. Assuming that the annihilations proceed via resonances, an expression is derived for the angular distribution. A least square fitting of the data of this experiment with this expression would have been very laborious and was not carried out.

Meson resonances at 2.20 GeV and 2.38 GeV observed in other experiments may be responsible for some of the features found in the angular distributions. However, no detailed conclusions could be drawn from the data.

B. Results

In presenting the results, runs at the same nominal momentum are grouped together. Table 6.1 gives the values of average laboratory interaction momentum at which data were taken, adjusted to give the proper calculated values of m_π^2 and m_k^2 (as discussed in Chapter 4). The full width at half maximum associated with each momentum includes, besides the momentum spread in the beam and the energy loss of the antiproton in the target, a spread from combining runs at slightly different momenta. Corresponding total energy in the center-of-mass system at each beam momentum is also given for reference.

Tables 6.2 and 6.3, and Figs. 6.1 and 6.2 show the cross sections measured in this experiment. As discussed in Chapter 4, the cross sections are in the form $[\frac{d\sigma}{d\Omega}(\Theta_{C.M.}) + \frac{d\sigma}{d\Omega}(\pi - \Theta_{C.M.})]$, because the charges of the final particles were not determined. The errors shown are purely statistical.

Systematic errors have been discussed in the previous chapter. They introduce an uncertainty in the absolute normalization, estimated to be $\pm 6.5\%$ for both $\pi^\pm$-pairs and $k^\pm$-pairs. Uncertainties in the systematic corrections lead to two other types of error: an uncertainty in the normalization for an angular distribution at one beam momentum relative to that at another momentum, estimated to be about $\pm$ 1% per GeV/c momentum difference; and, at a given momentum, an uncertainty at one center-of-mass angle relative to that at another angle, estimated to be $\pm$ 0.08% per degree. The last two uncertainties are both unimportant compared to the statistical errors.

Table 6.1 Antiproton beam momenta and total C. M. system energies for this experiment

Nominal Momentum (GeV/c)	Average Interaction Momentum (GeV/c)	FWHM (GeV/c)	Total C. M. Energy (GeV)	FWHM (GeV)
0.750	0.720	0.156	1.998	0.023
0.875	0.840	0.132	2.033	0.021
0.940	0.890	0.114	2.049	0.018
1.000	0.970	0.118	2.074	0.019
1.125	1.090	0.106	2.114	0.018
1.250	1.190	0.140	2.148	0.024
1.375	1.340	0.116	2.200	0.020
1.500	1.400	0.136	2.221	0.024
1.625	1.585	0.128	2.287	0.023
1.750	1.675	0.128	2.318	0.023
1.875	1.815	0.130	2.368	0.023
2.000	1.910	0.144	2.401	0.025
2.250	2.125	0.138	2.476	0.024
2.500	2.365	0.158	2.559	0.027
2.750	2.615	0.172	2.643	0.029

Table 6.2 Angular distribution $[\frac{d\sigma}{d\Omega}(\theta_{C.M.}) + \frac{d\sigma}{d\Omega}(\pi - \theta_{C.M.})]$ in μb/sr for $\bar{p} + p \rightarrow \pi^+ + \pi^-$

$\sqrt{s}$ = total energy in C. M. system, and p = lab antiproton momentum

$\sqrt{s}$ (GeV) =	2.00	2.03	2.05	2.07	2.11	2.15	2.20	2.22
p (GeV/c) =	0.720	0.840	0.890	0.970	1.090	1.190	1.340	1.400
27.5^o	58. ± 24.	137. ± 29.						
42.5^o	74. ± 20.	131. ± 21.				49. ± 15.		
47.5^o	94. ± 19.	81. ± 14.	74. ± 21.	75. ± 12	77. ± 10.	50.7 ± 6.0	50.8 ± 7.5	41.5 ± 4.4
52.5^o	66. ± 14.	63. ± 11.	61.5 ± 8.7	46.5 ± 5.8	51.0 ± 6.5	38.5 ± 4.4	44.6 ± 6.0	39.6 ± 3.6
57.5^o	42. ± 10.	41. ± 8.	42.9 ± 6.4	39.5 ± 4.8	39.3 ± 5.1	26.0 ± 3.2	29.5 ± 4.4	30.7 ± 2.9
62.5^o	44. ± 10.	48. ± 8.	42.9 ± 5.8	43.0 ± 4.7	35.1 ± 4.5	21.9 ± 2.7	26.8 ± 3.8	28.1 ± 2.6
67.5^o	44. ± 9.	43. ± 7.	45.9 ± 5.6	43.2 ± 4.4	32.6 ± 4.0	29.8 ± 2.9	24.1 ± 3.4	24.2 ± 2.2
72.5^o	30. ± 7.	52. ± 7.	50.9 ± 5.8	47.8 ± 4.4	46.3 ± 4.6	41.7 ± 3.3	36.5 ± 3.9	30.6 ± 2.3
77.5^o	28. ± 7.	43. ± 7.	54.1 ± 5.7	56.7 ± 4.6	57.6 ± 4.9	59.8 ± 3.7	47.3 ± 4.3	36.2 ± 2.4
82.5^o	57. ± 9.	69. ± 8.	68.2 ± 6.1	72.2 ± 5.0	70.4 ± 5.3	68.1 ± 3.9	56.9 ± 4.5	46.5 ± 2.6
87.5^o	61. ± 9.	64. ± 8.	65.4 ± 5.9	79.4 ± 5.1	83.7 ± 5.6	76.9 ± 4.0	65.8 ± 4.7	61.7 ± 2.9

$\sqrt{s}$ (GeV) =	2.29	2.32	2.37	2.40	2.48	2.56	2.64
p (GeV/c) =	1.585	1.675	1.815	1.910	2.125	2.365	2.615
47.5^o	31.3 ± 5.9	21.0 ± 4.3	26.5 ± 7.6				
52.5^o	40.1 ± 5.3	35.1 ± 3.5	31.0 ± 4.0	25.6 ± 2.5	13.7 ± 2.3	9.2 ± 2.0	
57.5^o	31.5 ± 4.2	33.3 ± 3.1	20.0 ± 2.8	26.2 ± 2.3	16.2 ± 1.8	11.9 ± 1.7	5.4 ± 1.4
62.5^o	18.6 ± 3.1	18.1 ± 2.1	21.5 ± 2.7	18.5 ± 1.8	18.5 ± 1.7	11.2 ± 1.5	7.8 ± 1.4
67.5^o	16.6 ± 2.8	15.5 ± 1.9	11.5 ± 1.9	15.6 ± 1.5	9.9 ± 1.2	7.3 ± 1.1	5.5 ± 1.0
72.5^o	24.8 ± 3.0	17.1 ± 1.9	12.6 ± 2.0	12.4 ± 1.3	9.0 ± 1.1	6.7 ± 1.0	3.7 ± 0.9
77.5^o	35.1 ± 3.4	23.6 ± 2.0	14.2 ± 1.9	12.5 ± 1.2	9.8 ± 1.1	4.4 ± 0.9	2.1 ± 0.8
82.5^o	37.3 ± 3.4	31.3 ± 2.2	28.3 ± 2.5	20.0 ± 1.4	9.9 ± 1.1	6.4 ± 0.9	2.5 ± 0.8
87.5^o	47.6 ± 3.7	37.4 ± 2.3	30.4 ± 2.5	22.3 ± 1.5	12.0 ± 1.1	4.6 ± 0.9	3.5 ± 0.8

The errors in the cross sections are statistical.

The uncertainty in the normalization is ± 6.5%.

Table 6.3 Angular distribution $[\frac{d\sigma}{d\Omega}(\theta_{C.M.}) + \frac{d\sigma}{d\Omega}(\pi - \theta_{C.M.})]$ in μb/sr for $\bar{p} + p \to k^+ + k^-$

$\sqrt{s}$ = total energy in C. M. system, and p = lab antiproton momentum

$\sqrt{s}$ (GeV)=	2.00	2.03	2.05	2.07	2.11	2.15	2.20	2.22
p (GeV/c)=	0.720	0.840	0.890	0.970	1.090	1.190	1.340	1.400
37.5°	30. ± 19.	28. ± 16.						
42.5°	29. ± 13.	20. ± 10.			8.3 ± 6.5	9.0 ± 4.5		
47.5°	42. ± 14.	34. ± 10.	19.2 ± 7.3	18.6 ± 4.7	10.1 ± 4.1	8.1 ± 2.5	19.2 ± 4.7	11.9 ± 2.9
52.5°	12.5 ± 7.2	8.1 ± 4.4	18.6 ± 4.7	24.2 ± 4.6	14.2 ± 3.7	10.9 ± 2.6	10.0 ± 3.4	8.0 ± 1.9
57.5°	8.1 ± 6.0	13.6 ± 5.4	18.7 ± 4.6	25.8 ± 4.1	15.9 ± 3.5	10.6 ± 2.3	8.5 ± 2.8	8.6 ± 1.7
62.5°	13.2 ± 6.3	19.3 ± 5.6	21.3 ± 4.5	21.6 ± 3.6	14.2 ± 3.1	16.8 ± 2.5	8.4 ± 2.4	10.7 ± 1.8
67.5°	13.8 ± 5.5	11.4 ± 4.6	20.9 ± 4.4	22.0 ± 3.4	16.4 ± 3.1	13.2 ± 2.2	12.0 ± 2.7	10.9 ± 1.6
72.5°	4.5 ± 3.7	14.0 ± 4.4	11.4 ± 3.1	17.4 ± 2.8	15.8 ± 2.8	17.0 ± 2.2	13.8 ± 2.7	9.8 ± 1.5
77.5°	10.4 ± 4.8	16.0 ± 4.6	20.8 ± 3.7	16.6 ± 2.8	16.5 ± 2.9	13.5 ± 2.0	11.3 ± 2.5	11.3 ± 1.5
82.5°	10.8 ± 4.4	15.2 ± 4.0	14.2 ± 3.2	15.6 ± 2.5	19.4 ± 3.0	11.4 ± 1.9	11.0 ± 2.3	9.6 ± 1.4
87.5°	9.4 ± 4.6	17.3 ± 4.3	13.1 ± 3.0	13.4 ± 2.3	18.7 ± 2.8	15.8 ± 2.0	15.3 ± 2.5	14.6 ± 1.5

$\sqrt{s}$ (GeV)=	2.29	2.32	2.37	2.40	2.48	2.56	2.64
p (GeV/c)=	1.585	1.675	1.815	1.910	2.125	2.365	2.615
47.5°		4.8 ± 3.1					
52.5°	8.6 ± 2.7	9.2 ± 2.1	7.1 ± 2.4	3.8 ± 1.4	1.7 ± 1.2	1.5 ± 1.1	
57.5°	7.4 ± 2.4	7.1 ± 1.6	7.3 ± 1.8	5.9 ± 1.2	1.7 ± 0.8	1.9 ± 1.0	$0.5^{+1.1}_{-0.5}$
62.5°	4.0 ± 2.1	7.1 ± 1.5	2.6 ± 1.3	4.7 ± 1.1	2.1 ± 0.8	1.7 ± 0.8	1.0 ± 0.8
67.5°	10.4 ± 2.3	5.2 ± 1.3	3.5 ± 1.3	3.6 ± 0.9	3.8 ± 0.8	0.6 ± 0.6	$0.1^{+0.8}_{-0.1}$
72.5°	9.5 ± 2.2	9.1 ± 1.5	5.1 ± 1.3	4.0 ± 0.9	3.6 ± 0.7	2.0 ± 0.8	1.0 ± 0.7
77.5°	8.4 ± 1.8	7.2 ± 1.3	8.1 ± 1.5	6.0 ± 1.0	3.8 ± 0.8	1.0 ± 0.6	1.3 ± 0.7
82.5°	9.2 ± 1.9	8.0 ± 1.2	9.0 ± 1.6	7.6 ± 1.0	5.7 ± 0.9	3.3 ± 0.8	1.9 ± 0.7
87.5°	10.9 ± 2.0	10.5 ± 1.4	8.4 ± 1.5	8.2 ± 1.0	4.9 ± 0.8	2.3 ± 0.7	3.1 ± 0.9

The errors in the cross sections are statistical.

The uncertainty in the normalization is ± 6.5%.

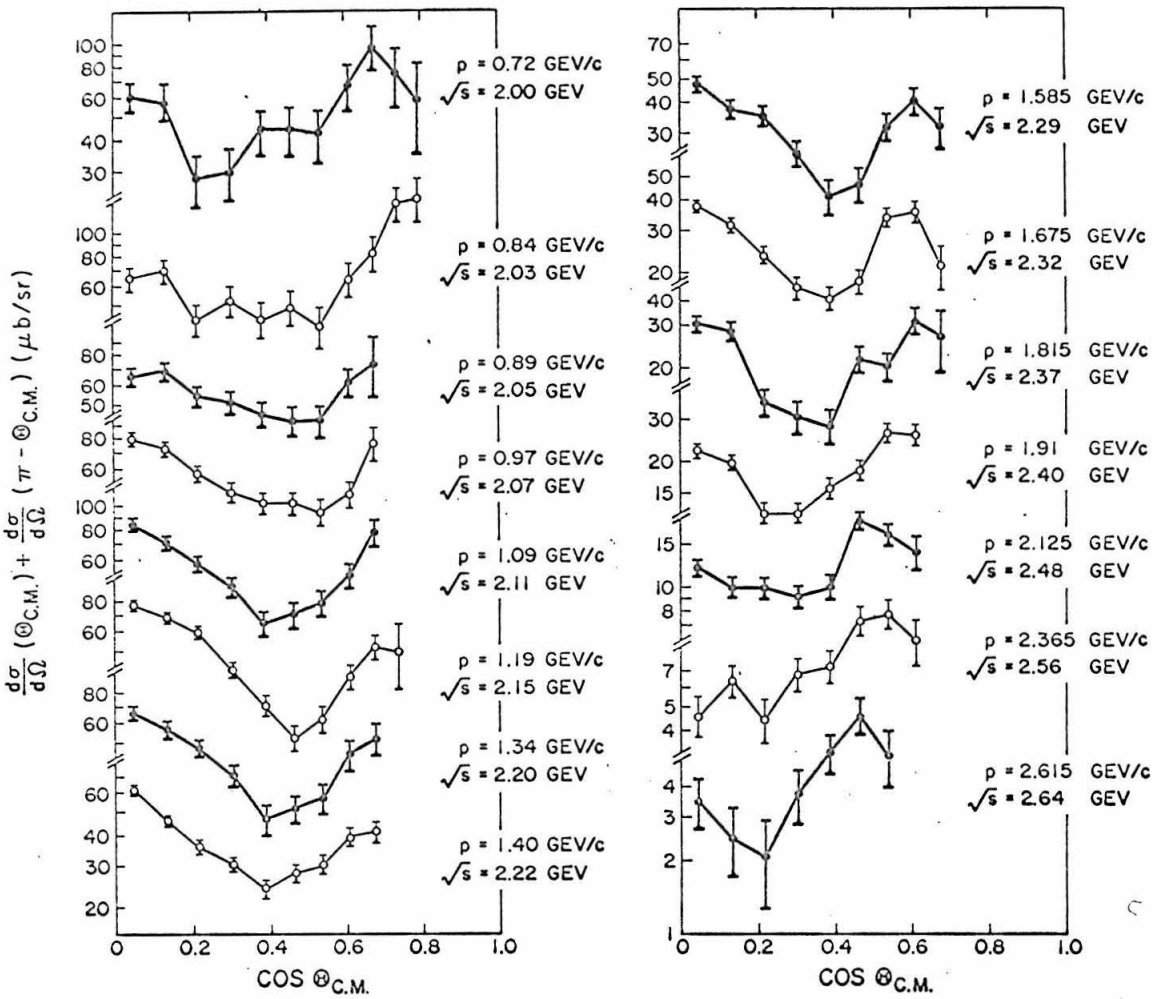

The errors in the cross sections are statistical.

The uncertainty in the normalization is ± 6.5%.

Fig. 6.1 Angular distributions $\left[\frac{d\sigma}{d\Omega}(\Theta_{C.M.}) + \frac{d\sigma}{d\Omega}(\pi - \Theta_{C.M.})\right]$ in μb/sr for $\bar{p} + p \rightarrow \pi^+ + \pi^-$

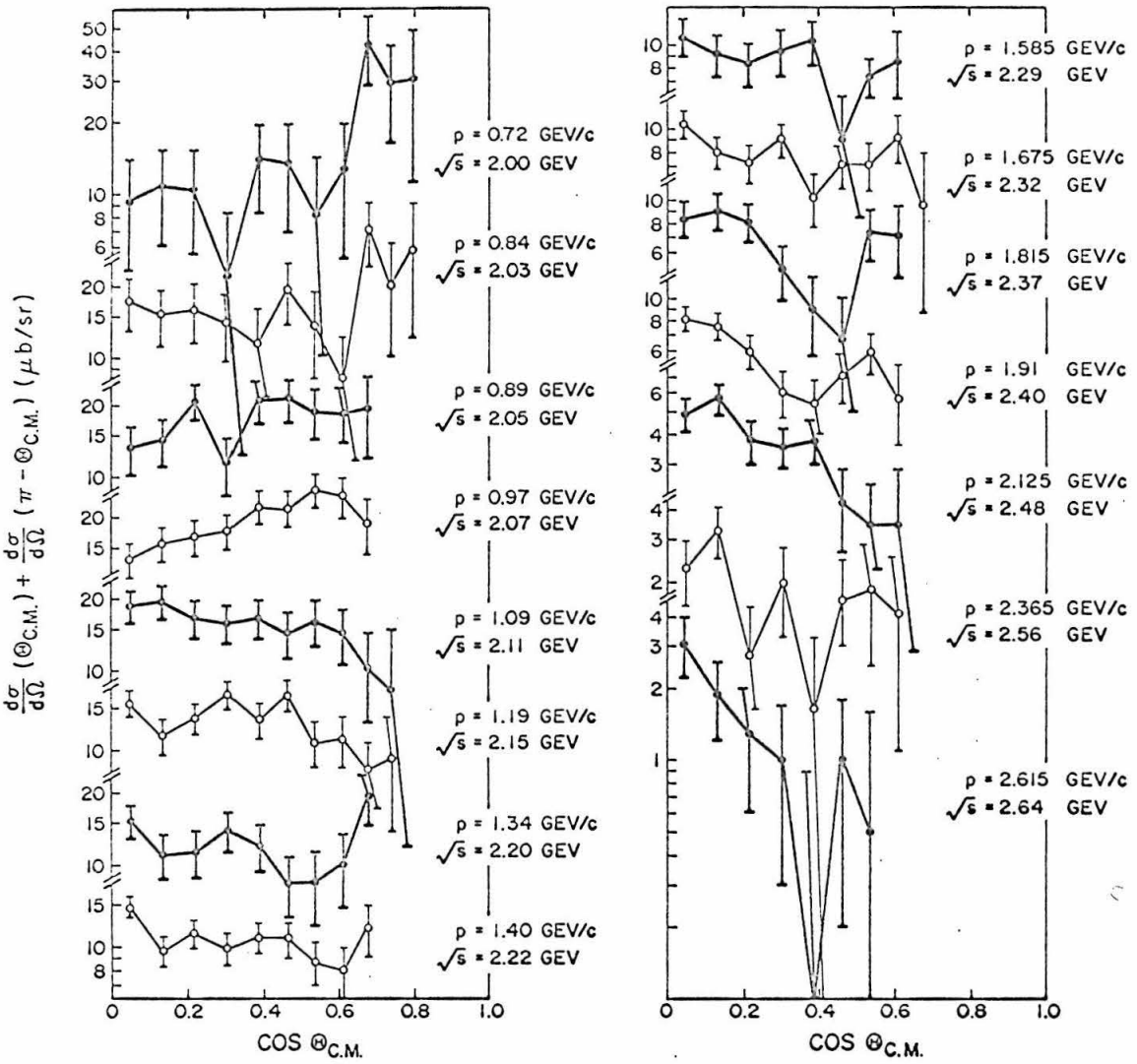

The errors in the cross sections are statistical.
The uncertainty in the normalization is ± 6.5%.

Fig. 6.2 Angular distribution $[\frac{d\sigma}{d\Omega}(\Theta_{C.M.}) + \frac{d\sigma}{d\Omega}(\pi - \Theta_{C.M.})]$ in μb/sr for $\bar{p} + p \rightarrow k^+ + k^-$

The most striking feature in the angular distributions is the peaking in the $\bar{p} + p \rightarrow \pi^+ + \pi^-$ cross section at $\Theta_{C.M.} = 90^o$, most pronounced at momenta near 1.1 GeV/c. As the total energy ($\sqrt{s}$) increases, the peak grows in size until $\sqrt{s}$ is about 2.1 GeV (antiproton momentum $\simeq$ 1.375 GeV/c), then it diminishes with increasing total energy, and disappears almost completely at $\sqrt{s} \simeq 2.6$ GeV.

Fig. 6.3 is a comparison of the average cross section in the range $80^o \leq \Theta_{C.M.} \leq 100^o$ with that in the combined angular ranges $45^o \leq \Theta_{C.M.} \leq 55^o$ and $125^o \leq \Theta_{C.M.} \leq 135^o$. The phenomenon mentioned above can clearly be seen. The sum of the more forward and backward cross sections shows, within statistics, a steady decrease with higher total energy, while the average 90^o cross section shows peaking at $\sqrt{s} \simeq 2.1$ GeV/c.

From Fig. 6.2, it can be seen that the $\bar{p} + p \rightarrow k^+ + k^-$ angular distributions show no striking variations at the lower total energies. A peak at $\Theta_{C.M.} = 90^o$, however, seems to develop at $\sqrt{s} = 2.3$ GeV. The graphs for $\bar{p} + p \rightarrow k^+ + k^-$ analogous to Fig. 6.3 are shown in Fig. 6.4. Again, the average 90^o cross sections show some peaking at $\sqrt{s} \simeq 2.1$ GeV. However, because of the poor statistics, no firm conclusion can be drawn.

The $k^{\pm}/\pi^{\pm}$ cross section ratio stays fairly constant at about 1/3.4 throughout the total energy range of this experiment.

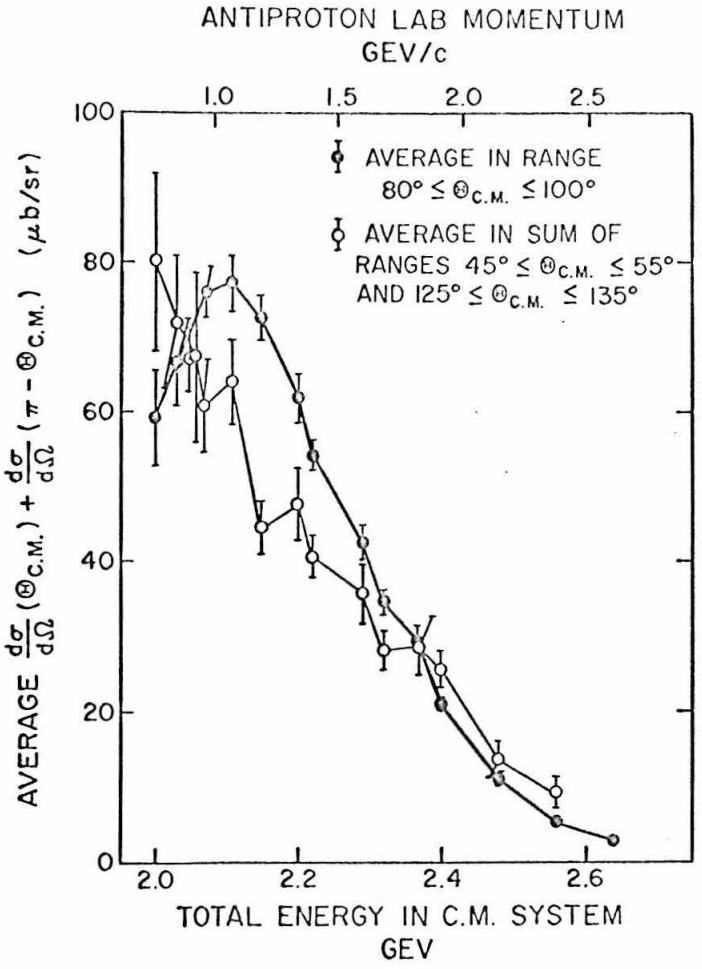

Fig. 6.3 Comparison of the average of forward and backward cross sections with 90^{o} cross section for $\bar{p} + p \rightarrow \pi^{+} + \pi^{-}$

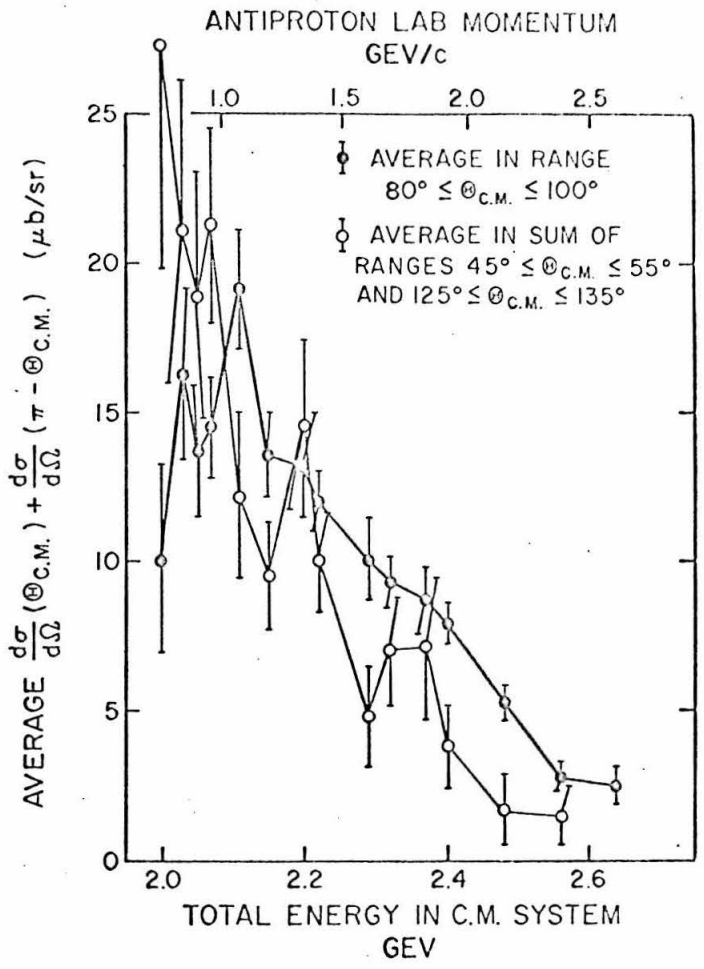

Fig. 6.4 Comparison of the average of forward and backward cross sections with 90^{o} cross section for $\bar{p} + p \rightarrow k^{+} + k^{-}$

C. Comparison with other Experiments

Previous to this experiment, all the attempts to measure $\bar{p} + p \rightarrow \pi^+ + \pi^-$ and $\bar{p} + p \rightarrow k^+ + k^-$ had been done with bubble chambers. Except for the experiment by Lynch et al.[2),3)] at 1.61 GeV/c $\bar{p}$ momentum, the other ones were done either at energies greater than the range covered in this experiment,[12),13),14)] or for antiprotons at rest.[15)]

For annihilation at rest, the $\pi^{\pm}$-pair to $k^{\pm}$-pair ratio has been found to be about 3 to 1, not significantly different from that in the energy range of this experiment.

At 1.61 GeV/c, Lynch et al. obtained angular distributions for the two annihilation modes. The result for $\bar{p} + p \rightarrow \pi^+ + \pi^-$ has been folded across $\Theta_{C.M.} = 90^o$ to yield $[\frac{d\sigma}{d\Omega}(\Theta_{C.M.}) + \frac{d\sigma}{d\Omega}(\pi - \Theta_{C.M.})]$ and compared to the angular distribution obtained in this experiment at 1.585 GeV/c, as shown in Fig. 6.5. There seems to be consistency in the shapes of the distributions, but the result of this experiment is about a factor of two larger. The large errors shown for the Lynch data reflect the poor statistics (22 events total).

Seven of the eleven $k^{\pm}$-pair events seen by Lynch et al. were in forward directions, to which this experiment was not sensitive. However, in the angular range where the two experiments overlap, Lynch et al. again observed a cross section smaller by about a factor of two.

At the higher energies, very few events have been observed. However, the results show that the total cross section diminishes steadily with increasing energy, consistent with the trend indicated by this experiment. All the results of other annihilation in flight experiments are summarized in Table 6.4.

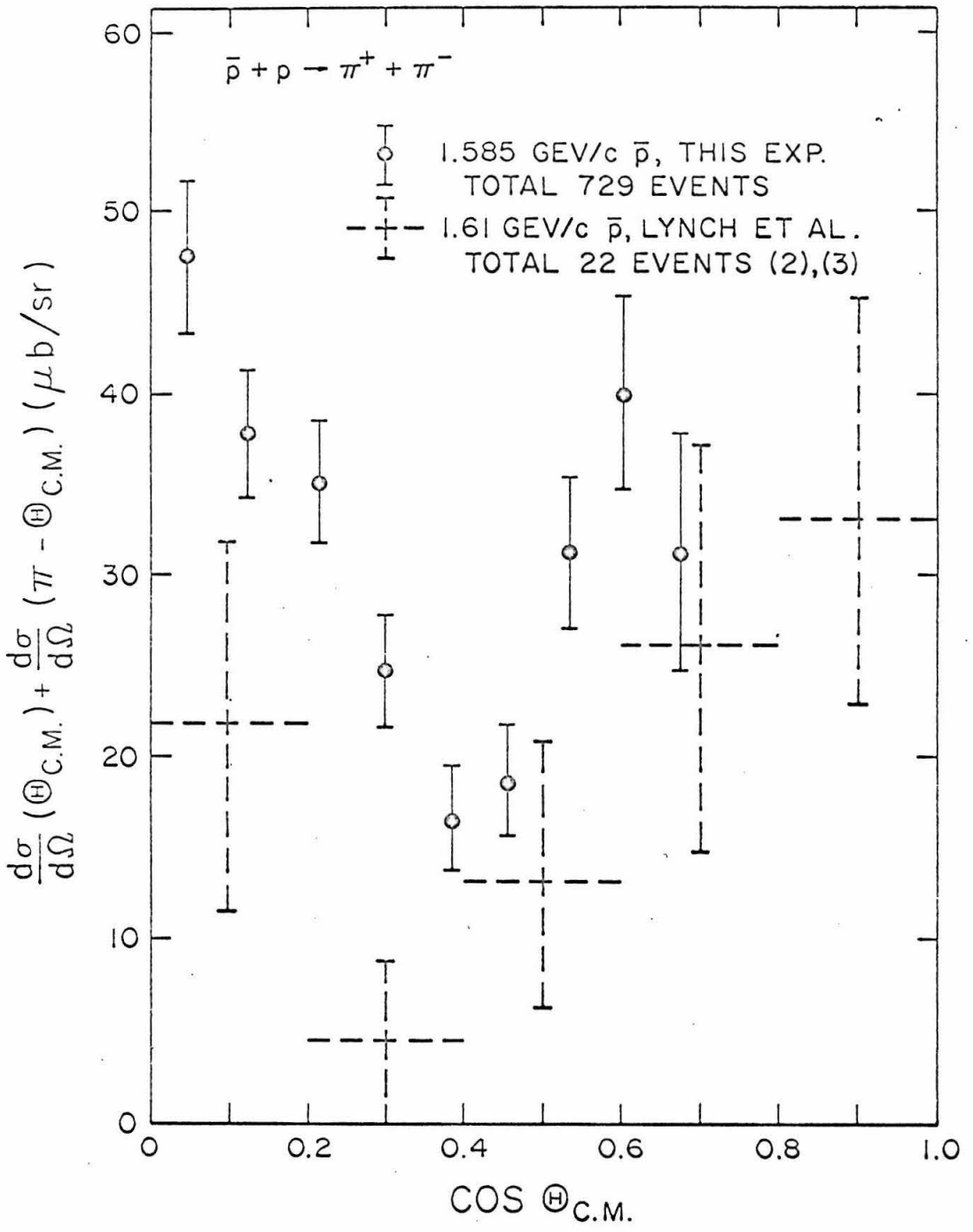

Fig. 6.5 Comparison of 1.61 GeV/c $\bar{p} + p \rightarrow \pi^+ + \pi^-$ result obtained by Lynch et al. [2), 3)] with the 1.585 GeV/c result of this experiment

Table 6.4 Summary of bubble chamber experiments on antiproton-proton annihilation in flight into charged meson pairs

	$\bar{p} + p \rightarrow \pi^+ + \pi^-$		$\bar{p} + p \rightarrow k^+ + k^-$		
$\bar{p}$ beam momentum	no. of events	total cross section	no. of events	total cross section	Ref.
1.61 GeV/c	22	119 ± 30 μb	11	55 ± 18 μb	(2), (3)
3.00 GeV/c	< 3	< 10 μb	< 3	< 10 μb	(13)
3.28 GeV/c		< 25 μb		< 25 μb	(12)
3.66 GeV/c	3	6.6 ± 3.5 μb	0	< 2.2 μb	(14)
4.00 GeV/c	1.2 ± 1.2	3.5 ± 3.5 μb	< 1.2	< 3.5 μb	(12)

D. Theoretical Considerations

(1) General. One of the reasons that make the annihilation

$$\bar{p} + p \rightarrow \text{meson} + \text{antimeson}$$

interesting theoretically is that it is the cross channel of meson-proton elastic scattering:

$$\text{meson} + p \rightarrow \text{meson} + p.$$

Furthermore, π-p elastic scattering has the special significance of being one of the most fundamental reactions, and one which has been most thoroughly studied. A great amount of experimental data has been obtained in measurements of the scattering cross section, offering theorists a starting point for various models of the strong interaction.

For π-p elastic scattering in the backward hemisphere, one of the more successful models is the fermion-Regge-pole-resonance interference model.[16),17)] In this theory, the interaction is supposed to be the combined result of two mechanisms shown in Fig. 6.6. The first mechanism (a) represents

$$\pi + p \rightarrow \text{fermion resonance} \rightarrow \pi + p,$$

while the second (b) depicts the exchange of a Regge pole. At high energies, the backward π-p elastic scattering is thought to be dominated by Regge exchange, and at the intermediate angles, it is dominated by interaction via resonances.

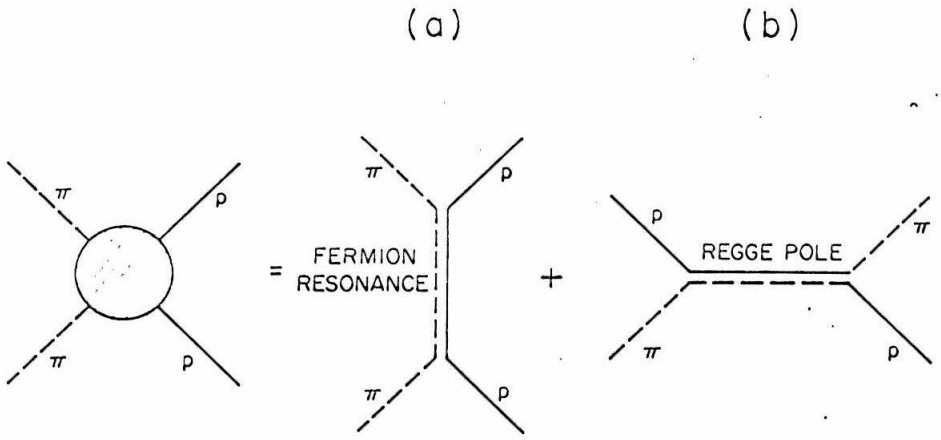

Fig. 6.6 Diagrams for π-p elastic scattering in the backward hemisphere

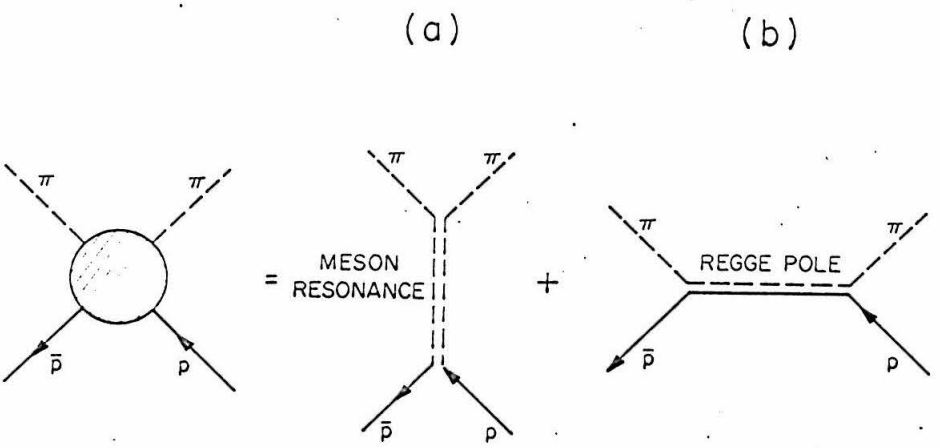

Fig. 6.7 Diagrams for $\bar{p} + p \rightarrow \pi^+ + \pi^-$

A similar approach can be used to try to understand the angular distribution for $\bar{p} + p \rightarrow \pi^+ + \pi^-$ (Fig. 6.7) and also for $\bar{p} + p \rightarrow k^+ + k^-$. In the following, the discussion will concentrate on the $\pi^{\pm}$-pair mode. A few comments about the $k^{\pm}$-pair mode will be made at the end of this section.

(2) Regge exchange in $\bar{p} + p \rightarrow \pi^+ + \pi^-$. There are two possibilities, shown in Fig. 6.8, for the Regge exchange diagram in the case of antiproton-proton annihilation into π^+ and π^-. In one case, the charge is 2. This diagram dominates for events with the final π^+ direction close to that of the initial antiproton. This is just the crossed Regge diagram for backward π^--p scattering (Fig. 6.9(1)). In the other case, Regge pole exchange with zero charge, the final π^- direction is close to that of the initial antiproton. It is the crossed diagram for backward π^+-p scattering (Fig. 6.9 (2)). Thus, assuming crossing symmetry, a Regge calculation for $\bar{p} + p \rightarrow \pi^+ + \pi^-$ can borrow from that for π-p elastic scattering.

In an extensive application of the interference technique by V. Barger and D. Cline,[17] it is shown that the amplitude in Fig. 6.9 (2) is dominated by the exchange of the Regge trajectory Δ_δ. (hypercharge Y = 1, isospin I = 3/2 parity P = +, signature τ = -) On the other hand, C. B. Chiu and J. D. Stack[18] showed that the amplitude in Fig. 6.9 (1) is dominated by the exchange of N_α (Y = 1, I = 1/2, P = +, τ = +).

The crossing from π-p elastic scattering to $\bar{p} + p \rightarrow \pi^+ + \pi^-$ is also worked out by Barger and Cline.[19] They showed that

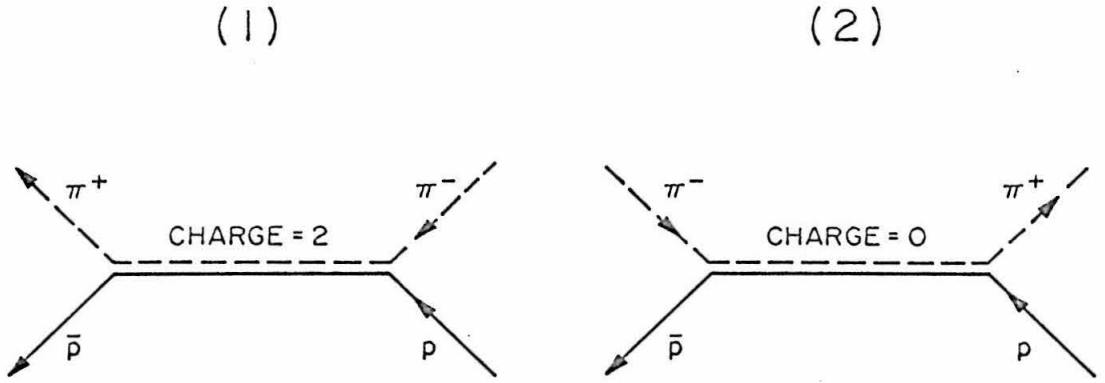

Fig. 6.8 Two kinds of Regge trajectories for $\bar{p} + p \rightarrow \pi^+ + \pi^-$

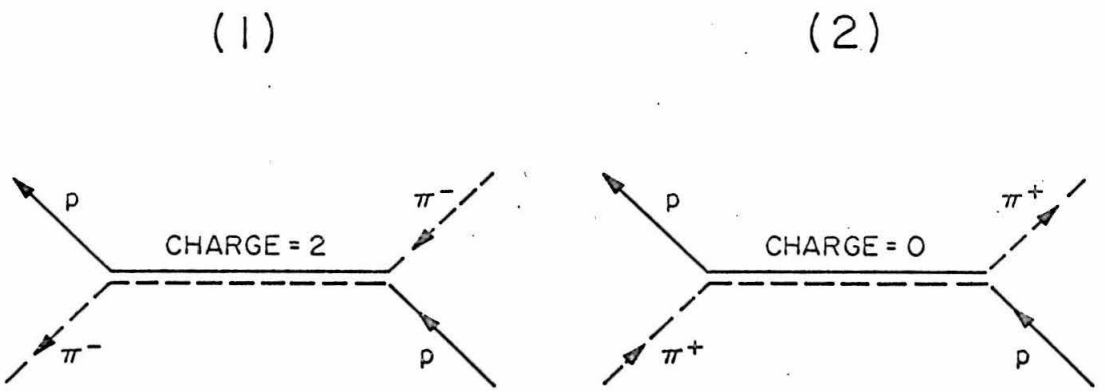

Fig. 6.9 Two kinds of Regge trajectories for $\pi + p \rightarrow \pi + p$

$$\left.\frac{d\sigma}{du}\right|_{\text{annihilation}} = \frac{1}{2}\left.\frac{d\sigma}{du}\right|_{\text{scattering}} \frac{[s - (M+\mu)^2][s - (M-\mu)^2]}{s[s + u + 2D^2]}$$

where M = nucleon mass,

μ = meson mass,

$\sqrt{s}$ = total energy in center-of-mass system,

u = cross momentum transfer $= M^2 + \mu^2 - \frac{s}{2} - 2\sqrt{\frac{s}{4} - \mu^2}\sqrt{\frac{s}{4} - M^2}\cos\Theta_{C.M.}$,

$\Theta_{C.M.}$ = C. M. angle between initial $\bar{p}$ and final π^-,

$D^2 = M^2 - \mu^2$.

A calculation was done for the energy range of this experiment. The two Regge cross sections were added together to give $[\frac{d\sigma}{d\Omega}(\Theta_{C.M.}) + \frac{d\sigma}{d\Omega}(\pi - \Theta_{C.M.})]$. It was found that in the angular range of this experiment, the Regge contribution was small, being less than 1/3 of the cross section at the most forward (and backward) angles ($\cos\Theta \approx 0.6$). Its importance was even less at the intermediate angles.

Thus, according to this particular theoretical model, the cross section observed here should be ascribed to annihilation via resonances.

(3) Resonances in $\bar{p} + p \rightarrow \pi^+ + \pi^-$. The left side of Table 6.5 is a list of the possible quantum numbers for the $\bar{p}$-p system, up to angular momentum quantum number $\ell = 4$. The spins of the proton and antiproton can be either parallel, forming a triplet state with

Table 6.5 Quantum numbers for $\bar{p}$-p systems and π^+-π^- (or k^+-k^-) systems

$\bar{p}$ p						$\pi^+ \pi^-$ (or k^+k^-)		
ℓ	S	J	C $(-)^{\ell+S}$	P $(-)^{\ell+1}$	$\bar{p}$ p State	C $(-)^J$	P $(-)^J$	
0	0	0	+	-	$^1S^0$	+	+	
0	1	1	-	-	$^3S^1$	-	-	ν
1	0	1	-	+	$^1p^1$	-	-	
1	1	0	+	+	$^3p^0$	+	+	ν
1	1	1	+	+	$^3p^1$	-	-	
1	1	2	+	+	$^3p^2$	+	+	ν
2	0	2	+	-	$^1D^2$	+	+	
2	1	1	-	-	$^3D^1$	-	-	ν
2	1	2	-	-	$^3D^2$	+	+	
2	1	3	-	-	$^3D^3$	-	-	ν
3	0	3	-	+	$^1F^3$	-	-	
3	1	2	+	+	$^3F^2$	+	+	ν
3	1	3	+	+	$^3F^3$	-	-	
3	1	4	+	+	$^3F^4$	+	+	ν
4	0	4	+	-	$^1G^4$	+	+	
4	1	3	-	-	$^3G^3$	-	-	ν
4	1	4	-	-	$^3G^4$	+	+	
4	1	5	-	-	$^3G^5$	-	-	ν

$S = 1$, or antiparallel, forming a singlet state with $S = 0$. Thus, except for $\ell = 0$, there are four possible different combinations of the quantum numbers ℓ, S, J for every ℓ, where J denotes the total angular momentum quantum number. In the case of $\ell = 0$, there are only two possibilities. Furthermore, the charge conjugation quantum number for an antiproton-proton system is $C = (-1)^{\ell+S}$, while the parity is $P = (-1)^{\ell+1}$.

The right side is the list of values of C and P for $\pi^+\pi^-$ (or $k^+ k^-$) systems which are the products of the annihilations of the corresponding $\bar{p}$-p states, assuming only conservation of total angular momentum. For $\pi^+ \pi^-$ (or $k^+ k^-$) systems, $P = C = (-1)^J$.

Since C and P are conserved separately in the strong interactions, the only $\bar{p}$-p states from which annihilation can occur to give $\pi^+ \pi^-$ (or $k^+ k^-$) are

$$_3S^1,\ _3P^0,\ _3P^2,\ _3D^1,\ _3D^3,\ _3F^2,\ _3F^4 \text{ --- etc.}$$

as indicated by the checks in Table 6.5. In other words, the only $\bar{p}$-p states which can annihilate into $\pi^+ \pi^-$ (or $k^+ k^-$) are those for which $S = 1$ and $J = \ell \pm 1$. For $\bar{p} + p \rightarrow \pi^+ + \pi^-$, there is the further requirement that the G parity is positive.

These considerations limit the possible intermediate boson resonances that can be involved in $\bar{p} + p \rightarrow$ boson resonance $\rightarrow \pi^+ + \pi^-$. Some allowed resonances are ρ^o, f^o, f'(1500) etc., and their Regge recurrences.

Taking the condition $J = \ell \pm 1$ into consideration, the amplitude in the center-of-mass system for annihilation via resonances can be written as

$$\frac{1}{p^2}\left[\left|\sum_{\text{resonances}}\left(A_J\sqrt{\frac{J+1}{2(2J-1)}}\,Y_J^{\,1}+B_J\sqrt{\frac{J}{2(2J+3)}}\,Y_J^{\,1}\right)\right|^2\right.$$

$$+\left|\sum_{\text{resonances}}\left(A_J\sqrt{\frac{J}{2J-1}}\,Y_J^{\,0}-B_J\sqrt{\frac{J+1}{2J+3}}\,Y_J^{\,0}\right)\right|^2$$

$$\left.+\left|\sum_{\text{resonances}}\left(A_J\sqrt{\frac{J+1}{2(2J-1)}}\,Y_J^{\,-1}+B_J\sqrt{\frac{J}{2(2J+3)}}\,Y_J^{\,-1}\right)\right|^2\right]$$

where p = momentum of the antiproton in the center-of-mass system, and

J = spin of the resonance.

The square-rooted numbers are Clebsch-Gordan coefficients. The terms with A_J are contributions from initial states with $\ell = J - 1$, while those with B_J are from initial states with $\ell = J + 1$.

If, following Barger and Cline,[17] Breit-Wigner forms for the resonances are assumed,

$$A_J = A_J'/\epsilon_J - i$$

$$B_J = B_J'/\epsilon_J - i \qquad (A_J',\ B_J' \text{ are real})$$

where $\epsilon_J = (s - m_{R_J}^{\,2})/m_{R_J}\Gamma_J$,

$\sqrt{s}$ = total energy in center-of-mass system,

m_{R_J} = mass of the resonance,

Γ_J = half width of the resonance.

Thus, with this simple model, for every resonance, there are two parameters for fitting, A_J' and B_J', as well as the values of m_R, Γ, and J. The values of A_J' and B_J' are products of factors, including the partial widths for the transitions from this intermediate resonance to $\pi^{\pm}$-pair or to $\bar{p}$-p pair. They are usually assumed to be independent of the total energy.

In the angular distributions for $\bar{p} + p \rightarrow \pi^+ + \pi^-$, the 90^o peaking seems to be most pronounced for $\sqrt{s} \simeq 2.1$ GeV. A resonance at 2.2 GeV has been reported by Focacci et al. [20] and Abrams et al. [1] In a Chew-Frautschi plot, this resonance - called T by Focacci et al. - falls squarely on the ρ trajectory, along with the resonance R (1.69 GeV), also observed by Focacci et al.. This assumes that the ρ trajectory has more or less the same slope as most other trajectories, $\simeq$ 1 unit of spin/GeV^2. Under this scheme, R should have spin = 3, and T should have spin = 5. It is tempting to try to interpret the shape of the $\pi^{\pm}$-pair angular distributions as a manifestation of the T resonance.

Furthermore, it is known that antiproton-proton annihilation at rest proceeds from an S state. [15] As shown above, for annihilation into π^+ and π^-, the initial $\bar{p}$-p state must then be $_3S^1$. The only known boson resonance with the correct quantum numbers (J = 1, G = +, C = -, P = -, strangeness = 0) is ρ. Annihilations at rest into $\pi^{\pm}$-pairs are observed, and account for about the same fraction of annihilations as in this experiment. Since the lowest energy of this experiment ($\sqrt{s}$ = 2.0 GeV) is not very far away from the energy of $\bar{p}$-p at rest (1.88 GeV), the difference being about

equal to the width of the ρ, the ρ meson should also be included in a calculation for antiproton-proton annihilation into π^+ and π^- via resonances.

There are many other meson resonances which may contribute to the $\pi^{\pm}$-pair annihilation mode. A detailed investigation would involve a great deal of calculational effort beyond the scope of this work, and is probably not justified by the data. For data over a larger angular range, with the charges of the mesons determined, an attempted fit in terms of a few resonances might be worthwhile and informative.

For $\bar{p} + p \rightarrow k^+ + k^-$, the cross sections show no consistent tendency to increase as $\cos \Theta_{C.M.}$ approaches 1. Consequently, the contribution due to Regge exchange (Fig. 6.7b) can be assumed to be small in the angular range of this experiment. For annihilation via resonances, the set of possible intermediate resonances can have either + or - G parity. Since only + G parity is allowed for $\pi^{\pm}$-pairs, this may account for the difference between the $\pi^{\pm}$-pair and $k^{\pm}$-pair angular distributions. As pointed out, at $\sqrt{s} \cong 2.3$ GeV, a peak at $\Theta_{C.M.} = 90^{\circ}$ seems to develop in the $k^{\pm}$-pair cross section. No particular change is seen in the $\pi^{\pm}$-pair cross section at the same energies. Furthermore, Focacci et al. also observed a meson resonance at 2.38 GeV which they called U. On the Chew-Frautschi plot, U, if real, could be a Regge recurrence of A_2. If this is indeed true, the G parity of the U should be -, and this U is expected to decay into $k^+ k^-$ but not $\pi^+ \pi^-$.

APPENDIX I Hodoscope Logic

To demonstrate schematically how information was extracted from the counters in a hodoscope, an outer theta tray is used in this appendix as an example.

Each of the seventeen photo tubes was connected to a discriminator, whose threshold was set for it to respond to only pulses greater than half the magnitude of that due to the passage of one minimum ionizing particle through the scintillator. The output of the discriminator was 1 volt in height and 50 nsec in duration. It was used in the following fashion:

1) The seventeen outputs of an outer theta hodoscope were connected to a multiple coincidence circuit. All the coincidences between adjacent counters were used to generate standard-sized signals. These signals were then added on the "coincidence sum bus", a bus wire which was connected to two fast discriminators. The thresholds of these two discriminators were set such that one of them produced a pulse if the size of the signal on the coincidence sum bus indicated that at least one pair of adjacent counters had a coincidence (coincidence ≥ 0). The other discriminator generated a pulse only if there were more than one coincidence between adjacent counters (coincidence > 1).

2) In another part of the multiple coincidence circuit, the signal from the Nth counter was used to veto that from the (N-1)th counter. (See Fig. 2.3 for the manner in which the counters and channels were numbered.) The surviving signals were then added up on a wire called "channel sum bus". This was also connected to two discriminators, one set for number of channels > 0 and the other

for number of channels > 1. (The signals from these discriminators were called "channel > 0" and "channel > 1", respectively.) If there was a coincidence between two adjacent counters, the first discriminator (channel > 0) would give an output but not the second (channel > 1); the signal from the lower-numbered counter was ignored because of the veto from the higher-numbered counter. However, if two non-adjacent counters gave out signals simultaneously, both of the discriminators would respond, and both "channel > 0" and "channel > 1" signals were generated.

3) The signals from the discriminators of the counters, after the veto chain described above, were connected to a 5 bit binary encoder starting with the two's bit. The one's bit was connected to the output of the "coincidence > 0" discriminator mentioned in 1). Because of the particular way in which the channels and counters in an outer-theta-hodoscope were numbered, if only the Nth counter gave out a signal, the binary number was made to read 2N - 2. However, if there was a coincidence between the Nth and (N-1)th counters, the result would be 2N - 1.

In this manner, a hodoscope provided the information listed in Chap. 2, Sect. F.

APPENDIX II The Fiducial System

For each kinematic spark chamber, there were four 1/4" lucite fiducial plates (Fig. A2. 1) -- two θ-view plates, one on top, one at the bottom, and two θ-view plates, one at the downstream end, and the other at the upstream end of the chamber. Fiducial lines were machined across the plates, 6.00 ± 0.01 inches apart, perpendicular to the length of the chamber. For each chamber, the positions of the fiducial lines in real space were carefully surveyed and determined.

For each picture, fiducial lights were flashed and the lines became visible as seen in Fig. 3. 1. From the spark locations with respect to the fiducials, co-ordinates in real space could be reconstructed with negligible errors from optical distortions.

Throughout the experiment, the positions of all the cameras were unaltered, and hence the apparent positions of the two sets of fiducials in each view of the chambers were unchanged relative to each other. Thus, in a θ view, the apparent position of a spark relative to the bottom fiducial could be calculated once its apparent position relative to the top fiducial was determined. Similarly, this was true for the ϕ views.

For the reconstruction of events, a right-handed co-ordinate system was chosen. The surveyed center of the target was taken to be the origin. The directions of the x, y, and z axes are shown in Fig. A2. 1. The true spatial position of the spark in a plane parallel to the y-z plane could then be determined as illustrated in Fig. A2. 2. There, the spark appeared to be "a" fiducial units away from the farthest upstream top fiducial line of the θ view, one "fiducial unit" being defined as the distance

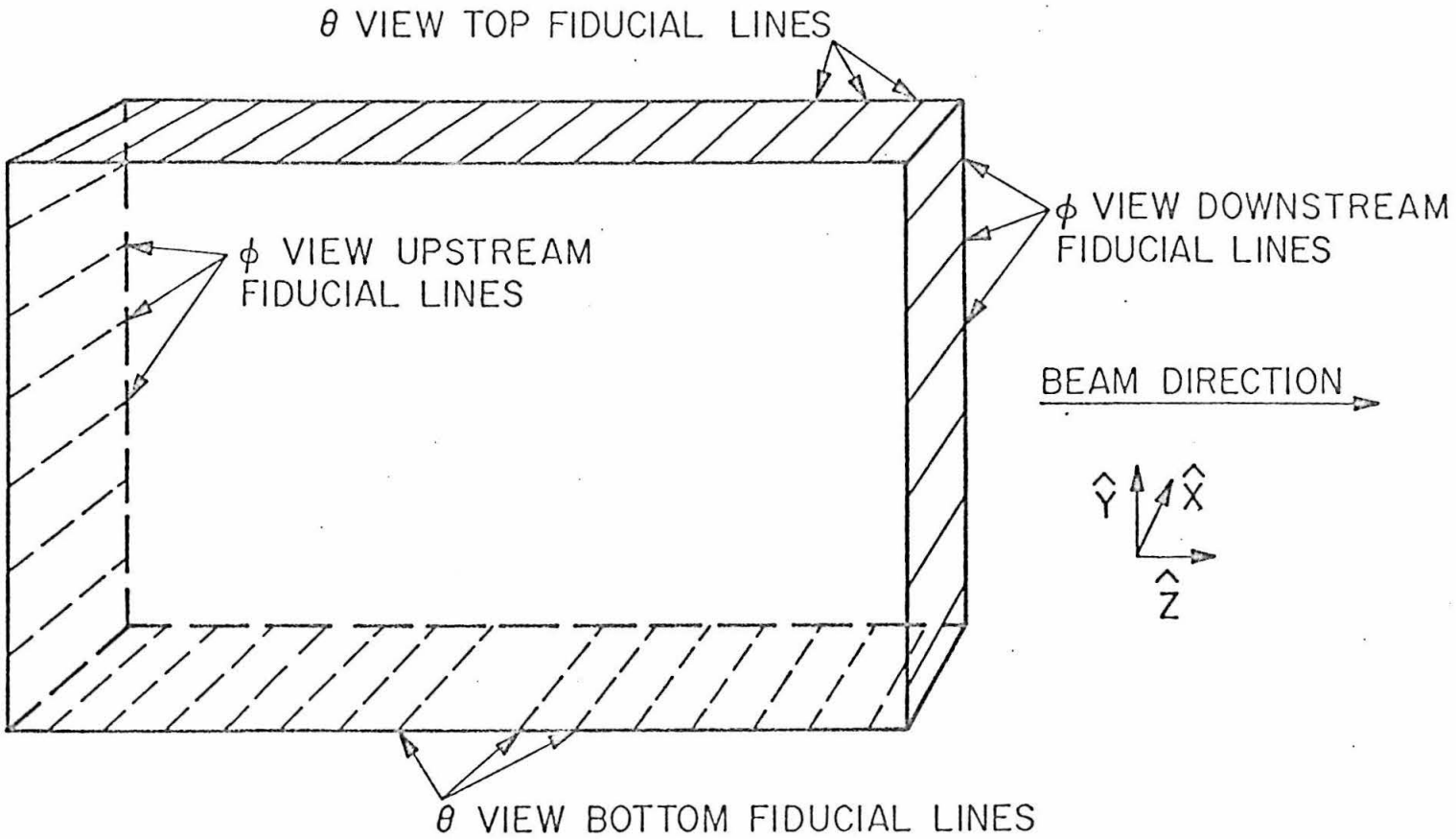

Fig. A2.1 The fiducial system on a kinematic spark chamber

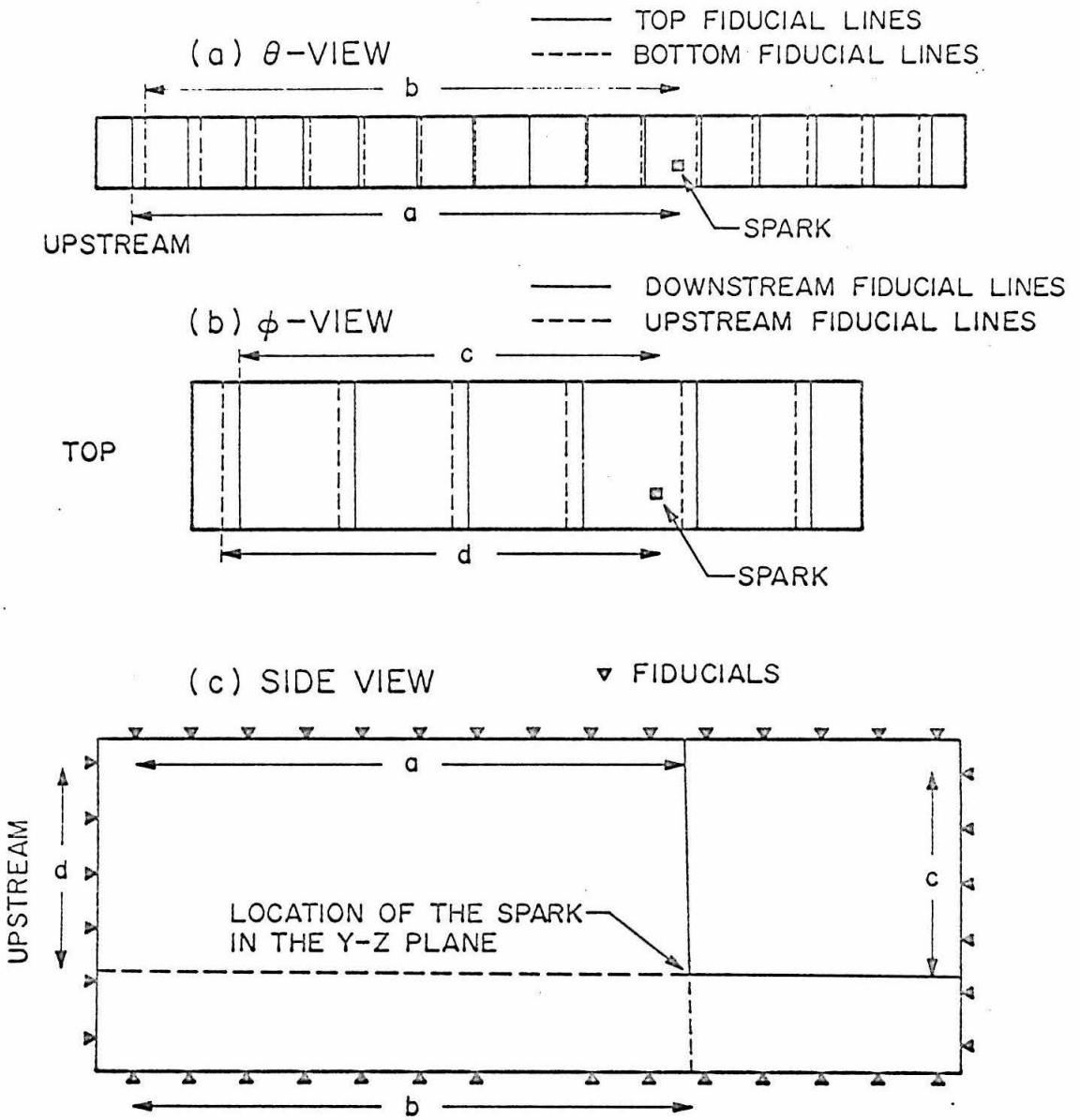

Fig. A2.2 Reconstruction of the position of a spark from the ϕ and θ views

between two fiducial lines. The same spark was "c" fiducial units away from the top-most downstream ϕ-view fiducial line. From these values, it could also be determined that the apparent spark position was "b" fiducial units away from the farthest upstream bottom θ-view fiducial line and "d" fiducial units from the top-most upstream ϕ-view fiducial line. From the values of a, b, c, and d, the position of the spark in a plane $x = x_0$ was reconstructed at the intersection of two straight lines as in Fig. A2. 2c.

In a measurement, as described in Chapter 3, the position of the second spark of a track relative to the fiducial grid was determined, and hence its y and z co-ordinates could be determined. The apparent angles of the track with the θ and ϕ fiducial lines were also measured. From the surveyed locations of the spark chamber plates, the x-co-ordinate of the second spark and the positions of the other seven sparks in the track could all be calculated. In this manner, a track was completely reconstructed in real space, to an accuracy mainly limited by the surveying technique used to establish the locations of the fiducial lines.

APPENDIX III The Measuring Device

The spark chamber pictures to be analyzed were projected onto a table with a 34" x 42" flat surface. The table was equipped with a measuring device which is shown pictorially in Fig. A3.1 and schematically in Fig. A3.2. The three sections of the arm AB, BC, and CD were 20", 20", and 14" long respectively. Point A was fixed onto the measurement table. The cross "E" was 8" away from pivot C. The three sections of the arm could be moved to place the cross "E" at any point and align "CD" with any line on the table. At pivots A, B, and C there were pulleys rigidly connected to sections AB, BC and CD respectively. These pulleys were coupled by stainless steel belts to the pulleys of three angle encoders. Each encoder registered the rotation of only one of the pulleys at A, B, and C. The encoder design, and the ratios of the radii of the pulleys were such that an angle of 90^{o} was divided into 8192 parts.

A standard position of the three sections of the arm was chosen where all the encoder readings were set to zero, and Fig. A3.1 shows the arm in this position. A rectangular co-ordinate system was chosen on the table with its origin at "A" and its "y" direction parallel to "CD" when the arm was in the standard position (see Fig. A3.2 for this co-ordinate system). If the arm was moved to any other position, the encoders registered the rotations the three sections of the arm underwent to reach this new position.

Suppose that at the standard position, the angles α and β (see Fig. A3.2) were α_o and β_o. If the arm was moved so that the cross E was at position P, say, and the encoders registered

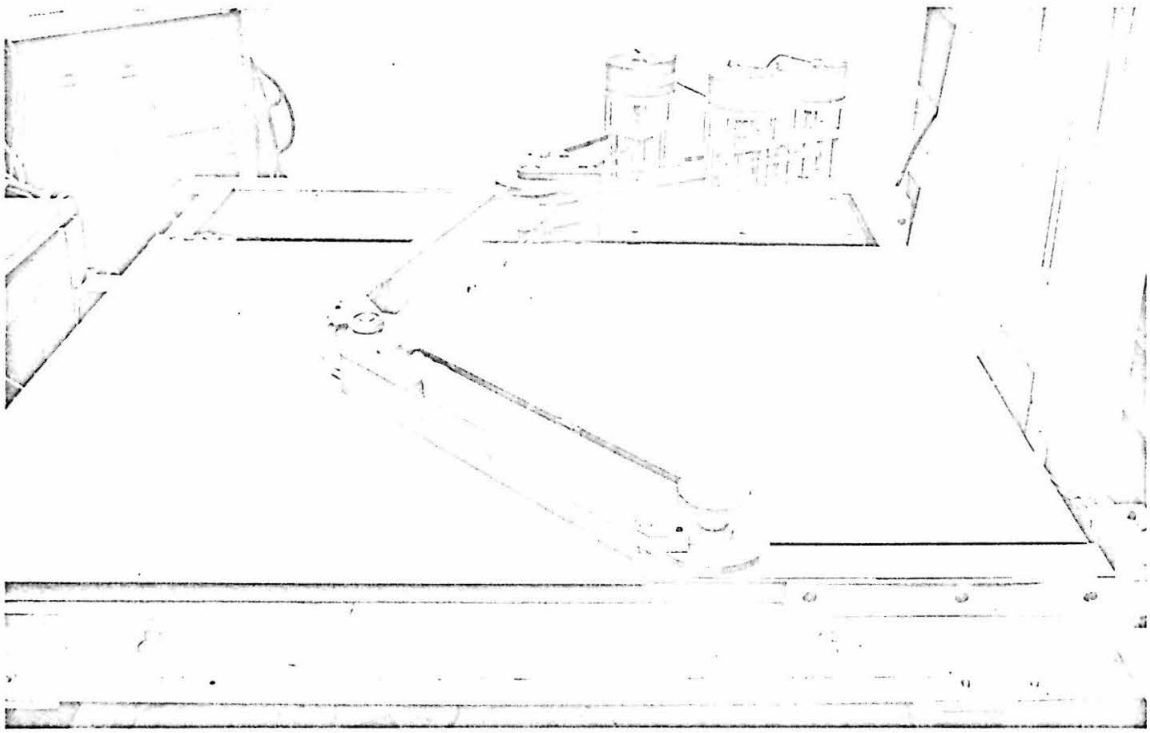

Fig. A3.1 The measuring table

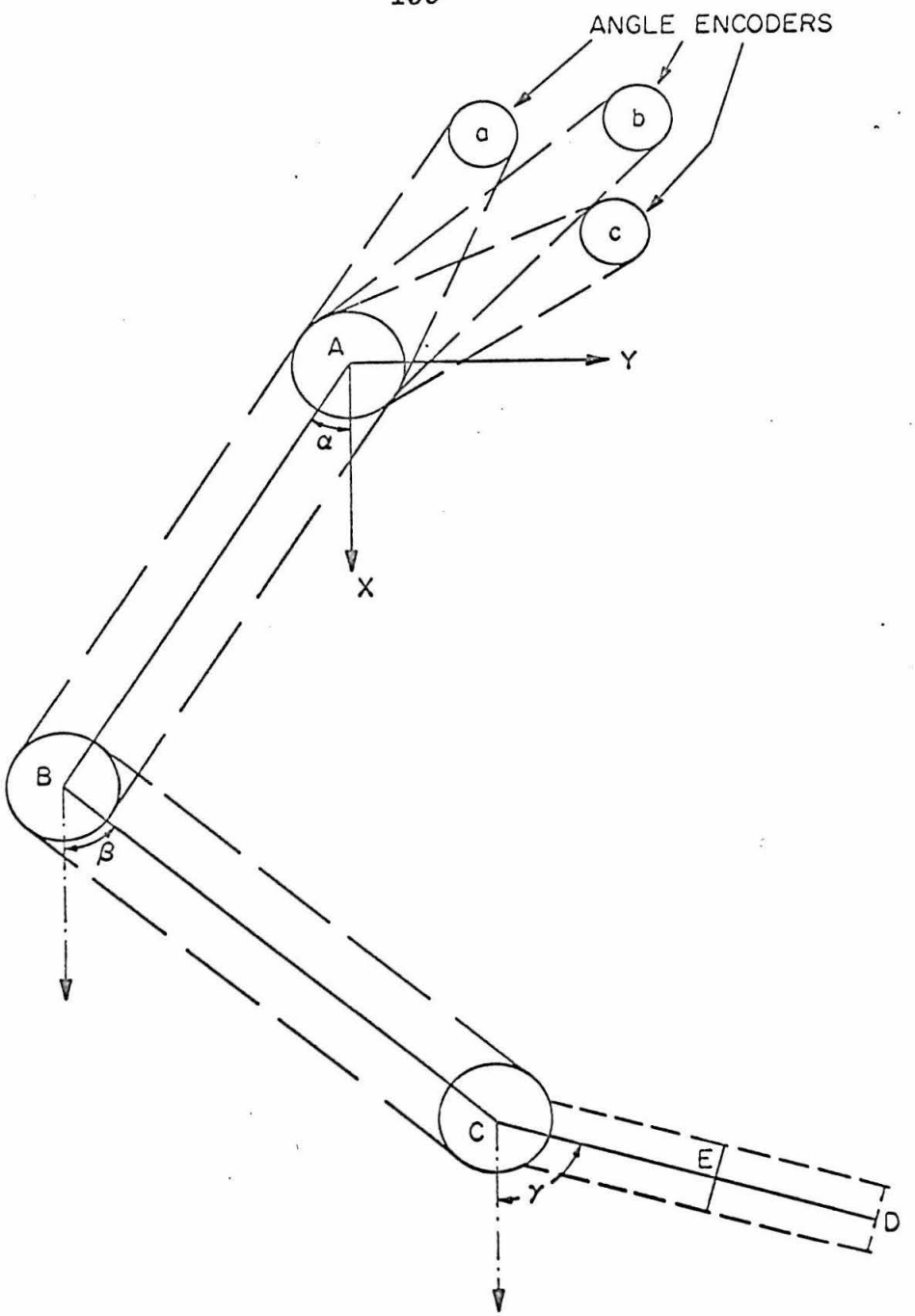

Fig. A3.2 Schematic diagram of the measuring device

rotations of $\Delta\alpha$ by section "AB," $\Delta\beta$ by "BC," and $\Delta\gamma$ by "CD," then the three sections' polar angles in the chosen co-ordinate system were

$$\alpha = \alpha_o + \Delta\alpha, \qquad \beta = \beta_o + \Delta\beta, \qquad \gamma = \frac{\pi}{2} + \Delta\gamma$$

and the point P was located at

$$X_P = 20'' \cos(\alpha_o + \Delta\alpha) + 20'' \cos(\beta_o + \Delta\beta) + 8'' \cos(\frac{\pi}{2} + \Delta\gamma)$$

$$Y_P = 20'' \sin(\alpha_o + \Delta\alpha) + 20'' \sin(\beta_o + \Delta\beta) + 8'' \sin(\frac{\pi}{2} + \Delta\gamma) .$$

Thus, once α_o and β_o were known, the arm could be used to determine the co-ordinates of any point, and hence distances on the table.

To determine the values of α_o and β_o, they were first measured roughly with a protractor. The arm was then used to measure distances on a precision straight edge (graduated in units of 0.010") placed in various positions on the measurement table. The values of α_o and β_o were then adjusted until the errors in the results were minimized. It was found that the arm was able to measure distances of 15" to an accuracy of $\pm$ 0.025".

APPENDIX IV Radiative Correction Calculation

The radiative corrections for colliding beam experiments have been worked out by Y. S. Tsai.[8] With some slight modification, his calculation can be applied to this experiment. To demonstrate how this was carried out, the calculation for $\bar{p} + p \rightarrow \pi^+ + \pi^-$ is described here in detail.

In this experiment, $\pi^{\pm}$-pair events were identified by the directions of the final charged particles. One of the necessary conditions was that the deviation from coplanarity of the two final particles in an event had to be within 2.25°. Another necessary condition was that the value of m^2 for the event as calculated with Eqn. 4.1 had to be within the range -0.12 to 0.14 GeV^2 (see Chapter 4, Section D). Consequently, given the direction of one of the final particles, the polar angle θ_{LAB} of the other particle had to be within $\pm \Delta\theta_{LAB}$ of the direction according to two body kinematics, where

$$\Delta\theta_{LAB} = \frac{.14-(-.12)}{2} \Big/ \left|\frac{dm^2}{d\theta_{LAB}}\right| = .13 \Big/ \left|\frac{dm^2}{d\theta_{LAB}}\right| .$$

The quantity $dm^2/d\theta_{LAB}$ is given by Eqn. 4.5. Fig. A4.1 shows the values of $\Delta\theta_{LAB}$ for $\pi^{\pm}$-pair events as a function of θ_{LAB} at three antiproton beam momenta.

This tolerance in the value of θ_{LAB} was reflected in a tolerance $\Delta\Theta$ in the value of the center-of-mass angle Θ defined in Chapter 4, Section B. To calculate $\Delta\Theta$ from $\Delta\theta_{LAB}$, the following relativistic transformation equation is used:

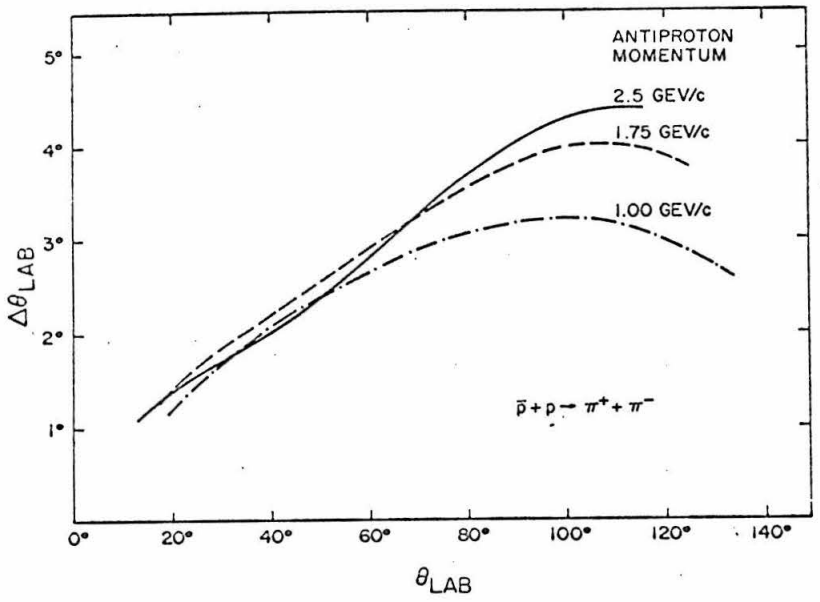

Fig. A4.1 Maximum acceptable deviation $\Delta\theta_{LAB}$ from ideal two-body kinematics in the laboratory

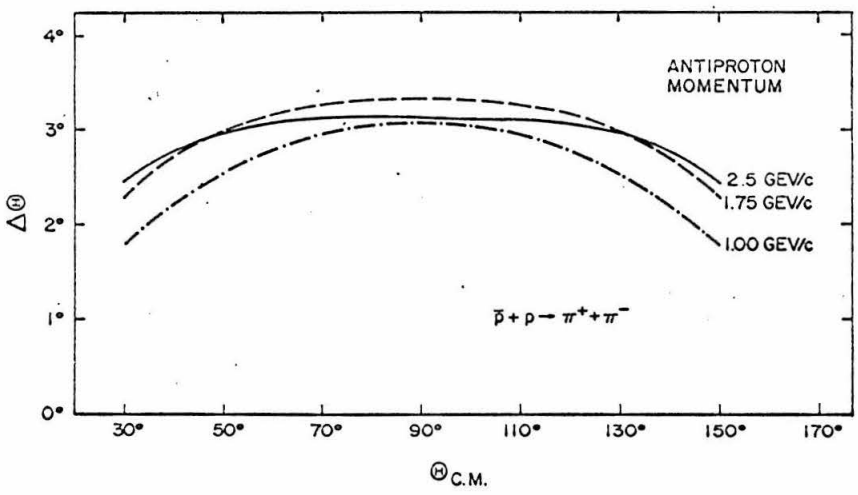

Fig. A4.2 Maximum acceptable deviation $\Delta\Theta$ from ideal two-body kinematics in the C. M. system

$$\bar{p}_z = \gamma(p\cos\Theta + \beta\sqrt{p^2 + m^2}) . \qquad \text{A4.1}$$

Here, the z direction is defined to be the direction of the antiproton,

c (velocity of light) $\equiv$ 1,

$\bar{p}$ = laboratory momentum of one of the mesons,

p = center-of-mass system momentum of the same meson,

m = mass of the meson,

β = velocity of the C. M. system in the laboratory,

and $\gamma = 1/\sqrt{1 - \beta^2}$.

For laboratory incident antiproton momentum Q,

$$\beta = \left(\frac{\sqrt{Q^2 + M^2} - M}{\sqrt{Q^2 + M^2} + M} \right)^{1/2} , \quad \text{where M = mass of antiproton.}$$

Thus,

$$\tan\theta_{LAB} = \frac{\bar{p}}{\bar{p}_z} = \frac{p\sin\Theta}{\gamma(p\cos\Theta + \beta\sqrt{p^2 + m^2})} . \qquad \text{A4.2}$$

Differentiating Eqn. A4.2, the following relationship was obtained,

$$\Delta\Theta = \frac{\sin^2\Theta + \gamma^2(\alpha + \cos\Theta)^2}{\gamma(1 + \alpha\cos\Theta)} \quad \Delta\theta_{LAB} \qquad \text{A4.3}$$

where, $\alpha \equiv \beta\sqrt{p^2 + m^2}/p$.

Fig. A4.2 gives the values of $\Delta\Theta$ for $\pi^{\pm}$-pair events as a function of center-of-mass angle Θ at three laboratory antiproton beam momenta.

By conservation of energy and momentum, the maximum allowed momentum of the photon in the final state, for acceptable events, could then be calculated as a function of its direction in the center-of-mass system. Fig. A4.3 is a schematic drawing of the phase space of the allowed photon momentum. If an event of the type $\bar{p} + p \rightarrow \pi^+ + \pi^- + \gamma$ had a photon harder than as indicated by the bomb-shaped region, it would not be accepted as a $\pi^{\pm}$-pair event.

The phase space was divided into three regions as shown, each contributing to the radiative correction δ:

$$\delta = \delta_{SOFT} + \delta_A + \delta_B$$

where δ is defined by the expression $\left(\frac{d\sigma}{d\Omega}\right)_{OBSERVED} = \left(\frac{d\sigma}{d\Omega}\right)_{TOTAL}(1+\delta)$.

For this experiment, the results were obtained in the form $\left[\frac{d\sigma}{d\Omega}(\Theta) + \frac{d\sigma}{d\Omega}(\pi - \Theta)\right]$. If it is assumed that, in the angular range of the data, $\frac{d\sigma}{d\Omega}(\Theta)$ and $\frac{d\sigma}{d\Omega}(\pi - \Theta)$ are of the same order of magnitude, the correction δ' for this experiment is

$$\delta'(\Theta) = \frac{1}{2}\left(\delta(\Theta) + \delta(\pi - \Theta)\right)$$

and,

$$\left[\frac{d\sigma}{d\Omega}(\Theta) + \frac{d\sigma}{d\Omega}(\pi - \Theta)\right]_{OBSERVED} = \left[\frac{d\sigma}{d\Omega}(\Theta) + \frac{d\sigma}{d\Omega}(\pi - \Theta)\right]_{TOTAL}(1 + \delta').$$

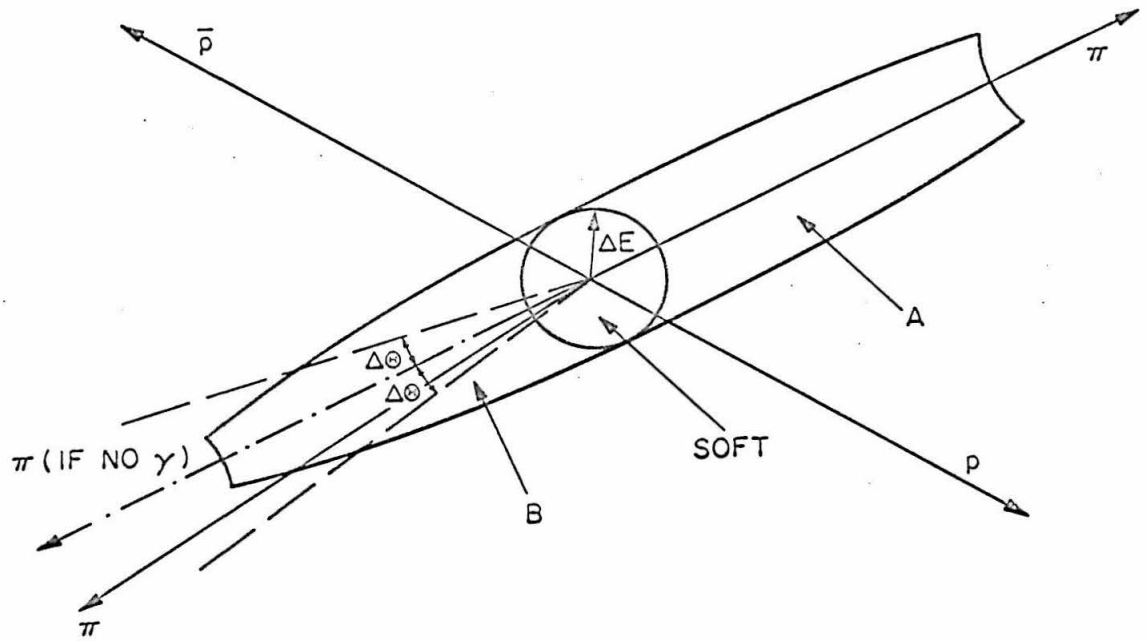

Fig. A4.3 Phase space of allowed photon momentum

In Fig. A4.3, the boundary for the "soft photons" is given by (Ref. 8, Eqn. 8):

$$\Delta E \approx \frac{2E\ \Delta\Theta'}{2\sin\Theta + \Delta\Theta'}$$

where, $\Delta\Theta' = \sqrt{\Delta\Theta \cdot \Delta\phi_{MAX}} = \sqrt{2.25\ \Delta\Theta}$.

Also, as given in Ref. 8,

$$\delta_{SOFT}(\Theta) = \frac{\alpha}{\pi} \ln \frac{\varepsilon}{\Delta E} \left[2 - \frac{2E^2 - m^2}{\varepsilon p} \ln \frac{(\varepsilon + p)^2}{m^2} - \frac{2E^2 - M^2}{\varepsilon P} \ln \frac{(\varepsilon + P)^2}{M^2} \right.$$

$$\left. + 4 \ln \frac{E^2 - Pp\cos(\pi - \Theta)}{\varepsilon^2 - Pp\cos\Theta} \right]$$

where ε = energy of the antiproton in the C. M. system, and

P = momentum of the antiproton in the C. M. system.

The other quantities remain the same as defined before.

For this experiment,

$$\delta'_{SOFT}(\Theta) = \frac{\alpha}{\pi} \ln \frac{\varepsilon}{\Delta E} \left[2 - \frac{2E^2 - m^2}{\varepsilon p} \ln \frac{(\varepsilon + p)^2}{m^2} - \frac{2E^2 - M^2}{\varepsilon P} \ln \frac{(\varepsilon + P)^2}{M^2} \right].$$

Fig. A4.4 shows the values of this contribution to radiative correction by "soft photons" at three beam momenta.

Tsai's calculation of the "hard photon" contributions from regions A and B in Fig. A4.1 was done for fermions:

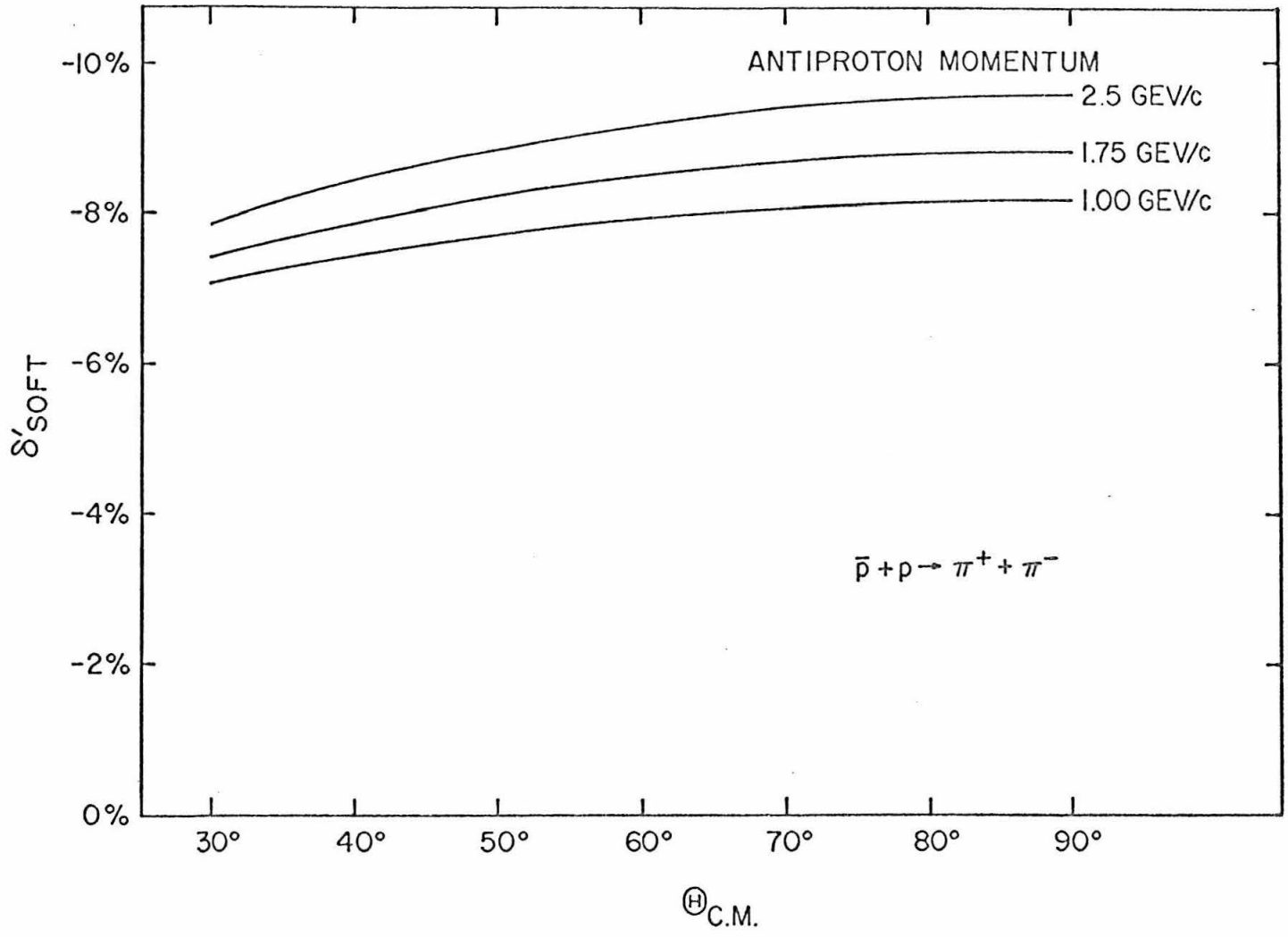

Fig. A4.4 Contribution to radiative corrections for $\bar{p} + p \rightarrow \pi^+ + \pi^-$ due to "soft" photons

$$\delta_A = \frac{\alpha}{\pi}\left[\left(\ell n\,\frac{\mathcal{E} - E_{min}}{\Delta E} - \frac{\mathcal{E} - E_{min} - \Delta E}{\mathcal{E}}\right)\ell n\,\frac{2E^2}{m^2} - \ell n\,\frac{\mathcal{E} - E_{min}}{\Delta E}\right.$$

$$\left. - \ell n^2\,\frac{\mathcal{E}\Delta\Theta}{\sqrt{2(\mathcal{E} - E_{min})}} + 2\,\frac{\mathcal{E} - E_{min}}{\mathcal{E}}\,\ell n\,\frac{\sqrt{2}(\mathcal{E} - E_{min})}{\Delta\Theta\mathcal{E}}\right]$$

$$\delta_B = \frac{\alpha}{\pi}\left[\left(\ell n\,\frac{\mathcal{E} - E_{min}}{\Delta E} - \frac{\mathcal{E} - E_{min} - \Delta E}{\mathcal{E}}\right)\ell n\left(\frac{\mathcal{E}}{m}\Delta\Theta\right)^2 - \ell n\,\frac{\mathcal{E} - E_{min}}{\Delta E}\right.$$

$$\left. + \ell n^2\,\frac{\mathcal{E}}{\Delta E}\right]$$

where E_{min} was the minimum energy in the center-of-mass system either of the final particles could have and still satisfy the identification conditions. It determines the "length" of the bomb-shaped region in Fig. A4.3. In this experiment, where the energies of the final particles were not used for their identification, E_{min} was small compared to $\mathcal{E}$. Furthermore, the dependence of $\delta_A + \delta_B$ on E_{min} was quite small as shown in Fig. A4.5. Fig. A4.6 gives the "hard photon" contribution to radiative correction at three beam momenta. E_{min} was taken to be 0 GeV. The hard photon contribution was symmetric with respect to center-of-mass angle $\Theta = 90^o$. Therefore,

$$\delta'_{hard}(\Theta) = \delta_A(\Theta) + \delta_B(\Theta) = \delta_A(\pi - \Theta) + \delta_B(\pi - \Theta)\,.$$

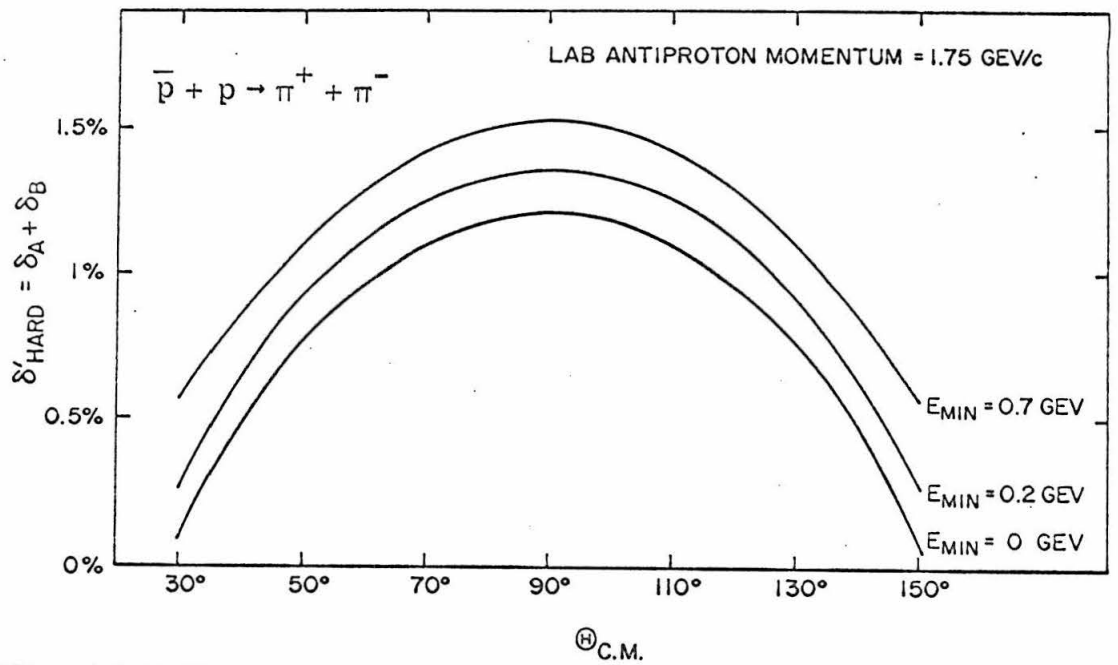

Fig. A4.5 Dependence of hard photon contribution to radiative corrections on E_{min}, the minimum acceptable meson C.M. energy

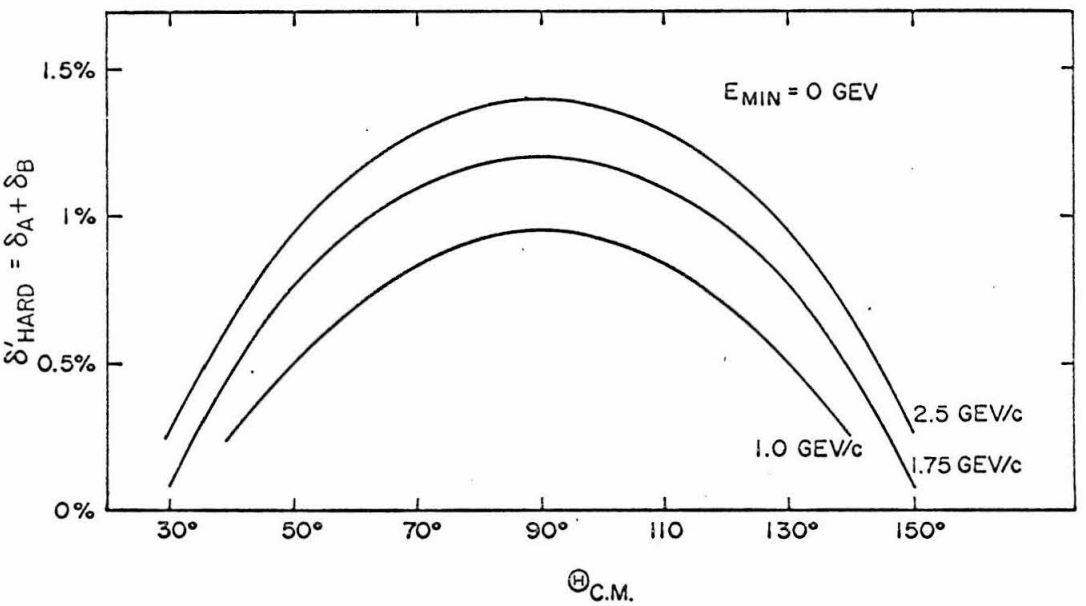

Fig. A4.6 Contribution to radiative corrections for $\bar{p} + p \rightarrow \pi^+ + \pi^-$ due to "hard" photons, assuming $E_{min} = 0$ GeV

For this experiment, the particles in the final state were bosons. In general, hard photon bremsstrahlung emission is more intense in the case of fermions than of bosons.[21] Hence, the hard photon contribution to the radiative correction in this experiment was expected to be even less than that shown in Fig. A4.6. In the angular range of the data, it was taken to be

δ'_{hard} = 0.6 ± 0.3% for lab antiproton beam momentum 1 GeV/c,

= 0.8 ± 0.4% for 1.75 GeV/c,

and = 1.0 ± 0.5% for 2.5 GeV/c.

The total radiative corrections adopted for $\bar{p}\, p \to \pi^+ \pi^-$ are summarized in Fig. 5.3a.

For the $k^{\pm}$-pair events, a similar calculation was carried out. Because of the larger mass of the k-meson, hard photon contributions for the energy range of this experiment were negligible. The results are summarized in Fig. 5.3b.

VIII. REFERENCES

(1) R. J. Abrams, R. L. Cool, G. Giacomilli, T. F. Kycia, B. A. Leontie, K. K. Li, and D. N. Michael, Phys. Rev. Letters 18, 1209 (1967).

(2) G. R. Lynch, Rev. Mod Phys. 33, 395 (1961).

(3) G. R. Lynch, P. Eberhard, G. R. Kalfleisch, J. E. Lannutti, B. C. Maglic, J. B. Shafer, M. L. Stevenson, and N. H. Xuong, Phys. Rev. 131, 1287 (1963).

(4) D. Hartill, PhD Thesis, Calif. Inst. of Tech. (1967).

(5) B. Barish, and T. F. Kycia, (to be published).

(6) UCRL-2426 (rev.) II (1957).

(7) G. R. Lynch, R. E. Foulks, G. R. Kalbfleisch, S. Limentani, J. B. Shafer, M. L. Stevenson, and N. H. Xyong, Phys. Rev. 131, 1276 (1963).

(8) Y. S. Tsai, Stanford University preprint SLAC-PUB-117 (1967).

(9) S. Gasiorowicz, "Elementary Particle Physics," John Wiley & Sons, Inc. 1966, p. 294.

(10) M. Crozon, Ph. Chavanon, A. Courau, Th. Leray, J. L. Narjoux, and J. Tocqueville, Nuclear Physics 64, 567 (1965).

(11) S. Gasiorowicz, "Elementary Particle Physics," John Wiley & Sons, Inc., 1966, p. 306.

(12) T. Ferbel, A. Firestone, J. Sandweiss, H. D. Taft, M. Gailloud, T. W. Morris, A. H. Bachman, P. Baumel, and R. M. Lea, Phys. Rev. 137, B1251 (1965).

(13) O. Czyzewski, B. Esconbes, Y. Goldschmidt-Clermont, M. Guinea-Moorhead, T. Hofmokl, R. Lewisch, D. R. O. Morrison, M. Schneeberger, and S. de Unamuno, Proceedings of the 1963 International Conference on High Energy Physics at Sienna, p. 271.

(14) W. M. Katz, B. Forman, and T. Ferbel, Phys. Rev. Letters 19, 265 (1967) .

(15) C. Baltay, N. Barash, P. Franzini, N. Gelfand, L. Kirsch, G. Lutzens, D. Miller, J. C. Severiens, J. Steinberger, T. H. Tan, D. Tycko, D. Zanello, D. Goldberg, and J. Plano, Phys. Rev. Letters 15, 532 (1965).

(16) V. Barger and M. Olsson, Phys. Rev. 151, 1123 (1966).

(17) V. Barger and D. Cline, Phys. Rev. 155, 1792 (1967).

(18) C. B. Chiu and J. D. Stack, Phys. Rev. 153, 1575 (1967).

(19) V. Barger and D. Cline, University of Wisconsin preprint (June, 1967).

(20) M. N. Focacci, W. Kienzle, B. Levrat, B. C. Maglic, and M. Martin, Phys. Rev. Letters 18, 1209 (1966).

(21) B. Rossi, "High-Energy Particles." Prentice Hall, Inc., 1961, p. 62.